

The conversion rate of lee waves and the energetics of
internal tides

Dissertation zur Erlangung des Doktorgrades
an der Fakultät für Mathematik, Informatik und Naturwissenschaften
Fachbereich Geowissenschaften
der Universität Hamburg

vorgelegt von

Bing Han

Hamburg, 2017

Tag der Disputation: 28.06.2017

Folgende Gutachter empfehlen die Annahme der Dissertation:

Prof. Dr. Carsten Eden

Dr. Jin-Song von Storch

Declaration on oath

I hereby declare, on oath, that I have written the present dissertation by my own and have not used other than the acknowledged resources and aids.

Bing Han
Hamburg, 2017

Abstract

Tides and geostrophic flows are two important energy sources for the mixing in the deep ocean. The global conversion rate of internal lee waves generated by geostrophic flows, the baroclinic tide generated by the barotropic tide over sinusoidal topography and the energy budgets of internal waves at the Luzon ridge calculated from both two-dimensional and three-dimensional simulations are investigated in this paper. It is aimed to give us a better understanding of the role of tides and geostrophic flows in ocean dynamics. This paper consists of four parts.

Firstly, the conversion rate of internal lee waves generated by geostrophic flows is calculated based on linear theory. In order to get a more precise value, we use two methods to deal with the topographic spectrum. The single beam sounding depth data, global predicted abyssal hill rms heights, WOCE hydrographic atlas, velocity data from SODA and ECCO2, mean flow and eddy velocity from the global eddy-permitting STORM model in a $1^\circ \times 1^\circ$ grid are used for the calculations. By using these data, we can not only compare with the results from different velocity and topography databases, but also get the difference between the conversion rate from the eddies and from the mean flow. The results show that the conversion rates calculated using SODA, ECCO2, mean flow and eddy velocity from the global eddy-permitting STORM model are between 0.03 and 0.23 TW, and the difference between the conversion rate from the eddies and from the mean flow is between 0.05 and 0.11 TW.

Secondly, a series of experiments are set up to investigate the baroclinic tide generated by barotropic tide over sinusoidal topography. The baroclinic velocity fields generated are quite different between in subcritical cases and in supercritical cases. The effects of the height of the topography, the amplitude of the barotropic tidal velocity, the stratification and the width of the topography on the baroclinic tide generated are studied in this chapter. The results show that the energy flux is almost proportional to the square of the height of the topography and the square of the amplitude of the barotropic tide; the energy flux will be larger when the width of topography is smaller and the stratification is stronger; there is almost no energy flux generated in experiments with too weak stratification or too wide topography. The results predicted by the linear theory agree well with the results calculated by C1

(energy flux) in most cases, and the results calculated by C2 (conversion rate) are larger than the results calculated by C1 in most cases (the definitions of C1 and C2 could be found in Chapter 3).

Thirdly, two-dimensional MIT General Circulation Model (MITgcm) is used to simulate internal waves at the Luzon ridge. Here, the topography is represented by two ideal Gaussian hills. The baroclinic energy budget of internal waves is studied and the conversion rate is mainly balanced by the energy flux. The effects of the height of the west ridge, the distance between the two ridges and the amplitude of the barotropic tide on the energy flux and conversion rate are also investigated. It is found that as the height of the west ridge increases, the westward energy flux increases; the internal tides can be enhanced due to a suitable distance between the two ridges; the amplitude of the barotropic tide is one of the crucial factors to determine whether the internal solitary waves would be generated or not, furthermore, when the amplitude of the barotropic tide is larger, the speed of the internal solitary waves generated will be larger.

Finally, three-dimensional simulations of internal tides at the Luzon ridge are shown. The MITgcm is used to study the M2 and K1 internal tides and the data from WOCE and SODA are used to give the stratification here. In this chapter, not only the barotropic energy budget and baroclinic energy budget but also the barotropic kinetic energy budget and baroclinic kinetic energy budget are analyzed. About 15.1 GW is transferred from the M2 barotropic tide to the baroclinic tide, which is about 88% of the barotropic input. The energy flux is about 4.5 GW, and the total dissipation is about 11.3 GW. The formula (Nycander, 2005) may underestimate the conversion rate at the Luzon ridge.

Contents

Abstract	i
List of Figures	vi
List of Tables.....	xi
1 Introduction	1
1.1 Motivation.....	1
1.2 The lee waves.....	5
1.3 The internal tides.....	7
1.3.1 The linear internal wave theory	7
1.3.2 The conversion rate of internal tides.....	9
1.3.3 The energy budgets of internal tides	10
1.4 The internal waves at the Luzon ridge	12
1.4.1 The internal tides.....	12
1.4.2 The internal solitary waves	13
1.5 Overview of the thesis	15
2 The conversion rate of internal lee waves generation by global geostrophic flows	16
Abstract.....	16
2.1 Introduction.....	16
2.2 Theory	17
2.3 The bottom stratification.....	18
2.4 The bottom topography	19
2.4.1 The single beam sounding depth data,	19
2.4.2 Global predicted abyssal hill rms heights	21
2.5 The bottom velocity	22
2.5.1 The bottom velocity from SODA and ECCO2	22
2.5.2 The mean flow and eddy velocity from the global eddy-permitting STORM model.....	23
2.6 Results.....	24
2.6.1 Steepness parameter.....	24
2.6.2 Conversion rate	25

2.7 Summary	27
3 Tidal flow over sinusoidal topography: the harmonics, energy flux and conversion rate.....	34
Abstract	34
3.1 Introduction.....	34
3.2 Model	36
3.3 The baroclinic velocity.....	38
3.4 The kinetic energy and potential energy	40
3.5 The spectra	47
3.6 The harmonics.....	50
3.7 The energy flux and conversion rate.....	54
3.8 Discussion and conclusion.....	58
4 The two-dimensional simulations of internal waves at the Luzon ridge	62
Abstract	62
4.1 Introduction.....	62
4.2 Model	65
4.3 The spectra	67
4.4 The baroclinic energy budget.....	69
4.4.1 Theory	69
4.4.2 The energy budget.....	70
4.4.3 Evolution of the energy budget.....	72
4.5 Sensitivity experiments	73
4.5.1 The height of the west ridge.....	73
4.5.2 The distance between the two ridges	77
4.5.3 The amplitude of the barotropic tide.....	81
4.6 Conclusion	84
5 The energetics of internal tides at the Luzon ridge	86
Abstract	86
5.1 Introduction.....	86
5.2 Model	89

5.3 Model validation	92
5.3.1 The M2 baroclinic velocity	92
5.3.2 The M2 tidal ellipses.....	94
5.4 The energy budgets	95
5.4.1 The barotropic and baroclinic energy equations	95
5.4.2 The barotropic and baroclinic kinetic energy equations	100
5.5 The energy budgets of K1 internal tide.....	103
5.6 The conversion rate (Nycander, 2005).....	105
5.7 Discussion	108
5.8 Conclusion	109
6 Summary and Outlook.....	112
6.1 Summary	112
6.2 Outlook	116
Acknowledgements.....	117
Bibliography	118

List of Figures

Figure 1.1. The conceptual model of MOC. AAIW stands for Antarctic Intermediate Water, AABW stands for Antarctic Bottom Water and NADW stands for North Atlantic Deep Water. From Vallis (2016).	1
Figure 2.1. Bottom stratification N using WOCE hydrographic atlas in $\log_{10} (s^{-1})$	19
Figure 2.2. a) The topographic roughness calculated by averaging spectra first in (m). b) The topographic roughness calculated by averaging the final results in (m).	21
Figure 2.3. The topographic roughness of Goff and Arbic (2010) in (m).	22
Figure 2.4. Bottom kinetic energy of SODA (a) and ECCO2 (b) in $\log_{10} (m^2 s^{-2})$	23
Figure 2.5. Bottom MKE (a) and bottom EKE (b) in $\log_{10} (m^2 s^{-2})$	24
Figure 2.6. The topographic steepness parameter ϵ calculated using eddy velocity in $\log_{10} ()$	25
Figure 2.7. The internal lee waves generation rate of SODA. a) Average spectra first in $\log_{10} (mW m^{-2})$. b) Average the final results in $\log_{10} (mW m^{-2})$	29
Figure 2.8. The internal lee waves generation rate of ECCO2. a) Average spectra first in $\log_{10} (mW m^{-2})$. b) Average the final results in $\log_{10} (mW m^{-2})$	30
Figure 2.9. The internal lee waves generation rate of mean flow. a) Average spectra first in $\log_{10} (mW m^{-2})$. b) Average the final results in $\log_{10} (mW m^{-2})$	31
Figure 2.10. The internal lee waves generation rate of eddy velocity. a) Average spectra first in $\log_{10} (mW m^{-2})$. b) Average the final results in $\log_{10} (mW m^{-2})$	32
Figure 3.1. Snapshots of baroclinic velocity ($m s^{-1}$) after 7 tidal cycles, the height of the topography (a) $h=200$ m, (b) $h=400$ m, (c) $h=800$ m, and (d) $h=1600$ m.	40
Figure 3.2. Snapshots of baroclinic velocity ($m s^{-1}$) after 7 tidal cycles, (a) $u=0.05$ $m s^{-1}$, and (b) $h=0.20$ $m s^{-1}$	40
Figure 3.3. Snapshots of baroclinic velocity ($m s^{-1}$) after 7 tidal cycles, the stratification (a) $N=10^{-3.5} s^{-1}$, and (b) $N=10^{-2} s^{-1}$	40
Figure 3.4. Snapshots of baroclinic velocity ($m s^{-1}$) after 7 tidal cycles, the width of the topography (a) width=18 km, and (b) width=54 km.	40

Figure 3.5. Snapshots of APE, KE, and APE plus KE for Exp_Ref after 7 tidal cycles, a) APE, b) KE, and c) APE+KE.....	42
Figure 3.6. Snapshots of APE, KE, and APE plus KE for Exp_width18 after 7 tidal cycles, a) APE, b) KE, and c) APE+KE.....	43
Figure 3.7. Snapshots of APE, KE, and APE plus KE for Exp_N2.5 after 7 tidal cycles, a) APE, b) KE, and c) APE+KE.....	43
Figure 3.8. The APE, KE, and APE plus KE for Exp_Ref averaged over 4 tidal cycles, a) APE, b) KE, and c) APE+KE.....	44
Figure 3.9. The APE, KE, and APE plus KE for Exp_width18 averaged over 4 tidal cycles, a) APE, b) KE, and c) APE+KE.....	44
Figure 3.10. The APE, KE, and APE plus KE for Exp_width18 averaged over 4 tidal cycles, a) APE, b) KE, and c) APE+KE.....	45
Figure 3.11. Temporal evolution of APE, KE, and APE plus KE for Exp_Ref, a) APE, b) KE, and c) APE+KE.....	45
Figure 3.12. Temporal evolution of APE, KE, and APE plus KE for Exp_width18, a) APE, b) KE, and c) APE+KE.....	46
Figure 3.13. Temporal evolution of APE, KE, and APE plus KE for Exp_N2.5, a) APE, b) KE, and c) APE+KE.....	46
Figure 3.14. The spectra of baroclinic velocity u' and w' for Exp_Ref at point A ($x=0$ km, $z=-1000$ m) and point B ($x=60$ km, $z=-1000$ m), respectively. The baroclinic velocity is scaled by 0.025 m s^{-1} and ω represents the M2 tidal frequency.	48
Figure 3.15. The spectra of baroclinic velocity u' for Exp_Ref, Exp_u0.05, Exp_u0.10 and Exp_u0.20 at point B ($x=60$ km, $z=-1000$ m), respectively. The baroclinic velocity is scaled by u_0 and ω represents the M2 tidal frequency.....	49
Figure 3.16. The spectra of baroclinic velocity w' for Exp_Ref, Exp_u0.05, Exp_u0.10 and Exp_u0.20 at point B ($x=60$ km, $z=-1000$ m), respectively. The baroclinic velocity is scaled by u_0 and ω represents the M2 tidal frequency.....	49
Figure 3.17. The spectra of baroclinic velocity u' and w' for Exp_3sinsoidal at point A ($x=0$ km, $z=-1000$ m) and point C ($x=100$ km, $z=-1000$ m),	

respectively. The baroclinic velocity is scaled by 0.025 m s^{-1} and ω represents the M2 tidal frequency.	50
Figure 3.18. The baroclinic velocity field for Exp_Ref: (top) mode 1, (middle) mode 2, and (bottom) full baroclinic velocity obtained by the first method.	52
Figure 3.19. The baroclinic velocity field for Exp_3sinsoidal: (top) mode 1, (second) mode 2, (third) mode 3, and (bottom) full baroclinic velocity obtained by the first method.	52
Figure 3.20. The baroclinic velocity field for Exp_Ref: (top) mode 1, (middle) mode 2, and (bottom) full baroclinic velocity obtained by the second method.	53
Figure 3.21. The baroclinic velocity field for Exp_3sinsoidal: (top) mode 1, (second) mode 2, (third) mode 3, and (bottom) full baroclinic velocity obtained by the second method.	53
Figure 3.22. Depth-integrated and time-averaged energy flux scaled by $P = \frac{\pi\rho_0 U_0^2 h_0^2}{8\omega_0} \sqrt{(N^2 - \omega_0^2)(\omega_0^2 - f_0^2)}$, (a) different heights of the topography, (b) different barotropic velocities, (c) different stratifications, and (d) different widths of the topography.	57
Figure 3.23. The conversion rate scaled by $P = \frac{\pi\rho_0 U_0^2 h_0^2}{8\omega_0} \sqrt{(N^2 - \omega_0^2)(\omega_0^2 - f_0^2)}$, a) different heights of the topography, b) different barotropic velocities, c) different stratifications, and d) different widths of the topography. The model C1 is calculated using the equation (3.4); the model C2 is calculated using the equation (3.5); and Theory is calculated using equations (3.7-3.8), where $\varphi(\epsilon)$ is got from the first six terms.	58
Figure 4.1. The bathymetry with two Gaussian ridges and the temperature ($^{\circ}\text{C}$) used in the model.	66
Figure 4.2. The spectra of baroclinic velocity u' for (a) Exp_K1 and Exp_1, and (b) Exp_west1, Exp_1, Exp_west2 and Exp_west3 at point $x=-120 \text{ km}$, $z=-140 \text{ m}$. Where H represents the height of the west ridge and ω represents the M2 tidal frequency. The baroclinic velocity is scaled by 0.035 m s^{-1}	68
Figure 4.3. Evolution of the energy budget calculated from Exp_1.	73
Figure 4.4. Evolution of the energy budget calculated from Exp_K1.	73
Figure 4.5. Depth-integrated and time-averaged energy fluxes for Exp_west1, Exp_1, Exp_west2 and Exp_west3. H represents the height of the west ridge.	

.....	75
Figure 4.6. Snapshots of baroclinic velocity field (m s^{-1}) after 5.9 tidal cycles, from top to bottom, the height of the west ridge (a) $H=1600$ m, (b) $H=1300$ m, (c) $H=1000$ m, and (d) $H=700$ m.	76
Figure 4.7. Time-averaged energy fluxes (from the left to the right) at Point A (-33 km), Point B (69 km), and Point C (177 km).....	77
Figure 4.8. The depth-integrated and time-averaged conversion rates for Exp_dis1, Exp_1, Exp_dis2, and Exp_dis3.	79
Figure 4.9. Depth-integrated and time-averaged energy fluxes for Exp_dis1, Exp_1, Exp_dis2, and Exp_dis3.	79
Figure 4.10. Snapshots of baroclinic velocity field (m s^{-1}) after 5.9 tidal cycles, from top to bottom, the distance between the two ridges (a) $\text{Dis}=60$ km, (b) $\text{Dis}=100$ km, (c) $\text{Dis}=140$ km, and (d) $\text{Dis}=180$ km.	80
Figure 4.11. Snapshot of temperature field after 5.9 tidal cycles, and the temperatures are $5\text{ }^{\circ}\text{C}$ (bottom line), $10\text{ }^{\circ}\text{C}$ (middle line) and $20\text{ }^{\circ}\text{C}$ (top line). The red, balck and blue lines represent the isotherms when $\text{dis}=60, 100$ and 140 km, respectively. The isotherm displacements are increased in magnitude by a factor of 2.	81
Figure 4.12. Depth-integrated and time-averaged energy fluxes for Exp_u1, Exp_u2, Exp_u3, Exp_1, and Exp_u4.	82
Figure 4.13. Snapshots of baroclinic velocity field (m s^{-1}) after 5.9 tidal cycles, from top to bottom, (a) $u=0.020\text{ m s}^{-1}$, (b) $u=0.025\text{ m s}^{-1}$, (c) $u=0.030\text{ m s}^{-1}$, (d) $u=0.035\text{ m s}^{-1}$, and (e) $u=0.040\text{ m s}^{-1}$	83
Figure 4.14. Snapshot of temperature field after 5.9 tidal cycles, and the temperatures are $5\text{ }^{\circ}\text{C}$ (bottom line), $10\text{ }^{\circ}\text{C}$ (middle line) and $20\text{ }^{\circ}\text{C}$ (top line). The red, balck and blue lines represent the isotherms when $u=0.020, 0.030$ and 0.040 m s^{-1} , respectively. The isotherm displacements are increased in magnitude by a factor of 2.	84
Figure 5.1. Map showing the bathymetry. The small black box shows the domain of the model.	91
Figure 5.2. The temperature (left) and buoyancy (right) used in models: red lines represent the temperature and buoyancy calculated from WOCE Hydrographic Climatology in standard experiments; blue lines represent the temperature and buoyancy calculated from SODA v2.24 monthly data (7,	

2008) used in Exp_Summer; black lines represent the temperature and buoyancy calculated from SODA v2.24 monthly data (1, 2008) in Exp_Winter.	91
Figure 5.3. Snapshots of baroclinic velocity (m s^{-1}) along 20.85°N after 10 M2 tidal cycles: a), b) and c) represent the baroclinic velocity calculated from Exp_Ref, Exp_Summer and Exp_Winter, respectively.	93
Figure 5.4. Left: the major axis amplitude of the M2 barotropic tidal ellipses. Right: the M2 barotropic tidal ellipses. Bathymetry contour is -1000 m.	94
Figure 5.5. From the left to the right: the depth-integrated, time-averaged conversion rate; the divergence of the depth-integrated, time-averaged baroclinic M2 energy flux and the difference between them (the divergence of the energy flux minus the conversion rate). Bathymetry contour is -1000 m. (W m^{-2}).....	99
Figure 5.6. From the left to the right: the depth-integrated, time-averaged conversion rate; the divergence of the depth-integrated, time-averaged K1 baroclinic energy flux and the difference between them (the divergence of the energy flux minus the conversion rate). Bathymetry contour is -1000 m. (W m^{-2}).....	104
Figure 5.7. The depth-integrated, time-averaged conversion rate (<-500 m, W m^{-2}), left: model result (Ref); right: using the method of Green and Nycander (2013). Bathymetry contour is -1000 m. The values in blank space are between -0.1 and 0.1 W m^{-2}	107

List of Tables

Table 2.1. The conversion rate calculated by the first method. (TW).....	27
Table 2.2. The conversion rate calculated by the second method. (TW).....	27
Table 3.1. List of cases: the values in all blank cells are the same to the Exp_Ref in the same column.	37
Table 3.2. The conversion rate scaled by $P = \frac{\pi\rho_0 U_0^2 h_0^2}{8\omega_0} \sqrt{(N^2 - \omega_0^2)(\omega_0^2 - f_0^2)}$..	58
Table 4.1. List of Experiments in this Study: the values in all blank cells are the same to the Exp_1 in the same column.....	67
Table 4.2. The baroclinic energy budget calculated from numerical experiments (W m ⁻¹).....	70
Table 5.1. The barotropic energy budget. (GW)	99
Table 5.2. The baroclinic energy budget. (GW).....	99
Table 5.3. The barotropic kinetic energy budget. (GW)	102
Table 5.4. The baroclinic kinetic energy budget. (GW).....	102
Table 5.5. The barotropic and baroclinic energy budgets (K1). (GW)	104
Table 5.6. The barotropic and baroclinic kinetic energy budgets (K1). (GW) ...	104
Table 5.7. The conversion rate. (GW).....	108
Table 5.8. The barotropic energy budget. (GW)	109
Table 5.9. The baroclinic energy budget. (GW).....	109

Chapter 1

1 Introduction

1.1 Motivation

The meridional overturning circulation (MOC) transports and redistributes mass, heat, salt, CO₂ and nutrients around the globe. The MOC has an important influence on the climate. The climate has an influence on our life. For example, the temperature in Hamburg in winter is much higher than the temperature in Asia near the sea at the same latitude, because the temperature in Hamburg in winter is largely influenced by North Atlantic Currents while in Asia is largely influenced by the cold northwest winds.

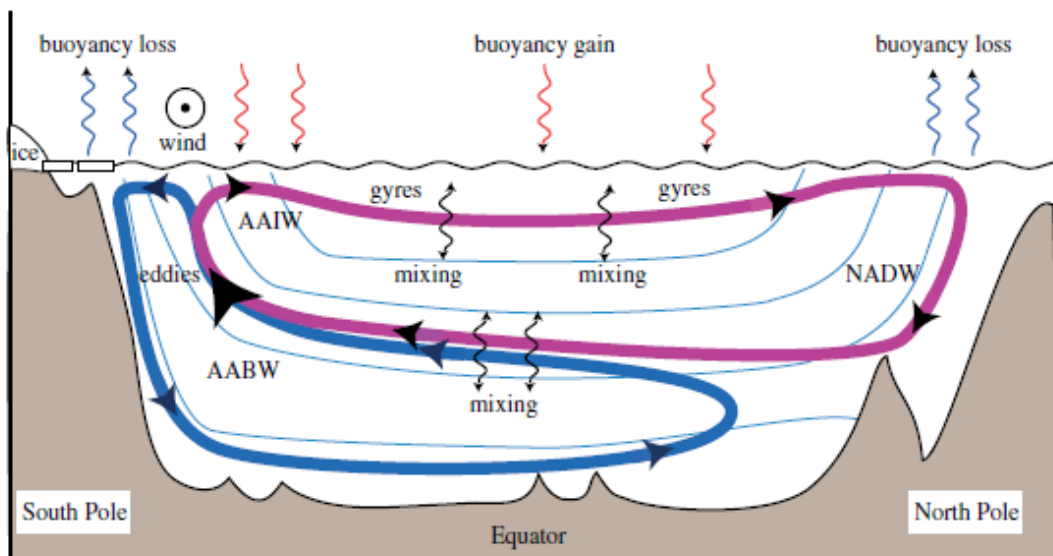


Figure 1.1. The conceptual model of MOC. AAIW stands for Antarctic Intermediate Water, AABW stands for Antarctic Bottom Water and NADW stands for North Atlantic Deep Water. From Vallis (2016).

The MOC consists of four parts: surface currents from low latitudes to high latitudes, downwelling processes at high latitudes, deep currents from high latitudes to low latitudes and upwelling processes at low latitudes. There are two mechanisms for the upwelling processes (Fig. 1.1). Firstly, diapycnal mixing caused by wave

breaking and other processes can bring the deep water to the ocean surface. The energy for diapycnal mixing is from the winds and tides, and about 2 TW are needed (Munk and Wunsch, 1998). In addition, the winds over the Southern Ocean induce northward Ekman transport. It also causes upwelling. If the upwelling processes caused by the winds over the Southern Ocean are taken into account, the required energy should be less than 2 TW (Kuhlbrodt et al., 2007).

Many motions driven by the winds and tides contribute to the diapycnal mixing. It is very important to know how much energy is transferred from the winds and tides to these motions respectively. Much previous research focused on three kinds of motions: near-inertial waves, internal lee waves and internal tides.

The near-inertial motions can be driven by winds and have been considered to be an important source for the diapycnal mixing in the deep ocean. The energy of near-inertial motions converted from winds was between 0.29 and 1.4 TW (Alford, 2001; Watanabe and Hibiya, 2002; Alford, 2003; Jiang et al., 2005; Rimac et al., 2013). However, much research pointed out that only about 0.1 TW was available for deep ocean mixing (Furuichi et al., 2008; Zhai et al., 2009), because most of energy would dissipate in the surface 200 m.

The large-scale flow and eddies can be driven by winds, and eddies can be generated by baroclinic instability. The lee waves can be generated when geostrophic flows flow over small scale topography. When the lee waves break and dissipate, the background mixing will be enhanced. For example, recently, much research (Garabato et al., 2004; Nikurashin and Ferrari, 2010a; Waterman et al., 2013; Brearley et al., 2013) suggested that the energy from geostrophic flows into internal waves may be a reason of enhanced mixing in the deep ocean. Furthermore, the energy flux into lee waves has been calculated based on linear theory (Nikurashin and Ferrari, 2011; Scott et al., 2011; Wright et al., 2014). The results showed that the conversion rate from global geostrophic flows was about between 0.2 and 0.94 TW. However, there are large uncertainties in velocity and topographic data; hence past results are still uncertain. In addition, they don't differentiate between the conversion rate from the mean flow and from eddies.

The tide force is generated by the combination of the gravitational attraction between the astronomical objects (Moon and Sun) and the Earth, and the rotation of Earth-astronomical objects systems. The energy from the barotropic tides will be either converted to the baroclinic tides or dissipated in oceanic regions. The internal

tides can be generated by barotropic tides over bottom topography. After the internal tide generation, low mode internal tides tend to propagate away from the generation sites and high mode internal tides tend to dissipate locally because of their low speeds and high shear. Egbert and Ray (2001) calculated the dissipation rate of the tides defined as the working rate by tidal forces subtracting the energy flux divergence using altimeter data. They estimated that about 1TW of power was lost from barotropic tides in the deep ocean. The dissipation of barotropic tides calculated by Egbert and Ray (2001) refers to the lost energy of barotropic tides and it can't distinguish the difference between the conversion rate from barotropic tides to baroclinic tides and the dissipation of barotropic and baroclinic tides.

Linear theory has been used to study internal tide generation. Bell (1975a) derived the conversion rate in an ocean of infinite depth based on weak topography approximation. Balmforth et al. (2002) derived the conversion rate for several topographies, and the conversion rate of subcritical sinusoidal topography was about 56% larger than the Bell's theory (Bell, 1975a). It was extended to the supercritical topography cases in Balmforth and Peacock (2009). In general, these studies (Bell 1975a, b; Balmforth et al., 2002; Llewellyn Smith and Young, 2002; Khatiwala, 2003; Párrdis et al., 2006; Balmforth and Peacock, 2009) have used different mathematical methods to derive the conversion rate and extended the linear theory to cases with different topographies based on different assumptions.

Nycander (2005) calculated the conversion rate directly using data from TPXO 6 basing on the theory (Bell 1975a,b; Llewellyn Smith and Young, 2002) and got that about 1.2 TW was transferred from barotropic tides to internal waves over areas with a depth greater than 500 m, which compared well with the results (Egbert and Ray, 2001). However, both above calculations of global tidal dissipation are using a coarse resolution. The strong tides may occur in regions such as Luzon ridge, in which the calculations in a coarse resolution are not reliable and numerical simulations in a higher resolution are needed.

Numerical models are also used to study the internal tide generation. Some ideal models have been set up to compare the conversion rates calculated by numerical simulations with the values predicted by the linear theory (Legg and Huijts, 2006; Di Lorenzo et al., 2006). Legg and Huijts (2006) used nonhydrostatic MITgcm to simulate the barotropic flow over an isolated Gaussian topography. In their paper, the cases could be divided into four different situations due to different topographies.

Model results showed that the conversion rates predicted by the linear theory (bell, 1975b) agreed well with results using ‘low, wide’ topography. The conversion rates calculated from supercritical cases were much larger than the results predicted by the linear theory. Di Lorenzo et al. (2006) used the Regional Ocean Modeling System (ROMS) to simulate the barotropic tide over polynomial ridge topography, and compared the model results with the values calculated using the theory (Petrelis et al., 2006). Results showed that the model results agreed well with the values predicted by the theory. Note that these two works have used different definitions of conversion rate, different models and different topographies.

Much research has used numerical models to study the energetics of internal tides for a certain region (Merrifield and Holloway, 2002; Jachec et al., 2006; Green et al., 2008; Buijsman et al., 2012b; Tanaka et al., 2013). Above studies except Tanaka et al. (2013) mainly focused on the energy flux part. In addition, the energy budget of internal tides has been developed. Cater et al. (2008) derived barotropic and baroclinic energy equations based on Princeton Ocean Model (POM), and applied the theory at the Hawaii Islands. Zaron and Egbert (2006) derived the barotropic and baroclinic kinetic energy equations from linearized primitive equations. Ponte and Cornuelle (2013) used MITgcm to study the kinetic energy budgets around Point Loma in San Diego, California. Kang and Fringer (2012) derived barotropic and baroclinic energy equations including the potential energy parts in a different way. Through analyzing the energy budgets, we can know the spatial distribution and pathway of the energies of internal tides for a certain region.

The Luzon strait connects the South China Sea to the Western Pacific Ocean and features two meridional ridges. It is an important generation site of the internal tides both at diurnal and semidiurnal periods (Niwa and Hibiya, 2004; Jan et al., 2007; Jan et al., 2008). Niwa and Hibiya (2004) studied the M2 internal tide in the East China Sea including the Luzon ridge using the three-dimensional POM. It was found that the baroclinic conversion rate and the energy flux of the internal tide at the Luzon ridge were 14.9 and 9.0 GW, respectively. Kerry et al. (2014) calculated the conversion rate of the internal tide based on ROMS and found that the mean conversion rate at the Luzon ridge over 2010 was 16.21 GW. Zhao (2014) calculated the depth-integrated energy flux using altimetric dataset by equations derived from linear theory. The results showed that the energy fluxes of mode-1 M2, K1 and O1 internal tides at the Luzon ridge were 2.7, 2.5 and 1.8 GW, respectively. However,

only part of the energetics of internal tides at the Luzon ridge has been studied, the full energy budget of internal tides is still unclear.

In this paper, we try to answer the following questions:

- 1, what is the difference between the conversion rates of lee waves generated by the mean flow and eddies?
- 2, do the conversion rates of tides predicted by the linear theory (Balmforth et al., 2002) compare well with the results calculated from numerical simulations?
- 3, what are the energy budgets of internal tides at the Luzon ridge?

In order to answer the above questions, firstly, the conversion rates from different velocity databases are calculated, and the sensitivities to the steepness and topographic spectrum are studied. Secondly, experiments with an ideal sinusoidal topography are set up to test the linear theory. The comparison of the conversion rates calculated from numerical simulations and the results predicted by the theory (Balmforth et al., 2002) will be discussed. At last, two- and three-dimensional simulations are set up at the Luzon ridge to obtain the energy budgets of internal tides.

1.2 The lee waves

The lee waves can be generated by a constant flow over bottom topography. Considering small amplitude topography, a uniform velocity U in the x direction and stratification N , the linearized equation for internal lee waves can be obtained (Gill 1982; Nikurashin and Ferrari, 2010a),

$$U \frac{\partial u}{\partial x} - fv = -\frac{1}{\rho_0} \frac{\partial p'}{\partial x}, \quad (1.1)$$

$$U \frac{\partial v}{\partial x} + fu = 0, \quad (1.2)$$

$$U \frac{\partial w}{\partial x} = -\frac{1}{\rho_0} \frac{\partial p'}{\partial z} - \frac{g}{\rho_0} \rho', \quad (1.3)$$

$$\frac{\partial u}{\partial x} + \frac{\partial w}{\partial z} = 0, \quad (1.4)$$

$$U \frac{\partial \rho'}{\partial x} = \frac{\rho_0}{g} N^2 w, \quad (1.5)$$

$$N^2(z) = -\frac{g}{\rho_0} \frac{d\rho_0}{dz}. \quad (1.6)$$

Where (u, v, w) is the wave velocity, ρ_0 is the constant reference density.

The full pressure is given by

$$p = \bar{p}_0 + p', \quad (1.7)$$

where p' is the perturbation pressure and the full density is given by

$$\rho = \bar{\rho}_0 + \rho', \quad (1.8)$$

where ρ' is the perturbation density. f is the Coriolis frequency. Solving equations (1.1)-(1.6) for w gives

$$U^2 \frac{\partial^2}{\partial x^2} \left(\frac{\partial^2}{\partial x^2} w + \frac{\partial^2}{\partial z^2} w \right) + N^2 \frac{\partial^2}{\partial x^2} w + f^2 \frac{\partial^2}{\partial z^2} w = 0. \quad (1.9)$$

Assuming the topography $h=h_1 \cos kx$, we seek solutions of the form

$$w = e^{i(kx+mz)}. \quad (1.10)$$

Substituting (1.10) to (1.9), one can obtain the dispersion relation for the lee waves,

$$m^2 = k^2 \frac{N^2 - U^2 k^2}{U^2 k^2 - f^2}. \quad (1.11)$$

When the frequency Uk is in the range $f < Uk < N$, lee waves are generated.

For sinusoidal topography, the energy flux of lee waves averaged over a wavelength can be expressed (Gill 1982),

$$C_{-1} = \int p'(x, -z, t) U \frac{dh}{dx} dx = \frac{\rho_0 U h_0^2}{8} \sqrt{(N^2 - U^2 k^2)(U^2 k^2 - f^2)}, \quad (1.12)$$

where h_0 is the maximum height of the sinusoidal topography. Then the lee waves energy flux for sinusoidal topography can got by integrating (1.12) over the wavenumber range $f/U < k < N/U$. As pointed in the studies (Nikurashin and Ferrari, 2010a, 2011), the inverse Froude number $Fr^{-1} = h_0 m \approx N h_0 / U$ is the fundamental nondimensional parameter for the internal lee waves. When $Fr^{-1} < 1$, the generation of lee waves will be linear. When $Fr^{-1} \sim 1$, nonlinear effect will become important, and when $Fr^{-1} > 1$, the energy flux will decrease.

Much recent research has focused on the internal lee waves. Nikurashin and Ferrari (2010a, b) extended the linear theory, derived a set of equations to study the feedback of waves on the flow in physics, and suggested that the enhanced mixing in Drake Passage can be supported by radiation and dissipation of the lee waves generated by geostrophic flows over topography. Nikurashin and Ferrari (2011) used the linear theory (Bell, 1975a) to calculate the global conversion rate. The single beam sounding, bottom stratification from WOCE, and bottom velocity from global model were used. They showed that the conversion rate was about 0.2 TW. Scott et al. (2011) calculated the conversion rate based on the theory (Gill 1982, chapter 8). They used two different topographic data sets (GA2010 and G2010), bottom velocity

from HYCOM, and stratification from WOA2009. They showed that the conversion rate was between 0.34 and 0.49 TW, and 92% of the lee wave energy generated in the South Hemisphere. However, Wright et al. (2013) suggested that the generation rate of internal lee waves would be 0.75 ± 0.19 TW.

The breaking and dissipation of internal lee waves contribute to the diapycnal mixing. However, the scale of the processes is too small for ocean circulation models to resolve; hence we need to parameterize the subgrid motions. Melet et al. (2014) set up a series of experiments using the Geophysical Fluid Dynamics Laboratory CM2G ocean-ice-atmosphere coupled model including a parameterization of lee wave-driven mixing and showed that the lee waves generated by geostrophic flows had a significant impact on the ocean state. The effects should be further verified because the exact conversion rate of lee waves is still a wide open question, and the vertical structure and process of dissipation of lee waves are still not clear.

1.3 The internal tides

1.3.1 The linear internal wave theory

Linear theory can be used to describe internal waves. After neglecting the nonlinear terms, the Euler equations with the Boussinesq approximation reduce to

$$\frac{\partial u}{\partial t} - fv = -\frac{1}{\rho_0} \frac{\partial p'}{\partial x}, \quad (1.13)$$

$$\frac{\partial v}{\partial t} + fu = -\frac{1}{\rho_0} \frac{\partial p'}{\partial y}, \quad (1.14)$$

$$\frac{\partial w}{\partial t} = -\frac{1}{\rho_0} \frac{\partial p'}{\partial z} - \frac{g}{\rho_0} \rho', \quad (1.15)$$

$$\frac{\partial u}{\partial x} + \frac{\partial v}{\partial y} + \frac{\partial w}{\partial z} = 0, \quad (1.16)$$

$$\frac{\partial \rho'}{\partial t} = \frac{\rho_0}{g} N^2 w, \quad (1.17)$$

$$N^2(z) = -\frac{g}{\rho_0} \frac{d\bar{\rho}_0}{dz}. \quad (1.18)$$

Where (u, v, w) is the wave velocity, ρ_0 is the constant reference density. The full pressure $p = \bar{p}_0 + p'$, and the full density $\rho = \bar{\rho}_0 + \rho'$, where ρ' is the perturbation density and p' is the perturbation pressure. f is the Coriolis frequency. Solving equations (1.1)-(1.6), we can get the equation for w alone,

$$\frac{\partial^2}{\partial t^2} \nabla^2 w + N^2 \nabla_H^2 w + f^2 \frac{\partial^2}{\partial z^2} w = 0. \quad (1.19)$$

Where the Laplace operator ∇^2 and horizontal component ∇_H^2 are

$$\nabla^2 = \frac{\partial^2}{\partial x^2} + \frac{\partial^2}{\partial y^2} + \frac{\partial^2}{\partial z^2}, \quad (1.20)$$

$$\nabla_H^2 = \frac{\partial^2}{\partial x^2} + \frac{\partial^2}{\partial y^2}. \quad (1.21)$$

We suppose solutions of the form

$$w = e^{i(kx+ly+mz-\omega t)}. \quad (1.22)$$

Where k and l are the horizontal wavenumbers in x - and y -direction, m is the vertical wavenumber, and ω is the frequency of the wave. Substituting (1.22) into (1.19), we get the dispersion relation for internal waves,

$$\omega^2 = \frac{(k^2+l^2)N^2+m^2f^2}{k^2+l^2+m^2}. \quad (1.23)$$

If we calculate the phase and group velocities in vector and multiply them, we can get

$$\vec{c} \cdot \vec{c}_g = 0. \quad (1.24)$$

The group velocity and the phase velocity are perpendicular to each other. Where $\vec{c} = \frac{\omega}{K}$ is the phase velocity, $\vec{c}_g = \frac{\partial \omega}{\partial K}$ is the group velocity, and $K=(k, l, m)$ is the wavenumber vector.

The vertical modes of the velocity can be got as follows. Assuming the internal waves propagate horizontally, we seek the solutions of the form

$$w = W(z)e^{i(kx+ly-\omega t)}. \quad (1.25)$$

$$W(z)=0, \text{ when } z=0, -H. \quad (1.26)$$

Substituting (1.25) into (1.19), we can get

$$W_{zz} + (k^2 + l^2) \left(\frac{N^2 - \omega^2}{\omega^2 - f^2} \right) W = 0. \quad (1.27)$$

If N is not constant, we can solve the equations (1.25)-(1.27) numerically. If N is constant, we define

$$m^2 = (k^2 + l^2) \left(\frac{N^2 - \omega^2}{\omega^2 - f^2} \right). \quad (1.28)$$

The equation becomes

$$W_{zz} + m^2 W = 0. \quad (1.29)$$

The general solutions of the equation (1.29) are

$$W_n = a1 \sin(mz) + a2 \cos(mz). \quad (1.30)$$

Considering the equations (1.26), the boundary conditions become

$$a2=0, \quad (1.31)$$

$$-a1 \sin(mH)=0. \quad (1.32)$$

If the solutions exist, hence

$$m_n = \frac{n\pi}{H}. \quad (1.33)$$

Now, the solutions of the eigenvalue problem (1.27) can be written in

$$W_n = a \sin\left(\frac{n\pi z}{H}\right), n=0, 1, 2, 3, \dots \quad (1.34)$$

The wave frequency can be written in

$$\omega^2 = \frac{(k^2+l^2)N^2H^2+n^2\pi^2f^2}{(k^2+l^2)H^2+n^2\pi^2}, n= 1, 2, 3, \dots \quad (1.35)$$

The horizontal phase velocity is obtained

$$c = \frac{\omega}{(k^2+l^2)^{\frac{1}{2}}} = \frac{H\omega}{n\pi} \left(\frac{N^2-\omega^2}{\omega^2-f^2}\right)^{\frac{1}{2}}, \quad (1.36)$$

and the horizontal group velocity is obtained

$$\vec{c}_g = \left(\frac{\partial\omega}{\partial k}, \frac{\partial\omega}{\partial l}\right) = \frac{H}{n\pi} \frac{(\omega^2-f^2)^{\frac{1}{2}}(N^2-\omega^2)^{\frac{3}{2}}}{(k^2+l^2)^{\frac{1}{2}}\omega(N^2-f^2)}(k, l). \quad (1.37)$$

The energy equation can be got from the sets of equations (1.13)-(1.18)

$$\frac{1}{2}\rho_0 \frac{\partial}{\partial t}(u^2 + v^2 + w^2 + N^{-2}b^2) + u \frac{\partial p'}{\partial x} + w \frac{\partial p'}{\partial z} = 0. \quad (1.38)$$

Because there is no y dependence, we multiply the equation (1.16) with p' , then obtain

$$p' \left(\frac{\partial u}{\partial x} + \frac{\partial w}{\partial z}\right) = 0. \quad (1.39)$$

Combining equations (1.38) - (1.39), we get

$$\frac{1}{2}\rho_0 \frac{\partial}{\partial t}(u^2 + v^2 + w^2 + N^{-2}b^2) + \frac{\partial up'}{\partial x} + \frac{\partial wp'}{\partial z} = 0. \quad (1.40)$$

1.3.2 The conversion rate of internal tides

We define $b = -g \frac{p'}{\rho_0}$ and assume $\frac{\partial}{\partial y} = 0$, then the equations (1.13)-(1.18) will be the same equations which have been used in Balmforth et al. (2002). The internal tides can be generated by barotropic flow over bottom topography in a stratified fluid. The barotropic tides can be prescribed through linearized boundary conditions,

$$w(x, 0, t) = 0, \quad (1.41)$$

$$w(x, -z, t) = U \cdot \nabla h. \quad (1.42)$$

The conversion rate can be calculated by

$$C = \int p'(x, -z, t) U \frac{dh}{dx} dx. \quad (1.43)$$

If we have the solutions of the p' , U and $\frac{dh}{dx}$, C can be obtained. For this part, different people used different methods to deal with it. Balmforth et al. (2002) used the stream function to deal with the equations, and the conversion rate of tides over sinusoidal topography averaged over one tidal period $2\pi/\omega_0$ is given by

$$C_{-2} = \frac{\pi \rho_0 U_0^2 h_0^2}{8 \omega_0} \sqrt{(N^2 - \omega_0^2)(\omega_0^2 - f_0^2)} \varphi(\epsilon), \quad (1.44)$$

$$\varphi(\epsilon) = 1 + \frac{\epsilon^2}{4} + \frac{11\epsilon^4}{96} + \frac{143\epsilon^6}{2304} + \frac{4513\epsilon^8}{122880} + \frac{170791\epsilon^{10}}{7372880} + O(\epsilon^{12}), \quad (1.45)$$

when $\epsilon < 1$. Where μ is the multiplicative inverse of the slope of internal wave beam and $\mu = \sqrt{\frac{N^2 - \omega_0^2}{\omega_0^2 - f_0^2}}$. ϵ is the nondimensional parameter $\epsilon = \frac{dh}{dx} * \mu$. ρ_0 is the reference density, U_0 is the barotropic velocity and h_0 is the maximum height of the sinusoidal topography. More detailed information about dealing with the formulas can be found in the following studies (Balmforth et al., 2002; Llewellyn Smith and Young, 2002; Khatiwala, 2003; P  r  dis et al., 2006; Balmforth and Peacock, 2009).

1.3.3 The energy budgets of internal tides

The barotropic and baroclinic energy equations derived by Kang and Fringer (2012) are shown as follows. The Reynolds-averaged form of the Navier-Stokes equation with Boussinesq approximation gives

$$\frac{\partial u}{\partial t} + \mathbf{u} \cdot \nabla u - fv + 2\Omega \cos\theta w = -\frac{1}{\rho_0} \frac{\partial p}{\partial x} + \nabla_H \cdot (A_h \nabla_H u) + \frac{\partial}{\partial z} (A_v \frac{\partial u}{\partial z}), \quad (1.46)$$

$$\frac{\partial v}{\partial t} + \mathbf{u} \cdot \nabla v + fu = -\frac{1}{\rho_0} \frac{\partial p}{\partial y} + \nabla_H \cdot (A_h \nabla_H v) + \frac{\partial}{\partial z} (A_v \frac{\partial v}{\partial z}), \quad (1.47)$$

$$\frac{\partial w}{\partial t} + \mathbf{u} \cdot \nabla w - 2\Omega \cos\theta u = -\frac{1}{\rho_0} \frac{\partial p}{\partial x} + \nabla_H \cdot (A_h \nabla_H w) + \frac{\partial}{\partial z} (A_v \frac{\partial w}{\partial z}) - \frac{g\rho}{\rho_0}, \quad (1.48)$$

$$\frac{\partial u}{\partial x} + \frac{\partial v}{\partial y} + \frac{\partial w}{\partial z} = 0, \quad (1.49)$$

$$\frac{\partial \rho}{\partial t} + \mathbf{u} \cdot \nabla \rho = \nabla_H \cdot (K_h \nabla_H \rho) + \frac{\partial}{\partial z} (K_v \frac{\partial \rho}{\partial z}), \quad (1.50)$$

where $\mathbf{u}=(u,v,w)$ is the velocity vector, the Coriolis term $f=2\Omega \sin\theta$ and Ω is the earth's angular velocity. The total density is given by

$$\rho(x, y, z, t) = \rho_0 + \rho_v(z) + \rho'(x, y, z, t), \quad (1.51)$$

where ρ_0 is the constant reference density, ρ_v is the background density, ρ' is the perturbation density, p is the pressure. A_h and A_v are the horizontal and vertical eddy viscosity. K_h and K_v are the horizontal and vertical eddy diffusivity. The full pressure is given by

$$\begin{aligned} p(x, y, z, t) &= p_0 + p_v(z) + p'(x, y, z, t) + q, \\ &= \rho_0 g(\eta - z) + g \int_z^\eta \rho_v dz + g \int_z^\eta \rho' dz + q, \end{aligned} \quad (1.52)$$

where p_0 is the reference pressure, p_v is the background pressure, q is the nonhydrostatic pressure, and η is the free surface elevation. In order to obtain the barotropic and baroclinic energy equations, the velocity is divided into barotropic and baroclinic parts. The full velocity $\mathbf{u}=(u, v, w)$, and the barotropic velocity $\mathbf{U}=(U, V, W)$. The baroclinic velocity is defined by

$$\mathbf{u}'(x, y, z, t) = \mathbf{u}(x, y, z, t) - \mathbf{U}(x, y, z, t). \quad (1.53)$$

Where the horizontal barotropic velocities can be obtained by

$$\mathbf{U}_h = \frac{1}{\eta+h} \int_{-h}^\eta \mathbf{u}_h(x, y, z, t) dz. \quad (1.54)$$

Where h is the depth of ocean. The continuity equation for (U, V, W) gives

$$\frac{\partial U}{\partial x} + \frac{\partial V}{\partial y} + \frac{\partial W}{\partial z} = 0. \quad (1.55)$$

The boundary condition on the bottom is

$$-\mathbf{U}_h \cdot \nabla_H h = W, \quad \text{when } z = -d. \quad (1.56)$$

Combining (1.55) and (1.56), the vertical barotropic velocity can be obtained by

$$W(z) = -\nabla_H \cdot ((z+h)\mathbf{U}_h). \quad (1.57)$$

Decomposition goes a series of processes, and we can obtain the barotropic and baroclinic equations. The depth-integrated barotropic equation reads

$$\frac{\partial}{\partial t} (\overline{E_{kb}} + \overline{E_{pb}}) + \nabla_H \cdot \overline{\mathbf{F}_b} = -\overline{C} - \overline{\varepsilon_b} - \overline{R_b}. \quad (1.58)$$

Where the barotropic kinetic energy is

$$E_{kb} = \frac{1}{2} \rho_0 (U^2 + V^2), \quad (1.59)$$

the depth-integrated potential energy due to surface elevation is

$$\overline{E_{pb}} = \frac{1}{2} \rho_0 g \eta^2, \quad (1.60)$$

the depth-integrated barotropic energy flux is

$$\overline{\mathbf{F}_b} = \mathbf{U}_h \overline{E_{kb}} + \mathbf{U}_h H \rho_0 g \eta + \mathbf{U}_h \overline{p'} + \mathbf{U}_h \overline{q} - \overline{A_h \nabla_H E_{kb}}, \quad (1.61)$$

the depth-integrated conversion rate is

$$\bar{C} = \overline{\rho' g W} - \overline{\frac{\partial q}{\partial z} W}, \quad (1.62)$$

and the barotropic dissipation term is

$$\bar{\varepsilon}_b = \rho_0 A_h \nabla_H \mathbf{U}_h \cdot \nabla_H \mathbf{U}_h. \quad (1.63)$$

\bar{R}_b contains the bottom drag and nonlinear conversion rate term. The depth-integrated baroclinic equation reads

$$\frac{\partial}{\partial t} (\bar{E}_k + \bar{E}_p) + \nabla_H \cdot \bar{\mathbf{F}} = \bar{C} - \bar{\varepsilon} - \bar{R}, \quad (1.62)$$

where the baroclinic kinetic energy is

$$E_k = \frac{1}{2} \rho_0 (u'^2 + v'^2 + w^2), \quad (1.63)$$

the available potential energy is

$$E_p = \frac{g^2 \rho'^2}{2 \rho_0 N^2}, \quad (1.64)$$

the cross kinetic energy is

$$E_{hk} = \rho_0 (U u' + V v'), \quad (1.65)$$

the depth-integrated baroclinic energy flux is

$$\bar{\mathbf{F}} = \overline{\mathbf{u}'_h p'} + \overline{\mathbf{u}'_h q} + \overline{\mathbf{u}'_h (E_k + E_p)} + \overline{\mathbf{u}'_h E_{hk}} - \overline{A_h \nabla_H E_k} - \overline{K_h \nabla_H E_p}, \quad (1.66)$$

and the baroclinic dissipation term is

$$\bar{\varepsilon} = \rho_0 A_h \nabla_H \mathbf{u}'_h \cdot \nabla_H \mathbf{u}'_h + \rho_0 A_v \frac{\partial \mathbf{u}'_h}{\partial z} \cdot \frac{\partial \mathbf{u}'_h}{\partial z} + \rho_0 A_h \nabla_H W \cdot \nabla_H W + \rho_0 A_v \frac{\partial w}{\partial z} \cdot \frac{\partial w}{\partial z}. \quad (1.67)$$

\bar{R} contains the dissipation of E_p , the bottom drag term and nonlinear conversion rate term.

1.4 The internal waves at the Luzon ridge

1.4.1 The internal tides

The Luzon strait connects the South China Sea to the west Pacific Ocean. It features two meridional ridges which contain a number of islands. Strong diurnal and semidiurnal internal tides are generated, when the barotropic tides flow over bottom topography. Then, part of the internal tides will dissipate locally. Part of the internal tides will either propagate into Pacific Ocean or into the South China Sea. Internal tides may evolve into solitary waves in the northern of South China Sea.

Much research has used numerical models to study the internal tide generation

and focused the energy flux and conversion rate at the Luzon ridge. Niwa and Hibiya (2004) used POM to study the M2 internal tide in the East China Sea. The baroclinic conversion rate at the Luzon ridge was 14.9 GW, the baroclinic energy flux was 9.0 GW, and the baroclinic dissipation rate was 5.9 GW in their EXP. A. The results didn't change too much, when the horizontal resolution, vertical level number and topography averaging radius changed small. Jan et al. (2008) used Princeton Ocean Model to study the baroclinic tides at the Luzon ridge. They calculated the barotropic and baroclinic energy flux and the conversion rate from barotropic flow to the baroclinic flow. Their results showed that the conversion rates for (O1 + K1) and (M2 + S2) were about 19 GW and 11GW, respectively, and 50% of the baroclinic tides generated was dissipated locally; about 12 GW for K1 barotropic tide was lost: the conversion rate was about 11 GW, and the barotropic dissipation was about 1 GW; about 18 GW of M2 barotropic tide was lost: the conversion rate was about 10 GW, and the barotropic dissipation was about 8 GW. Buijsman et al. (2014) used both two-dimensional and three-dimensional MITgcm to study the internal tide resonance. Their models were forced by eight barotropic tidal currents at the boundaries. They separated the conversion rate into semidiurnal and diurnal parts and found that most of resonance occurs for the first mode. Kerry et al. (2014) used ROMS to study the conversion rate from M2 barotropic tide to baroclinic tide in the Philippine Sea. The mean conversion rate at the Luzon strait over 2010 was 16.21 GW. Zhao (2014) calculated the energy flux for M2, K1, and O1 using the sea surface height measurements by multiple satellites ERS-2, Envisat, TOPEX/Poseidon, Jason-1/2, and Geosat Follow-On. His results showed that the energy fluxes for Mode-1 of M2, K1, and O1 were 2.7, 2.5 and 1.8 GW, respectively. Much research has also focused on the internal tides at the Luzon ridge (Jan et al., 2007; Alford et al., 2011; Jan et al., 2012). To sum up, the conversion rate of M2 tide calculated at the Luzon ridge was about 10~20 GW, and the energy flux of M2 tide was about 2~10 GW.

1.4.2 The internal solitary waves

The KDV equation is usually used to study the solitary waves. Nonlinearity and dispersion are the two important effects for the existence of a soliton solution. For interfacial wave, it usually can be described by the following formula

$$\frac{\partial \eta}{\partial t} + c_0 \frac{\partial \eta}{\partial x} + \frac{3}{2} \frac{h_1 - h_2}{h_1 h_2} c_0 \eta \frac{\partial \eta}{\partial x} + \frac{1}{6} c_0 h_1 h_2 \frac{\partial^3 \eta}{\partial x^3} = 0. \quad (1.68)$$

Where η is the surface height, h_1 and h_2 are the thickness of the upper and lower layer, respectively. $c_0^2 = g' \frac{h_1 h_2}{h_1 + h_2}$ is the linear long-wave speed. (Gerkema and Zimmerman, 2008)

The solitary waves have not only been studied in theory, but also studied by numerical simulations. There are strong internal tides at the Luzon ridge, and these can cause strong nonlinear internal waves in the Northern South China Sea.

Much research has focused on the solitons here. Cai et al. (2002) used a generation model of the internal tides and a long wave propagation model to study the generation and evolution of internal solitary waves at the Luzon ridge. They showed that only when the amplitude of the internal tide was large enough that the train of internal solitary waves would be generated. They also pointed out that shoaling effect, asymmetry of the depth profile and channel width had an influence on the internal waves generated. Nonlinear wave was described at the continental slope in the Northern South China Sea using the mooring during the period April-May 2001 in Duda et al. (2004). Type-a and Type-b packets were described in this research. Warn-Varnas et al. (2010) studied the generation of solitary waves with 2.5 dimensional nonhydrostatic model. Alford et al. (2010) studied the nonlinear internal waves transiting the South China Sea in detailed using data from mooring during the period 26 April- 7 May 2007. Type-a and Type-b waves were also found in their research. Buijsman et al. (2010a) used ROMS to study the nonlinear internal waves in the South China Sea. In this research the topography was represented by an ideal Gaussian ridge. One of the mechanisms of the generation of solitary waves was that the eastward flow created a first-mode warm front on the east side that, as it propagated eastward, steepened and evolved into a weak soliton train. Buijsman et al. (2010b) used ROMS to study the nonlinear waves in the Luzon Strait in an idealized two-dimensional simulation. They studied many factors influencing the generation of nonlinear waves including the distance between two ridges, Kuroshio and the heights of the ridges. The nonlinear internal waves in the northern South China Sea also have been studied in the studies (Zhao et al., 2004; Lien et al., 2005; Zhao and Alford., 2006; Shaw et al., 2009; Farmer et al., 2009; Li and Farmer, 2011). These studies have shown that a train of solitons can be generated when a strong enough low-mode internal tide steepens by nonlinear effects.

1.5 Overview of the thesis

The thesis is organized as follows.

In Chapter 2, we calculate the conversion rate of internal lee waves generated by geostrophic flows based on linear theory. The single beam sounding depth data and global predicted abyssal hill rms heights, WOCE hydrographic atlas, velocity data from SODA and ECCO2 and mean flow and eddy velocity from the global eddy-permitting STORM model on a $1^\circ \times 1^\circ$ grid are used.

In Chapter 3, we set up a series of experiments to investigate the baroclinic flow generated by barotropic flow over an ideal sinusoidal topography. A comparison of the conversion rates calculated from numerical simulations and the results predicted by the theory (Balmforth et al., 2002) is presented.

In Chapter 4, the two-dimensional numerical simulations of internal waves using MITgcm at the Luzon ridge are presented. The two meridional ridges in the Luzon region are represented by two ideal Gaussian ridges and the stratification used in these simulations is calculated using WOCE climatology in 20.5°N . The energy budget from the baroclinic equation derived by Kang and Fringer (2010) is shown in this chapter.

In Chapter 5, three-dimensional simulations of internal tides in Luzon region are presented. The M2 tidal ellipses and the energy budgets from both barotropic energy equation and baroclinic energy equation derived by Kang and Fringer (2010) and from both barotropic kinetic energy equation and baroclinic kinetic energy equation are shown.

Chapter 2

2 The conversion rate of internal lee waves generation by global geostrophic flows

Abstract

The conversion rate of internal lee waves generated by geostrophic flows is calculated based on linear theory. The single beam sounding depth data, global predicted abyssal hill rms heights, WOCE hydrographic atlas, velocity data from SODA and ECCO2, mean flow and eddy velocity from the global eddy-permitting STORM model in a $1^\circ \times 1^\circ$ grid are used for the calculations. Here, we use two different methods to deal with the topographic spectrum calculated using single beam sounding depth data. The first method is aimed to obtain topographic spectra in $3^\circ \times 3^\circ$ global grid cells firstly by averaging spectra from different segments. The second method is calculating the conversion rate using the spectrum for each segment. The conversion rates calculated using SODA, ECCO2, mean flow and eddy velocity from the global eddy-permitting STORM model are between 0.03 and 0.23 TW using the two methods. The difference between the conversion rate from the eddies and from the mean flow is between 0.05 and 0.11 TW.

2.1 Introduction

The meridional overturning circulation (MOC) transports and redistributes mass, heat, salt, CO₂ and nutrients around the globe and has an important influence on the climate. Diapycnal mixing caused by wave breaking and other processes can bring the deep water to the ocean surface and plays a crucial role in sustaining the MOC. The energy for diapycnal mixing is from the winds and tides, and about 2 TW are needed (Munk and Wunsch, 1998). The internal tides and internal lee waves generated in deep ocean contribute to the process (Egbert and Ray, 2001; Garabato et al., 2004; Nikurashin and Ferrari, 2010a; Waterman et al., 2013; Brearley et al., 2013).

The energy work on the large-scale flow and eddies from winds is about 1.0 TW

(Wunsch, 1998). Much of the energy will be transferred into eddies. The eddy energy can dissipate through several processes. For example, about 0.2-0.8 TW eddy energy is lost due to bottom drag (Sen et al., 2008). In addition, the lee waves are generated when the geostrophic flows flow over the ocean bottom, and propagate away from the generation sites (Bell, 1975a). This process can transfer the eddy energy to small scale. The total energy flux into internal lee waves was found to be about 0.2-0.94 TW based on linear theory (Nikurashin and Ferrari, 2011; Scott et al., 2011; Wright et al., 2014) and the Southern Hemisphere produced most of lee wave energy. However, there are large uncertainties in velocity and topographic data, both of which have large influences on the conversion rate; hence past results are still uncertain. In addition, the difference between the conversion rate from eddies and from the mean flow hasn't been given in the previous studies.

Waterman et al. (2012) showed that the conversion rate predicted by the theory (Nikurashin and Ferrari, 2011) was much larger than the observed dissipation in a region north of the Kerguelen Pkateau, which was also supported by Nikurashin et al. (2014). The disagreement between linear theory and observations may be explained in many ways. For example, much of the energy may propagate away from the generation sites, the linear theory may ignore some finite topography effects and there are limitations for the topographic spectrum (Waterman et al., 2013; Nikurashin et al., 2014). The influences of the former two factors are hard to be quantified, but here we develop a method to test the sensitivity to the topographic spectrum.

The purpose of the paper is to test the sensitivities of conversion rate to the velocity and to the topographic spectrum, and differentiate between the conversion rate from eddies and from the mean flow. Two different topography databases, velocity data from SODA and ECCO2, mean flow and eddy velocity from the global eddy-permitting STORM model are used to finish the calculations.

2.2 Theory

The energy transferred from geostrophic flows to internal lee waves in small scale topography can be calculated by the following formula (Bell, 1975a; Nikurashin and Ferrari, 2011; Nikurashin et al., 2014).

$$E = \frac{\rho_0 |\mathbf{U}|}{\pi} \int_{|f|/|\mathbf{U}|}^{N/|\mathbf{U}|} P_*(k) \sqrt{N^2 - |\mathbf{U}|^2 k^2} \sqrt{|\mathbf{U}|^2 k^2 - f^2} dk. \quad (2.1)$$

Where the reference density $\rho_0=1045 \text{ kg m}^{-3}$, U is the bottom velocity, N is the bottom stratification, f is the Coriolis frequency and $P_*(k) = \frac{1}{2\pi} \int_{-\infty}^{+\infty} \frac{|k|}{|\mathbf{k}|} P(k, l) dl$ is the effective topographic spectrum, where $k= (k, l)$ is the wavenumber in the reference frame along and across the mean flow U .

We define the steepness $\epsilon = \frac{NH}{|U|}$, where H is the topographic height, and set $\epsilon_0=0.7$ as the critical steepness parameter as done by Nikurashin and Ferrari (2011). Because the linear theory is derived based on subcritical topography, the expression is multiplied by $(\epsilon_0/\epsilon)^2$ at all locations whenever $\epsilon > 0.7$, in order to account for the suppression of energy conversion at supercritical topography. It's not an exact method, so we want to test the sensitivity of the conversion rate to the steepness. Here, the amplitude of the topography H is defined in two ways. The first way is $H = \sqrt{2}h_{\text{range}}$, as done by Nikurashin and Ferrari (2011), where h_{range} is the rms height of the topography in the radiative wavenumber range. The second way is $H = h_0$, where h_0 is the topographic roughness.

The bottom stratification N , the topographic spectrum $P_*(k)$, the bottom velocity U , and Coriolis frequency f at each point will be used for the calculations.

2.3 The bottom stratification

We use the WOCE hydrographic atlas (Gouretski and Koltermann, 2004) to calculate the global bottom stratification. The WOCE Global Hydrographic Climatology has a 0.5° spatial resolution and 45 depth levels. The potential pressure, potential temperature and potential salinity from the bottom two layers have been used to calculate the bottom stratification using seawater_ver3_3 sw_bfrq.m. From the Fig. 2.1, we can see that the values of N are between $10^{-3.5} \text{ s}^{-1}$ and $10^{-2.5} \text{ s}^{-1}$ over most of areas. There are high values of N in mid-ocean ridge and low values of N over abyssal ocean. We don't calculate the values in the areas with a depth shallower than 500 meters.

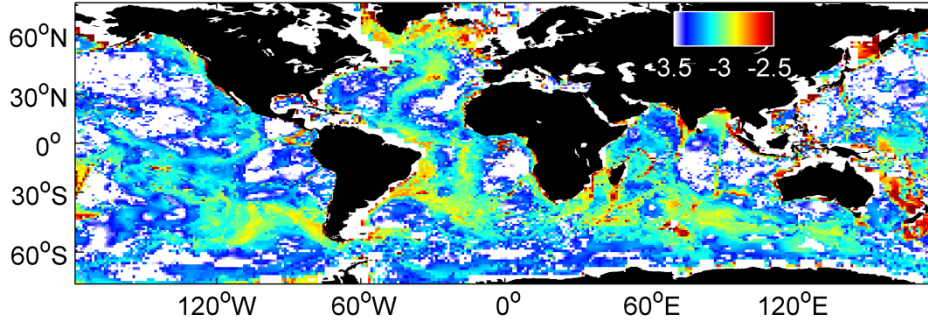


Figure 2.1. Bottom stratification N using WOCE hydrographic atlas in $\log_{10} (s^{-1})$.

2.4 The bottom topography

2.4.1 The single beam sounding depth data,

Following the method of Goff and Jordan (1998) and Nikurashin and Ferrari (2011) and assuming the topography is isotropic, the effective topographic spectrum in (2.1) then can be calculated by

$$P_*(k) = P_{1d}(k) \frac{B\left[\frac{1}{2}, \frac{\mu-1}{2}\right]}{B\left[\frac{1}{2}, \frac{\mu}{2}\right]}, \quad (2.2)$$

$$P_{1d}(k) \cong P_0 k^{-\mu+1}. \quad (2.3)$$

Where B is Beta function, $P_{1d}(k)$ is one-dimensional of model spectrum, P_0 is the spectral level given in terms of parameters of the two-dimensional spectrum and μ is the spectral slope.

NGDC's Marine Trackline Geophysics database provides access to bathymetry data collected during marine cruises from 1939 to the present. Coverage is worldwide. The resolution of the data in the Southern ocean is smaller than in the Northern Ocean.

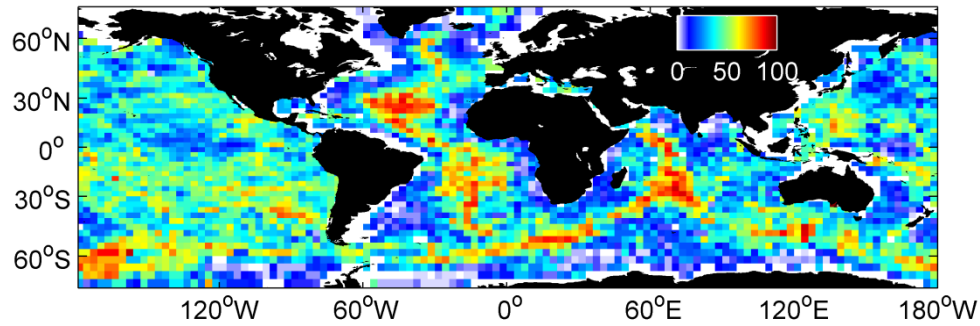
We divide the single beam sounding depth data deeper than 500 meters into different segments with a resolution of at least 2 km and a length of 50 km, remove the topographic slope for each segment, then calculate along track topographic spectrum. Using the spectrum (2.3), you can get P_0 and μ in the 2 to 20 km wavelength range.

There are two different processes to get P_0 and μ . One is averaging the spectra

over a $3^\circ \times 3^\circ$ grid first, then we can get P_0 and μ in each grid. Thus the resolution of P_0 and μ is $3^\circ \times 3^\circ$. Absent values due to lack of topographic data are estimated from neighboring grid cells. Another method is that, instead of averaging the spectra, we obtain P_0 and μ in each segment first; then we divide P_0 and μ into $3^\circ \times 3^\circ$ grid cells. Using the bottom velocity and P_0 and μ from a $3^\circ \times 3^\circ$ grid cell, we can calculate the conversion rates. Moreover, by using this method, we can get the mean conversion rate by averaging the results over the same grid in the final step, and we can also obtain the largest and smallest global conversion rates. The total number of about 225,000 segments is used. In this paper, we have calculated the conversion rate using the two methods for all velocity data.

The topographic roughness is computed as an integral of the model spectrum in (3) over 1 to 10 km wavelength range. The topographic roughness is calculated using two methods corresponding to the two ways of obtaining P_0 and μ . The large roughness (Fig. 2.2a, average spectra first) is along mid-ocean ridges where the process of seafloor spreading occurs, and it is enhanced up to 100 m. The small roughness is in flat abyssal plains which are covered by sediments. The result of second method (Fig. 2.2b, average the final results) shows a pattern similar to the Fig. 2.2a, though the roughness is a little smaller. It is up to 80 m along mid-ocean. It is remarkable, because there is a nonlinear process between the two methods for the calculation of topographic roughness. Most of areas of the ocean are covered with the topographic roughness of 0-100 m using the two methods.

a)



b)

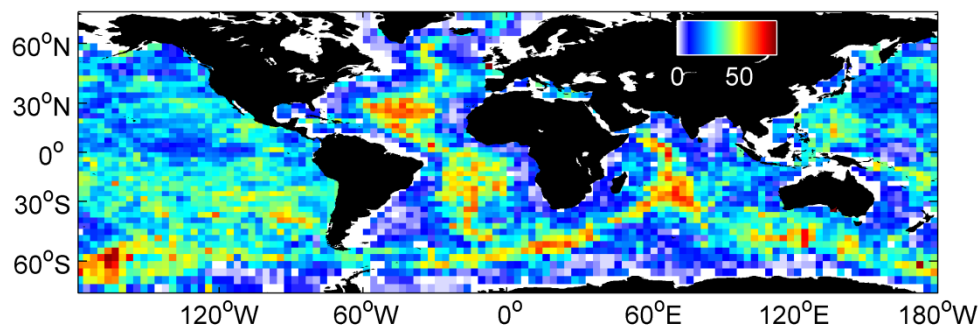


Figure 2.2. a) The topographic roughness calculated by averaging spectra first in (m).
 b) The topographic roughness calculated by averaging the final results in (m).

2.4.2 Global predicted abyssal hill rms heights

Following Goff and Arbic (2010), the global abyssal hill rms heights are calculated using paleo-spreading rate and sediment thickness by the following formula,

$$h_0 = -r \times 1473.4 y + 247 \text{ m.} \quad (2.4)$$

$$h_{\text{rms}} = h_0 - S/2, \text{ for } S/2 < h_0,$$

$$h_{\text{rms}} = 0, \text{ for } S/2 \geq h_0. \quad (2.5)$$

Where r is spreading rate, h_0 is uncorrected rms height and S is the sediment thickness. Spreading rates are downloaded from <http://www.earthbyte.org/Resources/agegrid2008.html> and sediment thickness S is provided at <http://www.ngdc.noaa.gov/mgg/sedthick> (Eden and Olbers, 2014). The rms data has 1° spatial resolution. Only part of areas of ocean has $h_{\text{rms}} > 0$ using this method.

The roughness of Goff and Arbic (2010) is shown in Fig. 2.3. Compared with the roughness calculated from the single beam sounding data, it has a much larger value along mid-ocean and can be enhanced to more than 200 meters. It hints that we will get a smaller conversion rate, if we use this roughness to replace the roughness calculated from the single beam sounding data in the calculation.

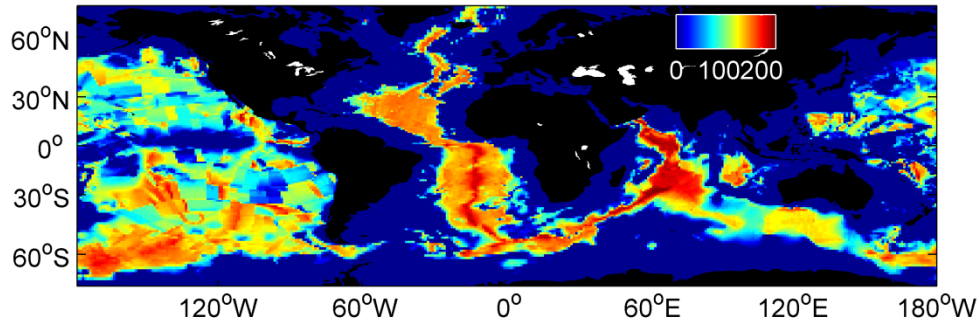


Figure 2.3. The topographic roughness of Goff and Arbic (2010) in (m).

2.5 The bottom velocity

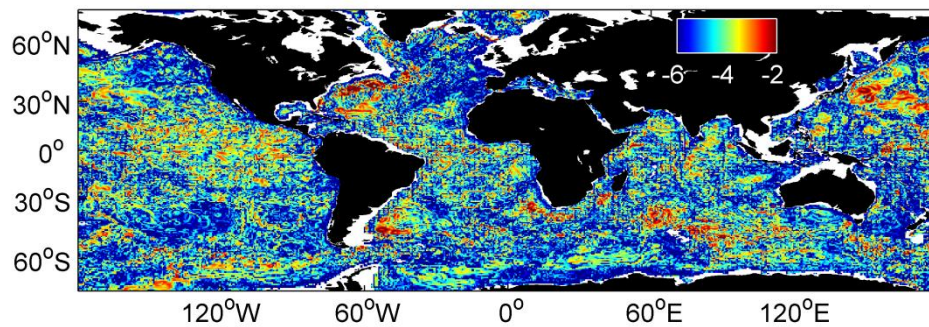
2.5.1 The bottom velocity from SODA and ECCO2

Velocity data from SODA and ECCO2 are used for the calculation. The SODA (Ocean data assimilation model) (Carton et al., 2005) is based on Parallel Ocean Program physics and there are several versions depending on the experiment setup. The data has a uniform $0.5^\circ \times 0.5^\circ$ resolution.

ECCO2 data syntheses (Menemenlis et al., 2008) are obtained by least squares fit of a global full-depth-ocean and sea-ice configuration of the Massachusetts Institute of Technology general circulation model (MITgcm) to the available satellite and in-situ data. It has a resolution of $0.25^\circ \times 0.25^\circ$. The outputs of the two data are all in a monthly-averaged form.

In Fig. 2.4, we calculate the bottom kinetic energy of SODA and ECCO2 using the velocity from the deepest layer. The bottom kinetic energy is calculated by $KE = u^2 + v^2$, where u and v are the bottom velocities. The results show that the bottom kinetic energy is larger in western boundary currents regions, ACC region and the Equator region, compared with the energy in abyssal plains.

a)



b)

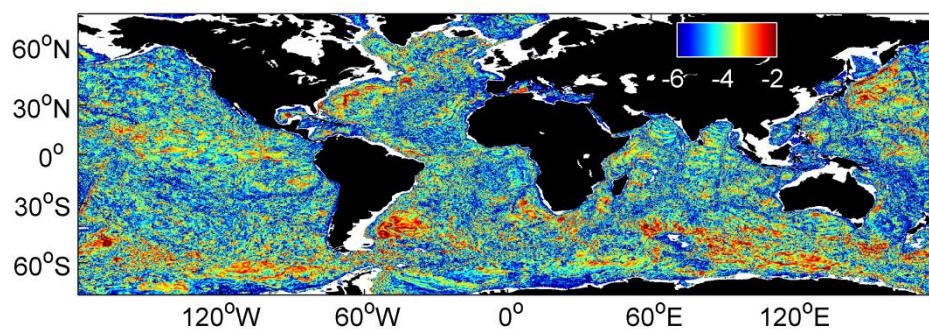


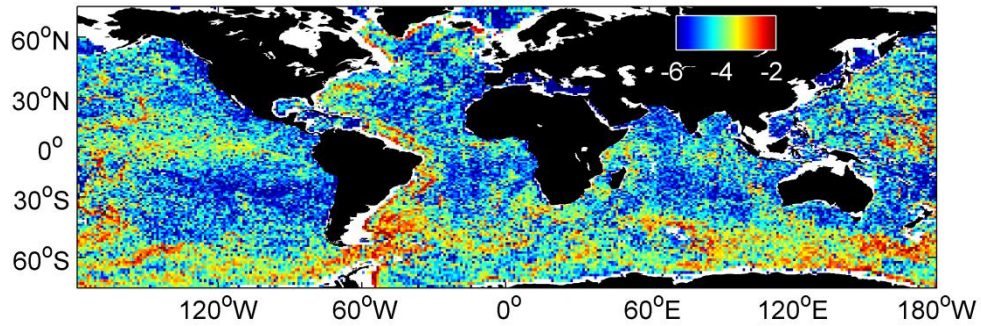
Figure 2.4. Bottom kinetic energy of SODA (a) and ECCO2 (b) in $\log_{10}(\text{m}^2 \text{s}^{-2})$.

2.5.2 The mean flow and eddy velocity from the global eddy-permitting STORM model

The mean flow and eddy velocity are got from the global eddy-permitting STORM model (Storch et al., 2012). The model was spun up for 25 years. Then the model was run with the forcing of 6 hourly NCEP-NCAR reanalysis-1 (Kalnay et al., 1996) for the period 1948-2010 with a resolution of about one tenth of degree, so it can achieve a quasi-steady state of mesoscale eddies. Here we use the output of mean flow and eddy velocity, both of which have a resolution of $1^\circ \times 1^\circ$.

The MKE (mean flow kinetic energy) and EKE (eddy kinetic energy) are shown in Fig. 2.5. The EKE is larger than the MKE in most areas of the ocean and the energy can be enhanced to $10^{-2} \text{m}^2 \text{s}^{-2}$ in ACC region.

a)



b)

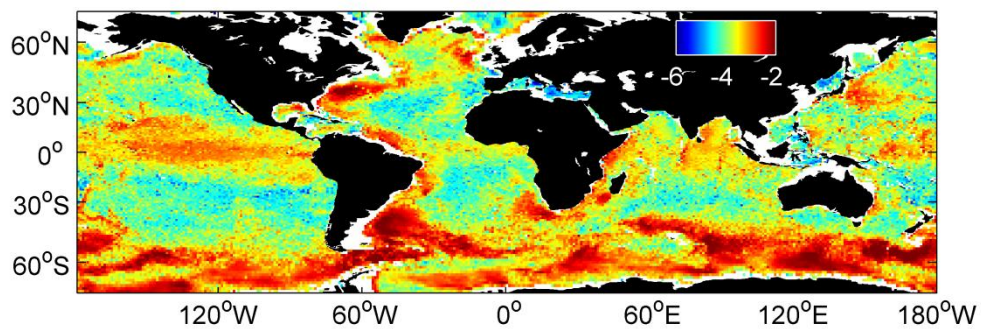


Figure 2.5. Bottom MKE (a) and bottom EKE (b) in $\log_{10}(\text{m}^2 \text{s}^{-2})$.

2.6 Results

2.6.1 Steepness parameter

The steepness parameter is determined by the buoyancy frequency, the topographic height and the bottom velocity. The steepness parameter calculated using the eddy velocity from the global eddy-permitting STORM model is shown here. The steepness parameter (Fig. 2.6) is large in the areas with large topographic height and small velocity, such as the equatorial regions and the mid-ocean ridges. It is small in the ACC area because of large velocity. The steepness parameters of SODA, ECCO2 and mean flow for different topographic roughness are also calculated, but not shown here.

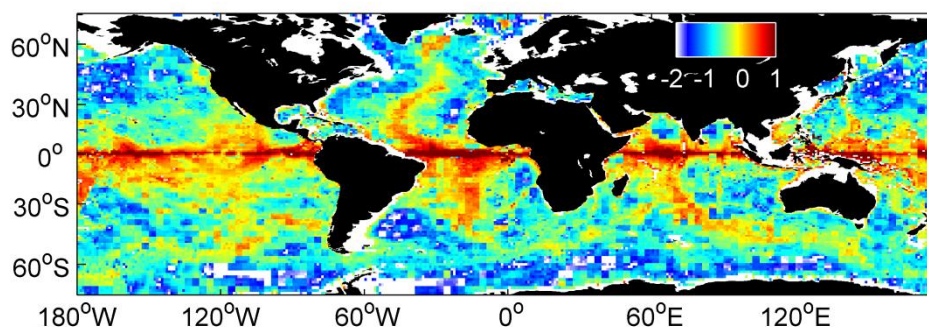


Figure 2.6. The topographic steepness parameter ϵ calculated using eddy velocity in $\log_{10}()$.

2.6.2 Conversion rate

The conversion rates calculated using SODA, ECCO2, mean flow and eddies by the two methods (Average spectra first and average the final results), which are described in 2.4.1, are shown in Fig. 2.7-2.10. The steepness calculated using the rms height in the radiative wavenumber range is used for the calculations. The conversion rate is enhanced in the large currents areas and shows a pattern similar to the bottom kinetic energy. The results calculated by the two methods for the same velocity data are different, but similar. The global integral of the energy conversion rates of SODA are 0.04 TW (Fig. 2.7a, average spectra first) and 0.03 TW (Fig. 2.7b, average the final results) and the results of ECCO2 (Fig. 2.8a-b) are 0.05 TW and 0.04 TW, respectively. Here we set the conversion rates in the areas with values larger than $2 \times 10^2 \text{ mW m}^{-2}$ to be 0 in order to inhibit large value. The global integral of the energy conversion rate calculated using mean flow (Fig. 2.9a-b) is 0.06 TW by averaging spectra first, and the value becomes 0.04 TW, if we average the results in the final step. The conversion rates calculated using eddy velocity (Fig. 2.10a-b) are 0.11 and 0.09 TW, respectively, using the two methods. The velocities from SODA, ECCO2 and mean flow used in the paper are obviously smaller than the velocities used in Nikurashin and Ferrari (2011) and Scott et al. (2011), thus the conversion rates are much smaller.

The sensitivity of the conversion rates to the steepness is investigated. As described in section 2.2, the steepness here is defined in two ways and we have three different topographic roughnesses for the second way. All results are shown in Table

2.1, where `Roughness_range` means the rms height in the radiative wavenumber range, `Roughness_first` means the roughness that is calculated by averaging spectra first, `Roughness_last` means the roughness that is calculated by averaging the final results and `Roughness_Goff_and_Arbic` means the rms height (Goff and Arbic, 2010). The results obtained using `Roughness_range` have been shown in the above paragraph. The `Roughness_last` is smaller than the `Roughness_first`, thus the conversion rate using `Roughness_last` is a little larger than the result using `Roughness_first`. It is found the conversion rates for the four velocities using `Roughness_first` are between 0.08 and 0.19 TW and using `Roughness_last` between 0.10 and 0.23 TW. The conversion rates of eddies are the largest because the amplitude of eddies are largest.

The roughness (Goff and Arbic, 2010) has a larger value along mid-ocean compared with the results using the single beam sounding data, and covers less non-zero areas (Fig. 2.3). So if we use topographic roughness of Goff and Arbic (2010), there will be large areas with zero value and the total conversion rate will be smaller than the actual value. The conversion rates calculated using SODA, ECCO2, mean flow and eddies are 0.04, 0.03, 0.05 and 0.08 TW, respectively. The conversion rate calculated using roughness of Goff and Arbic (2010) is just a reference for the actual value.

The results in Table 2.2 are obtained using the second method and using `Roughness_range`. In Table 2.2, Mean means that we average the conversion rates in the final step; Largest means we choose the largest conversion rate for each grid and Smallest means we choose the smallest conversion rate for each grid. Moreover, the results for Largest and Smallest are unreal in nature and just used to test the sensitivity to the topographic spectrum. The results for Mean have been discussed in the above. The physical meaning for the results for Largest and Smallest is that these two values represent the upper and lower global integral conversion rates for one velocity data using the linear theory. For example, the mean conversion rate for SODA is 0.03 TW, but the upper and lower conversion rates are 0.19 and 0.002 TW, respectively, which are almost 10 times larger and 10 times smaller than the mean conversion rate. As we know, if we calculated the conversion rate only using one topographic spectrum, the result won't be so accurate. The results from Table 2.2 show that the difference caused only using one topographic spectrum may have two orders of magnitude for the global ocean, since the upper conversion rate is almost

100 times larger than the lower conversion rate. Furthermore, the result only using one topographic spectrum may be 10 times larger or 10 times smaller than the mean value.

From Table 2.1 and Table 2.2, we can see that the global integral of the conversion rate calculated using mean flow is between 0.04 and 0.12 TW using the two methods. In contrast, the conversion rate calculated using eddy velocity is between 0.09 and 0.23 TW using the two methods. The difference between the conversion rate from the eddies and from the mean flow is about 0.05-0.11 TW. Compared with the results from SODA and ECCO2, the conversion rate calculated using the global eddy-permitting STORM model is larger, indicating that the velocity data is crucial for the calculation.

Table 2.1. The conversion rate calculated by the first method. (TW)

	Roughness _range	Roughness _first	Roughness _last	Roughness_Goff _and_Arbic
SODA	0.04	0.09	0.10	0.04
ECCO2	0.05	0.08	0.10	0.03
Mean flow	0.06	0.11	0.12	0.05
Eddies	0.11	0.19	0.23	0.08

Table 2.2. The conversion rate calculated by the second method. (TW)

	Mean	Largest	Smallest
SODA	0.03	0.19	0.002
ECCO2	0.04	0.22	0.003
Mean flow	0.04	0.23	0.002
Eddies	0.09	0.54	0.007

2.7 Summary

Different velocity and topography datasets are used to calculate the conversion rate. About 0.03-0.23 TW energy is transferred from geostrophic flows to internal lee waves field using the single beam sounding data. The value will be 0.03-0.08 TW using the roughness of Goff and Arbic (2010). We choose the values calculated using

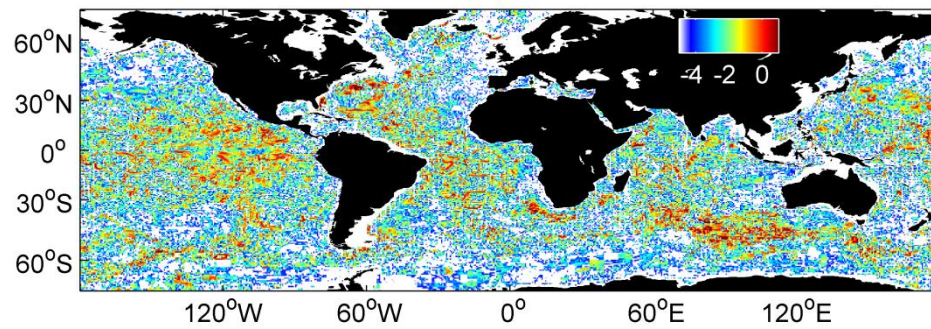
single beam sounding data as the last results, but the values are still smaller than the results (Scott et al., 2011), because the velocities used here are smaller. In addition, we don't try to answer which result is better compared with Nukurashin and Ferrari (2011), because we can't get enough observation data so far. Better topography data is needed for a better estimation. Compared with 1 TW of power lost from barotropic tides in the deep ocean (Egbert and Ray, 2001), the energy transferred from geostrophic flow is a little smaller.

We differentiate between the conversion rate from eddies and from the mean flow. The conversion rate for eddies is almost twice as the conversion rate for the mean flow. The results here stress the importance of eddies. By the second method, we have obtained the error bound of the conversion rate. The results indicate that the topographic spectrum causes large uncertainties in the conversion rate.

The breaking and dissipation of internal lee waves contribute to the diapycnal mixing. However, the scale of the processes is too small for ocean circulation models to resolve; hence we need to parameterize the subgrid motions. Melet et al. (2014) set up a series of experiments using the Geophysical Fluid Dynamics Laboratory CM2G ocean-ice-atmosphere coupled model including a parameterization of lee wave-driven mixing and showed that the lee waves generated by geostrophic flows had a significant impact on the ocean state. The effects should be further verified because the exact conversion rate of lee waves is still a wide open question, and the vertical structure and process of dissipation of lee waves are still not clear.

2 The conversion rate of internal lee waves generation by global geostrophic flows

a)



b)

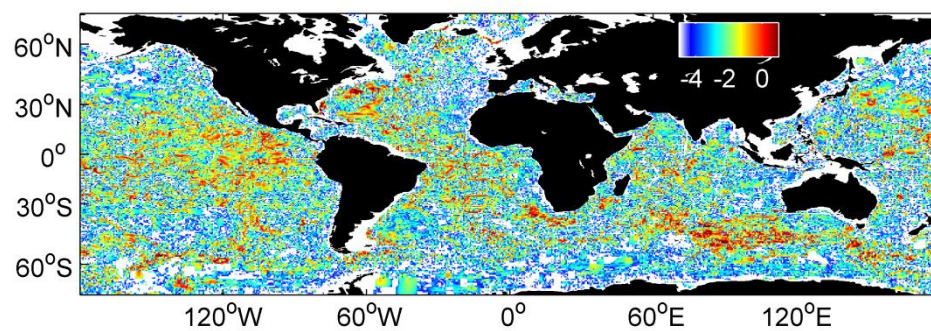
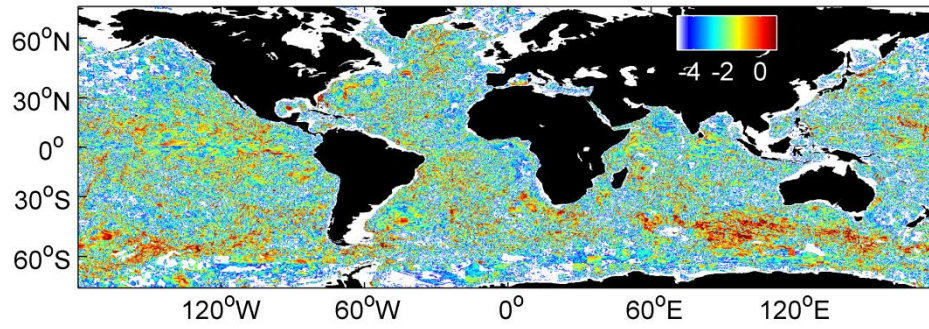


Figure 2.7. The internal lee waves generation rate of SODA. a) Average spectra first in $\log_{10} (\text{mW m}^{-2})$. b) Average the final results in $\log_{10} (\text{mW m}^{-2})$.

a)



b)

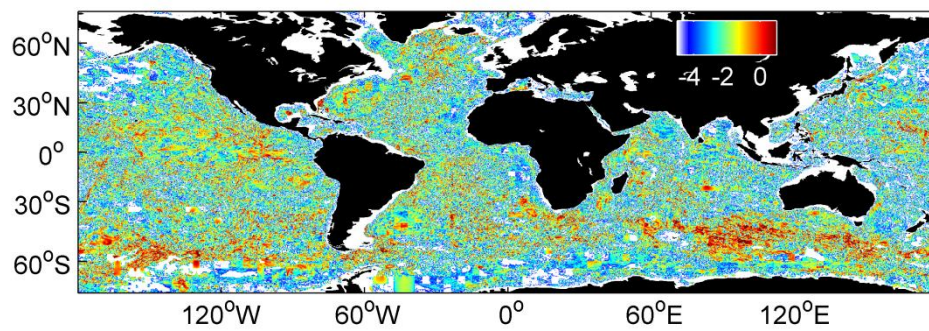
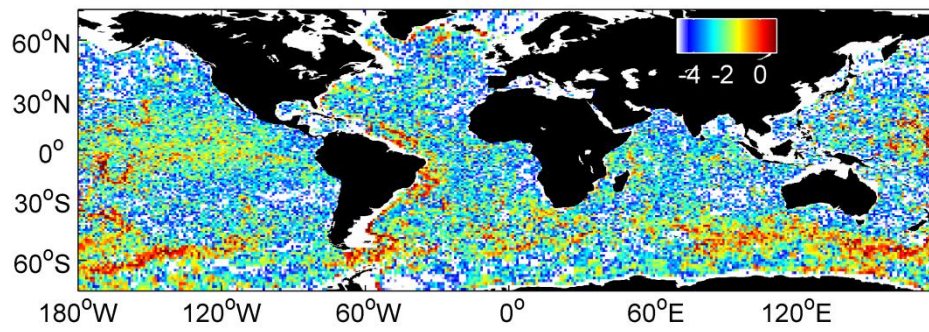


Figure 2.8. The internal lee waves generation rate of ECCO2. a) Average spectra first in $\log_{10} (\text{mW m}^{-2})$. b) Average the final results in $\log_{10} (\text{mW m}^{-2})$.

2 The conversion rate of internal lee waves generation by global geostrophic flows

a)



b)

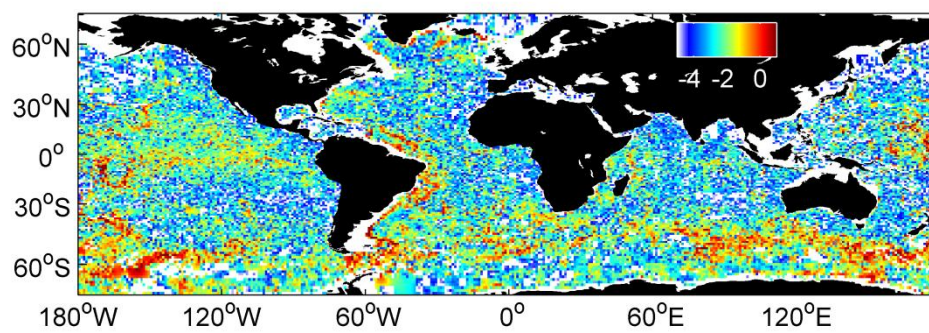
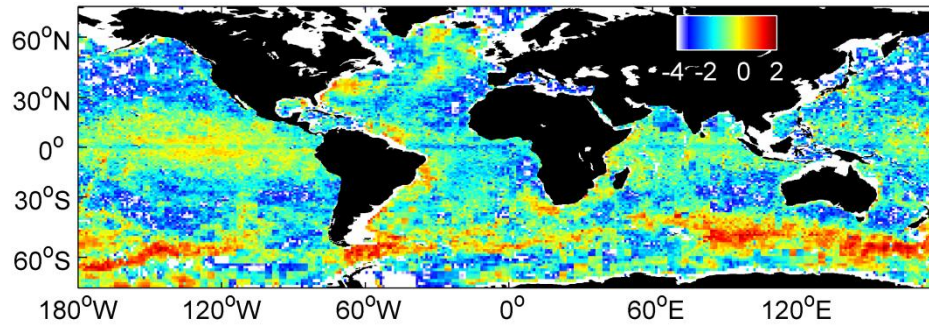


Figure 2.9. The internal lee waves generation rate of mean flow. a) Average spectra first in $\log_{10} (\text{mW m}^{-2})$. b) Average the final results in $\log_{10} (\text{mW m}^{-2})$.

a)



b)

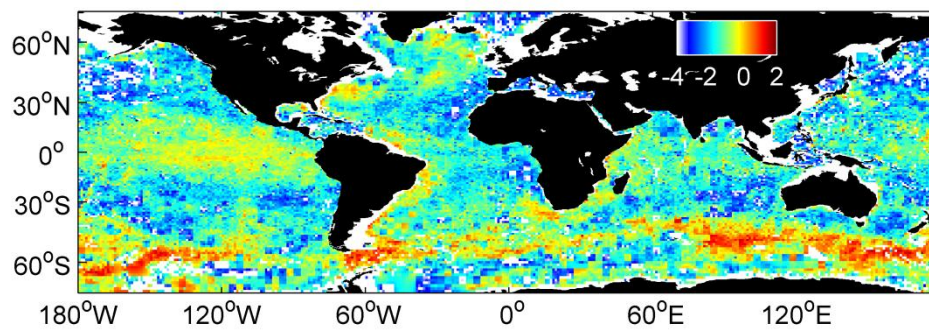


Figure 2.10. The internal lee waves generation rate of eddy velocity. a) Average spectra first in $\log_{10} (\text{mW m}^{-2})$. b) Average the final results in $\log_{10} (\text{mW m}^{-2})$.

Chapter 3

3 Tidal flow over sinusoidal topography: the harmonics, energy flux and conversion rate

Abstract

In this paper, a series of two-dimensional numerical simulations using MITgcm are set up to investigate the baroclinic tide generated by barotropic tide over sinusoidal topography. In terms of the linear tide theory, the baroclinic tide generated due to tide-topography interaction is mainly influenced by the barotropic forcing, the stratification and the topography. Here, the influences of the height of the topography, the amplitude of the barotropic tide, the stratification and the width of the topography on the baroclinic tide generation are investigated in detail. Moreover, we compare the results predicted by the linear theory with the results calculated using two definitions of conversion rate. Model results show that the baroclinic velocity fields generated are quite different between in subcritical cases and in supercritical cases; there are more high harmonics generated in the case with three-sinusoidal topography compared with results from the case with an isolated sinusoidal topography by two methods of calculating the modes of the baroclinic velocities. The results predicted by the linear theory agree well with the results calculated by C1 (the energy flux) in most cases and the results calculated by C2 (the conversion rate) are larger than the results calculated by C1 in most cases.

3.1 Introduction

The tide force is generated by the combination of the gravitational attraction between the astronomical objects (Moon and Sun) and the Earth, and the rotation of Earth-astronomical objects systems. The energy from the barotropic tides will be either converted to the baroclinic tides or dissipated in oceanic regions. The internal tides are generated when barotropic tides flow over bottom topography in stratified ocean. After the internal tide generation, low mode internal tides tend to propagate away from the generation sites and high mode internal tides tend to dissipate locally

because of their low speeds and high shear. The internal tide energy can be transferred into small scale through wave breaking, wave-wave interaction, bottom friction, scattering from bottom topography and reflection from critical topography. When the internal tides break and dissipate, the background mixing will be enhanced. The diapycnal mixing generated due to these processes can contribute in sustaining the MOC and should be parameterized in ocean models. To get a better parameterization, we need to study the internal tide generation, propagation and dissipation processes. In the paper, we mainly focus the generation process.

The internal tide generation has been studied in theory. Bell (1975a) derived the conversion rate in an ocean of infinite depth based on weak topography approximation. Balmforth et al. (2002) derived the conversion rate for several topographies, and the conversion rate of subcritical sinusoidal topography was about 56% larger than the Bell's theory (Bell, 1975a). It was extended to the supercritical topography cases in Balmforth and Peacock (2009). In general, these studies (Bell, 1975a, b; Balmforth et al., 2002; Llewellyn Smith and Young, 2002; Khatiwala, 2003; Párdís et al., 2006; Balmforth and Peacock, 2009) have used different mathematical methods to derive the conversion rate and extended the linear theory to cases with different topographies based on different assumptions. Furthermore, Nycander (2005) calculated the conversion rate basing on the theory (Bell, 1975a, b; Llewellyn Smith and Young, 2002) and got that the conversion rate from barotropic tides into internal waves was about 1.2 TW at depths greater than 500 m.

Legg and Huijts (2006) set up experiments to simulate the baroclinic tide generated by barotropic tide over Gaussian topography. Their results showed that the conversion rate predicted by Bell (1975b) was good for 'low wide' Gaussian topography, but the conversion rates calculated from other cases were much larger than the values predicted by the linear theory (Bell, 1975b). Di Lorenzo et al. (2006) used the ROMS to simulate the barotropic tide over polynomial ridge topography, and compared the model results with the values calculated by $C = \frac{\pi\rho_0 U_0^2 h_{\max}^2 N}{4\omega_0} \sqrt{(\omega_0^2 - f_0^2)} \times M$, where ρ_0 is the reference density, U_0 is the amplitude of the barotropic tide, h_{\max} is the height of the ridge, N is the buoyancy frequency, ω_0 is the M2 tidal frequency, f_0 is the Coriolis frequency and M is a dimensionless function that depends on many factors (Petrelis et al., 2006). Results showed that the model results agreed well with the theory. Note that these two works have used different definitions of conversion rate which are equal in the linear theory

with the assumption of in viscid fluid.

The height of the topography, the width of the topography, the depth of the ocean, the amplitude of the barotropic tide and the stratification have an obvious influence on the conversion rate (Legg and Huijts, 2006; Di Lorenzo et al., 2006; Qian et al., 2010; Paoletti et al., 2014). There are five main nondimensional parameters based on the above factors (Legg and Huijts, 2006): the tidal excursion parameter; the slope of the topography; the slope of the internal wave; the relative height of the topography; the Froude number. Every parameter has an influence on the generations of the internal waves.

The real ocean topography is complex and the generation of internal tides is largely influenced by the topography. Thus it is necessary to study the internal tide generation for a variety of topographies. The internal tide generated by barotropic flow over sinusoidal topography hasn't been studied in numerical simulations in detail. Here we study several features of internal tides including the baroclinic velocity, energy density and harmonics, and focus on the energy flux and conversion rate. A series of experiments with different conditions are carried out to compare the theoretic predictions (Balmforth et al., 2002) with the model results. It is aimed to give us a better understanding of the internal tide generation process.

The paper is organized as follows. In section 3.2, the model setup and all the designed cases are introduced; in section 3.3, the baroclinic velocities calculated from different cases are analyzed; in section 3.4, the kinetic energy and potential energy for different cases are shown; in section 3.5, the spectra of the velocities are shown; in section 3.6, the harmonics are presented; in section 3.7, different conversion rates predicted by the linear theory and obtained from numerical simulations are shown; at last, the discussion and conclusion parts are offered in section 3.8.

3.2 Model

The nonhydrostatic MITgcm (Marshall et al., 1997) is used to simulate the internal waves. Therefore, we can compare model results with the results predicted by the linear theory based on nonhydrostatic assumption. The length and the height of the domain are 120 km and 2 km, respectively. The horizontal resolution is uniform 1.5 km, and the vertical resolution is uniform 50 m. The standard

3 Tidal flow over sinusoidal topography: the harmonics, energy flux and conversion rate

experiment is initialized with a uniform constant stratification of $N=10^{-3} \text{ s}^{-1}$, which is represented by the temperature in the model using a linear equation of state. We set up several experiments with buoyancy frequencies of $N=10^{-2}$, $10^{-2.5}$ and $10^{-3.5}$, respectively, to investigate the sensitivity to the stratification. The Coriolis frequency $f=5 \times 10^{-5} \text{ s}^{-1}$, and it represents the value in the latitude 20°N . In order to get a small dissipation, the horizontal and vertical viscosity and diffusivity are set to be $10^{-3} \text{ m}^2 \text{ s}^{-1}$ and $10^{-5} \text{ m}^2 \text{ s}^{-1}$, respectively. The barotropic tide is forced by adding a body force to the momentum equation and the boundary conditions are the same with Khatiwala (2003), which has been also used in Legg and Huijts (2006) and Green et al. (2008).

All of the configurations of experiments are listed in Table 3.1, where U is the barotropic velocity, N is the stratification, h_0 is the maximum height of the sinusoidal topography, and width is the width of the topography. The nondimensional parameter $\gamma = (dh/dx)/s$ is also calculated, where dh/dx is the largest slope of the topography in the model, and $s = \sqrt{(\omega^2 - f^2)/(N^2 - \omega^2)}$ is the slope of internal wave beam, where ω is the M2 tide frequency. Following a widely-used convention, we define that when $\gamma < 1$, the case is subcritical; when $\gamma > 1$, the case is supercritical; when $\gamma = 1$, the case is critical. We can see in Table 3.1 that Exp_h1600 and Exp_width18 are critical cases, Exp_N2.5 and Exp_N02 are supercritical cases and all other experiments are subcritical cases. Another nondimensional parameter $Fr = U/(h_0 \times N)$ is also offered in the table. The Fr of all our experiments is smaller than 1. A series of experiments are performed to study the energy flux and conversion rate influenced by the height of the topography, the width of the topography, the amplitude of the barotropic tide and the stratification. For example, the heights of the topography from Exp_h200, Exp_h400, Exp_Ref and Exp_h1600 vary from 200 to 1600 m and cause the cases to be from subcritical to supercritical. All experiments are run for 20 M2 tidal cycles.

Table 3.1. List of cases: the values in all blank cells are the same to the Exp_Ref in the same column.

Case	U (m s^{-1})	h_0 (m)	N (s^{-1})	Width (km)	Fr	$\frac{dh}{dx}$	s	
Exp_Ref	0.025	800	10^{-3}	30	0.0313	0.0824	0.1327	Sub
Exp_h200		200			0.1250	0.0206		

Exp_h400	400		0.0625	0.0412	
Exp_h1600	1600		0.0156	0.1667	Critical
Exp_u0.05	0.05		0.0625		
Exp_u0.10	0.10		0.1250		
Exp_u0.20	0.20		0.2500		
Exp_N02		10^{-2}	0.0031	0.0131	Sup
Exp_N2.5		$10^{-2.5}$	0.0099	0.0416	Sup
Exp_N3.5		$10^{-3.5}$	0.0988	0.4636	
Exp_width18		18	0.0313	0.1333	Critical
Exp_width54		54	0.0313	0.0463	

3.3 The baroclinic velocity

The baroclinic velocity is got from the following formula,

$$u'(x, z, t) = u(x, z, t) - \frac{1}{\eta+h} \int_{-h}^{\eta} u(x, z, t) dz, \quad (3.1)$$

where u is the full velocity, η is the free surface elevation and h is the depth of ocean. The same calculation is also applied on v and w . Fig. 3.1 shows the snapshots of baroclinic velocities calculated from the four experiments with the same barotropic tide of 0.025 m s^{-1} and different heights of the topography at the end of the seventh tidal cycle. The baroclinic beams can be seen from the Fig. 3.1, indicating the generated baroclinic tide is mainly linear. According to the linear theory, the slope of the baroclinic beam $s = \sqrt{(\omega^2 - f^2)/(N^2 - \omega^2)}$, where ω is the tidal frequency, f is the Coriolis frequency and N is the stratification. Since the stratification used in the four experiments is the same, the patterns of the four velocity fields are similar. However, they differ in the amplitudes of the baroclinic tides: when the height of the topography $h=200 \text{ m}$, the amplitude of the generated baroclinic tide can reach 0.005 m s^{-1} , in contrast, the baroclinic velocities can reach 0.012 , 0.04 and 0.15 m s^{-1} , when the heights of the topography are 400 , 800 and 1600 m , respectively. In summary, as the height of the topography increases, the amplitude of the baroclinic tide increases.

The snapshots of the baroclinic velocity for Exp_u0.05 and Exp_u0.20 are shown in Fig. 3.2. As illustrated in Fig. 3.2, the patterns of the baroclinic velocity

3 Tidal flow over sinusoidal topography: the harmonics, energy flux and conversion rate

fields are similar for the two cases. However, the amplitude of the baroclinic tide is larger and the baroclinic velocity becomes more unstable near the boundary of the topography, when the amplitude of the barotropic tide increases.

The sensitivity of the baroclinic tide to the stratification is investigated in the cases with different buoyancy frequencies. Fig. 3.3(a) shows the baroclinic velocity field for the subcritical case Exp_N3.5. We can see that the baroclinic velocity is very weak, when there is weak stratification. For Exp_N02, the buoyancy frequency $N=10^{-2} \text{ s}^{-1}$ and $\gamma = (dh/dx)/s > 1$, hence the case is supercritical. As shown in Fig. 3.3(b), higher harmonics are generated with strong stratification and the pattern changes a lot due to the changing of the stratification, compared with the subcritical case.

The cases Exp_Ref, Exp_width18 and Exp_width54 have the same stratification and barotropic tide, and only differ with widths of the topography. The baroclinic velocity fields for Exp_width18 and Exp_width54 are shown in Fig. 3.4. The amplitude of the baroclinic tide generated in Exp_width18 is much larger than that in Exp_width54. Though the stratification in Exp_width18 and Exp_width54 is the same, the patterns of the baroclinic velocity fields in these experiments are different. One reason is that the width of the topography in Fig. 3.4(b) is larger than the length of mode 1 internal tide and the width of the topography in Fig. 3.4(a) is smaller than the length of mode 1 internal tide.

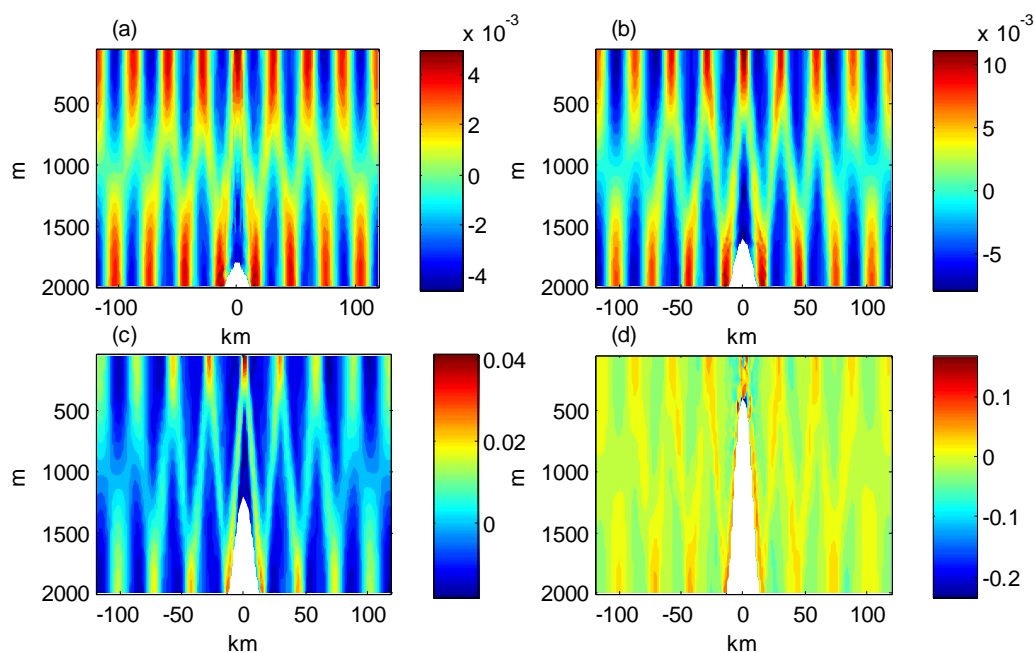


Figure 3.1. Snapshots of baroclinic velocity (m s^{-1}) after 7 tidal cycles, the height of the topography (a) $h=200$ m, (b) $h=400$ m, (c) $h=800$ m, and (d) $h=1600$ m.

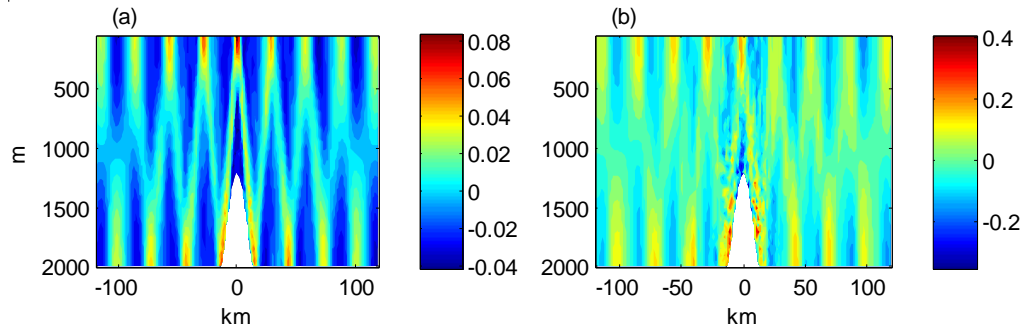


Figure 3.2. Snapshots of baroclinic velocity (m s^{-1}) after 7 tidal cycles, (a) $u=0.05$ m s^{-1} , and (b) $h=0.20$ m s^{-1} .

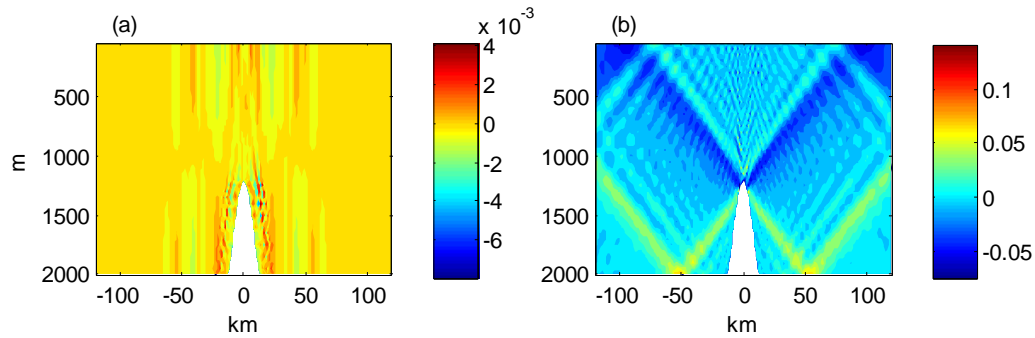


Figure 3.3. Snapshots of baroclinic velocity (m s^{-1}) after 7 tidal cycles, the stratification (a) $N=10^{-3.5}$ s^{-1} , and (b) $N=10^{-2}$ s^{-1} .

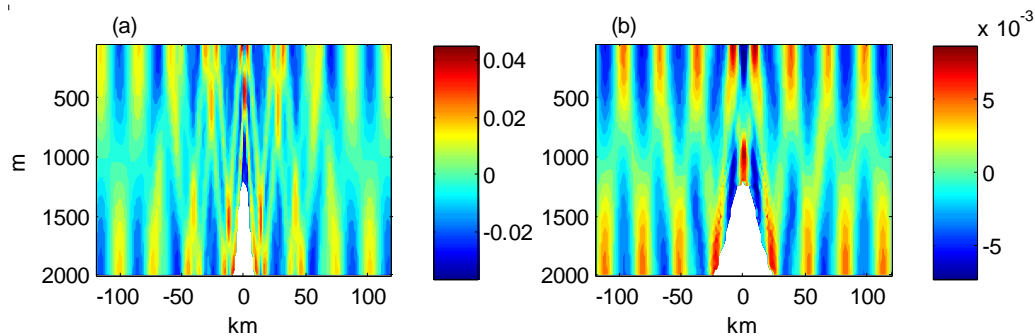


Figure 3.4. Snapshots of baroclinic velocity (m s^{-1}) after 7 tidal cycles, the width of the topography (a) width=18 km, and (b) width=54 km.

3.4 The kinetic energy and potential energy

Here we want to show the energy density of the internal tides. In the chapter, the

kinetic energy is defined by $KE = \frac{1}{2}\rho_0(u'^2 + v'^2 + w'^2)$, and the available potential energy APE is defined by $APE = \frac{g^2 \rho'^2}{2\rho_0 N^2}$, where ρ' is the perturbation density and ρ_0 is the constant reference density. The discussion of different definitions of APE in detail can be found in Kang and Fringer (2010).

The Fig. 3.5, Fig. 3.6 and Fig. 3.7 show the snapshots of APE, KE, and APE plus KE for Exp_Ref, Exp_width18 and Exp_N2.5, respectively. From Fig. 3.5a), we can see that most of available potential energy is in the interior of the ocean. The largest available potential energy distributes in the vicinity of the topography and can reach 0.25 J m^{-3} . In contrast, the kinetic energy scatters in the upper and lower boundary and the largest kinetic energy distributes in the upper of the topography, as shown in Fig. 3.5b). The energy density is calculated by summing the available potential energy and the kinetic energy. As illustrated in Fig. 3.5c), each vertical beam represents the energy density radiated away within one tidal cycle.

The patterns of APE, KE, and APE plus KE for Exp_width18 shown in Fig. 3.6a) are similar to the results for Exp_Ref. But the values for Exp_width18 are larger than those for Exp_Ref. The APE, KE, and APE plus KE for supercritical case Exp_N2.5 are shown in Fig. 3.7. The pattern of APE is quite different with the patterns for subcritical cases. The energy beams originate from the bottom topography and reflect when the beams meet the surface. The patterns of KE, and APE plus KE are quite similar to the pattern of APE. In addition, we can see higher harmonic frequencies are generated in the upper of the bottom topography.

Not only the snapshots of the APE, KE, and APE plus KE but also the time-averaged APE, KE, and APE plus KE are calculated. The results for the three cases are averaged over 3 tidal cycles from the beginning of the seventh tidal cycle and shown in Fig. 3.8, Fig. 3.9 and Fig. 3.10, respectively. In Fig. 3.8a) we can see that the available energy mainly distributes in the interior and shows a wave-like structure. In contrast, the kinetic energy distributes in the upper and bottom domain as shown in Fig. 3.8b). The time-averaged energy density are shown in Fig. 3.8c), we can find that the energy distributes over the whole domain. The APE, KE, and APE plus KE for Exp_width18 show a pattern similar to those in Fig. 3.8. But the values for Exp_width18 are larger. Furthermore, the APE, KE, and APE plus KE for Exp_N2.5 are largest. As shown in Fig. 3.10, the patterns of APE, KE, and APE plus

KE are quite different with the former two cases. The energy density is large in the areas around the topography and become smaller when the distance is far away from the central domain.

Fig. 3.11, Fig. 3.12 and Fig. 3.13 show the temporal evolution of APE, KE, and APE plus KE for three different cases from the beginning of seventh tidal cycle. The patterns of APE, KE, and KE plus APE as shown in Fig. 3.11 are quite similar, and show a symmetric structure around the topography. The slope of the beam is determined by the buoyancy frequency when the tidal frequency and the Coriolis frequency are the same. Hence, the slopes of APE, KE, and KE plus APE for Exp_width18 are the same to the ones for Exp_Ref, as shown in Fig. 3.12. In addition, the APE, KE, and KE plus APE for Exp_N2.5 are shown in Fig. 3.13. We can see that the slopes of the energy beams are smaller than those for Exp_Ref and Exp_width18. However, the amplitudes of the available potential energy, the kinetic energy and the energy density are larger than those for the former two cases.

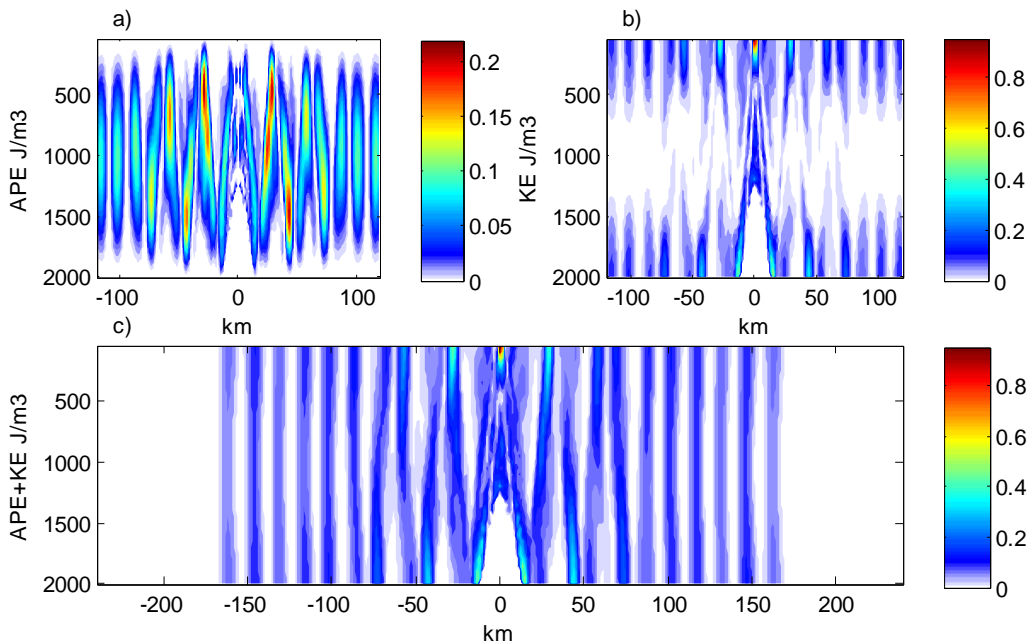


Figure 3.5. Snapshots of APE, KE, and APE plus KE for Exp_Ref after 7 tidal cycles, a) APE, b) KE, and c) APE+KE.

3 Tidal flow over sinusoidal topography: the harmonics, energy flux and conversion rate

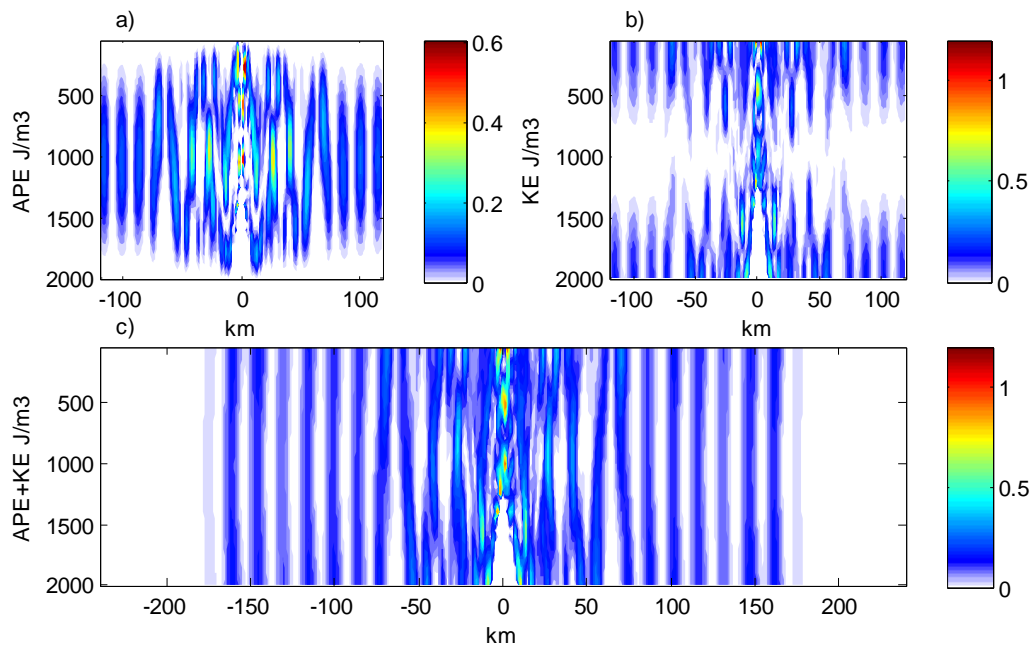


Figure 3.6. Snapshots of APE, KE, and APE plus KE for Exp_width18 after 7 tidal cycles, a) APE, b) KE, and c) APE+KE.

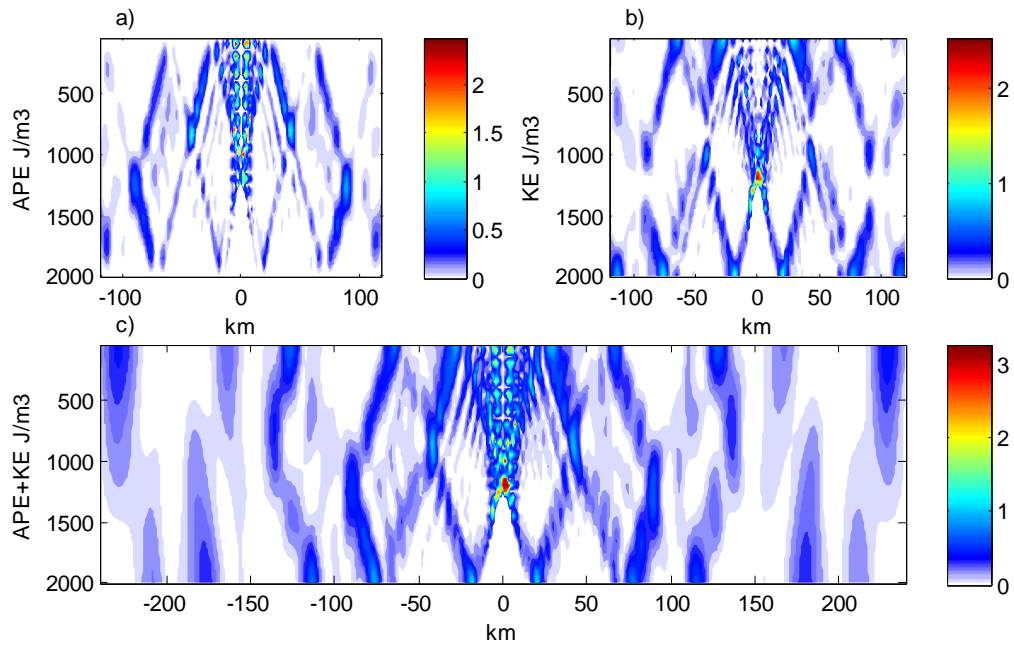


Figure 3.7. Snapshots of APE, KE, and APE plus KE for Exp_N2.5 after 7 tidal cycles, a) APE, b) KE, and c) APE+KE.

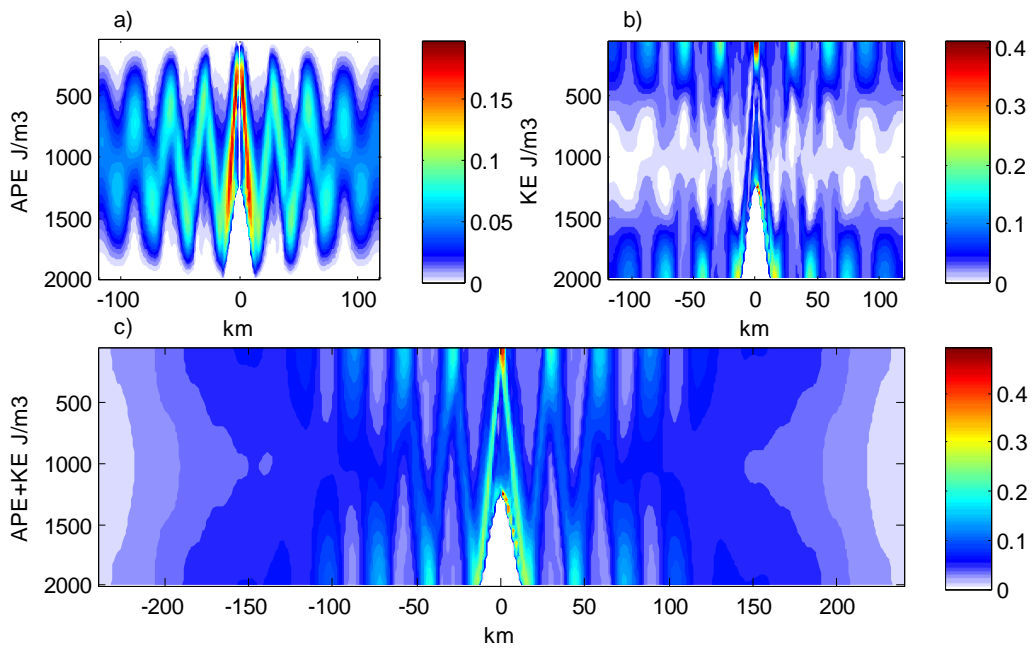


Figure 3.8. The APE, KE, and APE plus KE for Exp_Ref averaged over 4 tidal cycles, a) APE, b) KE, and c) APE+KE.

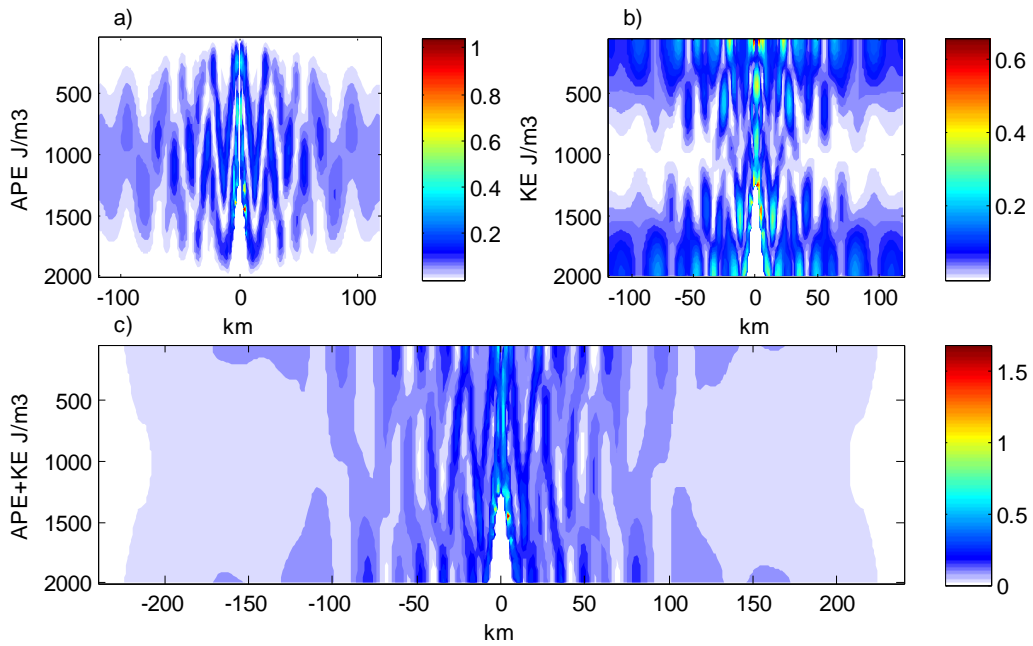


Figure 3.9. The APE, KE, and APE plus KE for Exp_width18 averaged over 4 tidal cycles, a) APE, b) KE, and c) APE+KE.

3 Tidal flow over sinusoidal topography: the harmonics, energy flux and conversion rate

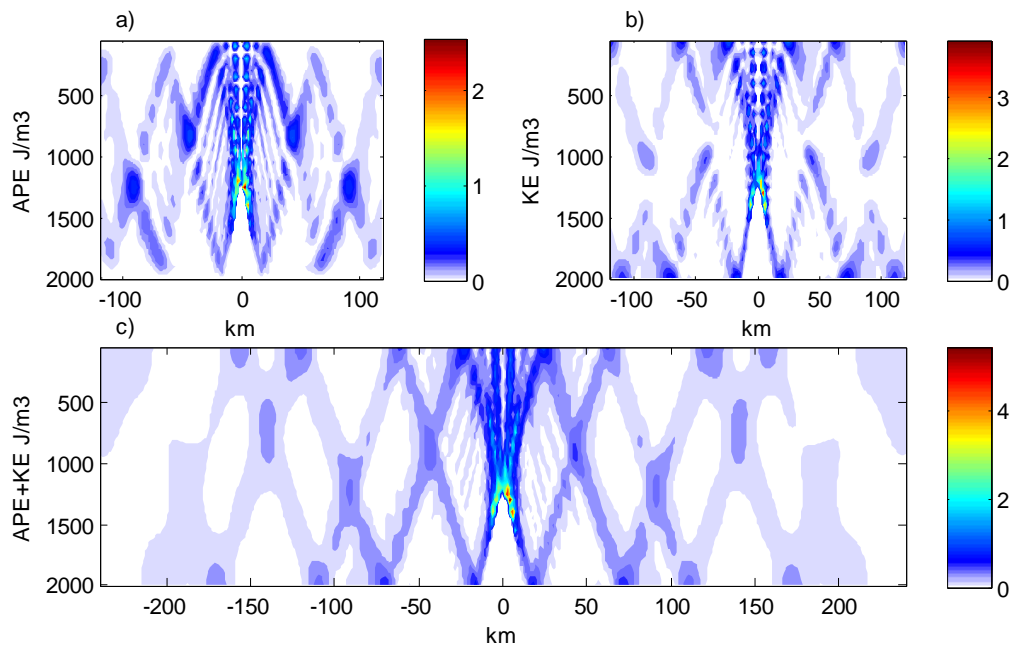


Figure 3.10. The APE, KE, and APE plus KE for Exp_width18 averaged over 4 tidal cycles, a) APE, b) KE, and c) APE+KE.

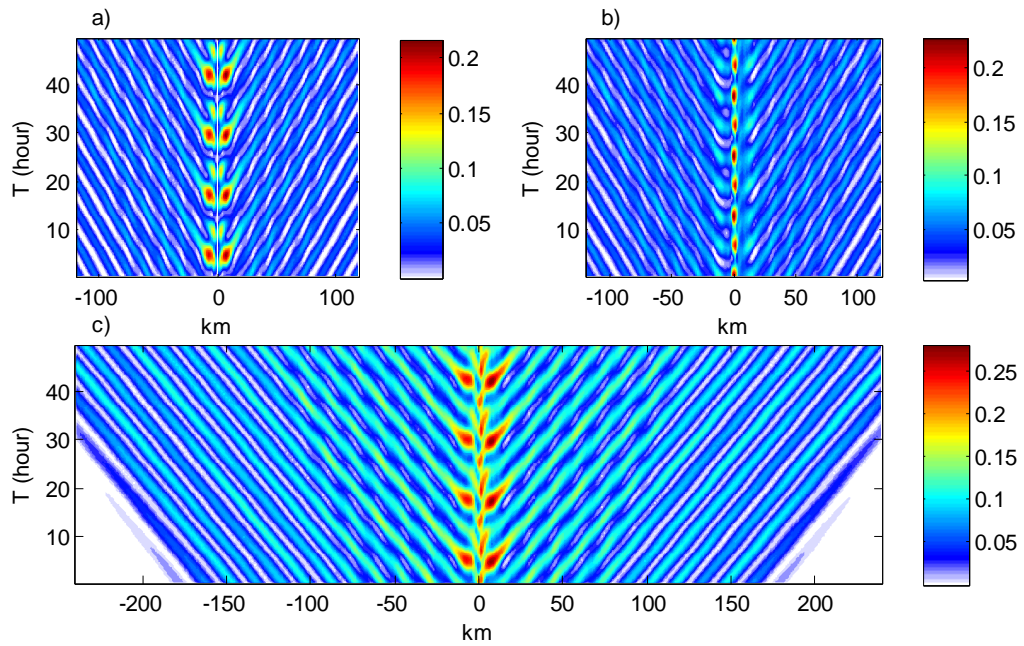


Figure 3.11. Temporal evolution of APE, KE, and APE plus KE for Exp_Ref, a) APE, b) KE, and c) APE+KE.

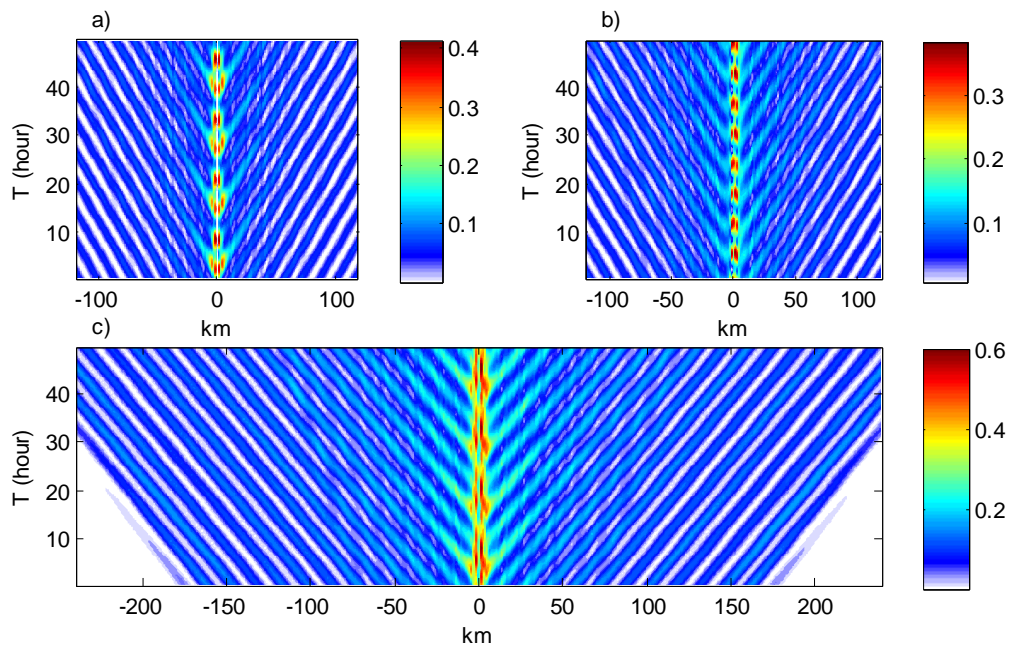


Figure 3.12. Temporal evolution of APE, KE, and APE plus KE for Exp_width18, a) APE, b) KE, and c) APE+KE.

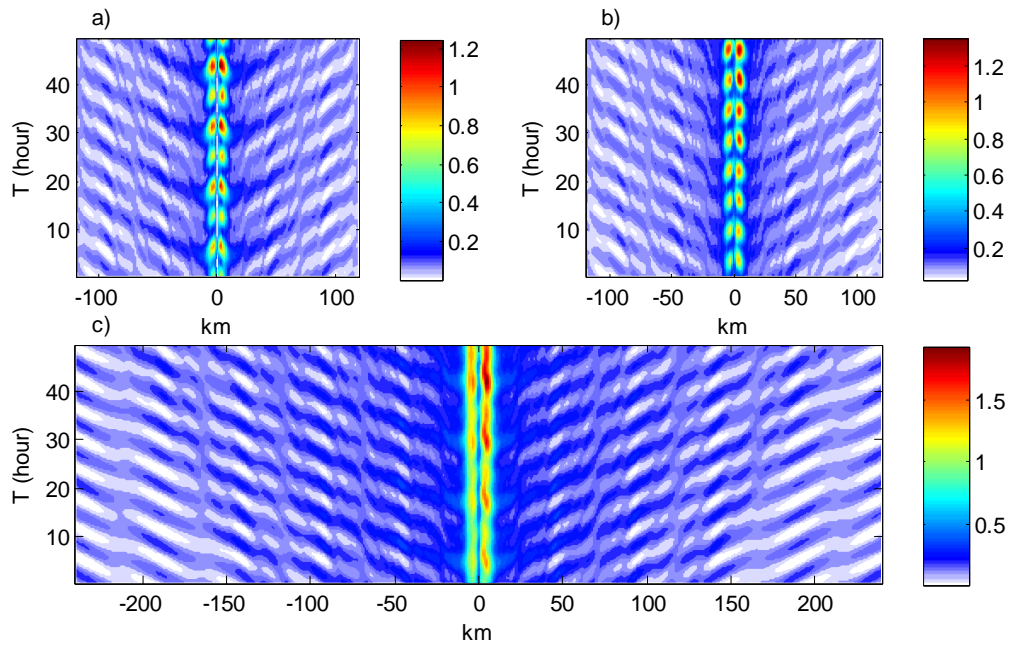


Figure 3.13. Temporal evolution of APE, KE, and APE plus KE for Exp_N2.5, a) APE, b) KE, and c) APE+KE.

3.5 The spectra

In terms of the linear theory, internal tides are generated at the fundamental frequency and harmonic frequencies. In order to understand the solutions from numerical simulations, we analyze the spectra of the baroclinic velocities from several cases. The spectra of the vertical and horizontal baroclinic velocities for Exp_Ref at two points are shown in Fig. 3.14. Point A is just at the center of the domain, and Point B locates at 60 km east of the center of the domain. The baroclinic velocities are calculated over four tidal cycles from the seventh tidal cycle to the eleventh tidal cycle and scaled by the barotropic velocity. It should be noticed that both the time that we choose to do the spectra and the length of the velocity data have some influence on the spectra. The spectra of horizontal baroclinic velocities (point A u and point B u) have peaks at the fundamental frequency ω , 2ω and 3ω . Furthermore, the values at 2ω and 3ω are much smaller than the values at the fundamental frequency, and there is very small energy at the other higher harmonic frequencies. The peak at Point A is much larger than the peak at Point B at fundamental frequency and smaller than the peak at point B at 2ω . The spectra of vertical velocities have a different pattern compared with the spectra of the horizontal velocities. In terms of the volume continuity equation, we can predict that the vertical velocities have much smaller amplitudes than the horizontal velocities. The spectra of vertical baroclinic velocities (point A w and point B w) are also shown in Fig. 3.14. The peaks of the vertical baroclinic velocities are much smaller than the peaks of horizontal baroclinic velocities, indicating that the amplitude of vertical velocities are much smaller than the amplitudes of horizontal velocities. The spectra of vertical baroclinic velocities also differ on the locations: the spectra at point A have a peak at 2ω and the spectra at point B have a peak at ω .

The sensitivity of the spectra to the barotropic velocity is also investigated. Fig. 3.15 shows the spectra of baroclinic velocity u' for Exp_Ref, Exp_u0.05, Exp_u0.10 and Exp_u0.20 at point B ($x=60$ km, $z=-1000$ m), respectively. The baroclinic velocities are scaled by u_0 . The patterns of the four spectra for the four cases are similar in many aspects: the spectra for Exp_Ref, Exp_u0.05 and Exp_u0.10 have peaks at ω , 2ω and 3ω . But the spectrum for Exp_u0.20 doesn't have an obvious peak at 2ω and the spectrum for Exp_u0.10 has peaks at 1.5ω , 2.5ω , and 3.5ω . More energy is transferred into higher harmonics, when the amplitude of

the barotropic tide is larger. The spectra of baroclinic velocity w' for Exp_Ref, Exp_u0.05, Exp_u0.10 and Exp_u0.20 at point B ($x=60$ km, $z=-1000$ m) are shown in Fig. 3.16. The spectra for Exp_Ref and Exp_u0.05 have peaks at ω , 3ω and 4ω and a frequency around 2ω . The spectrum for Exp_u0.10 has peaks at ω , 2ω , 3ω and 4ω , while the spectrum for Exp_u0.20 has higher harmonics.

Not only the spectra for cases with isolated sinusoidal ridge topography are calculated, but also the spectra for the case with three sinusoidal ridges topography are analyzed. There is only one difference between the model configurations for the Exp_Ref and Exp_3sinusoidal: there are three sinusoidal ridges in Exp_3sinusoidal, shown in Fig. 3.20. The spectra of baroclinic velocity u' and w' for Exp_3sinusoidal at point A ($x=0$ km, $z=-1000$ m) and point C ($x=100$ km, $z=-1000$ m) are shown in Fig. 3.17. The spectra for Exp_3sinusoidal at Point A are quite similar to the spectra for Exp_Ref at Point A. In addition, the spectra for Exp_3sinusoidal at Point C are quite similar to the spectra for Exp_Ref at point B as shown in Fig. 3.14, though the positions of point B in Exp_Ref and point C in Exp_3sinusoidal used for the calculations are different.

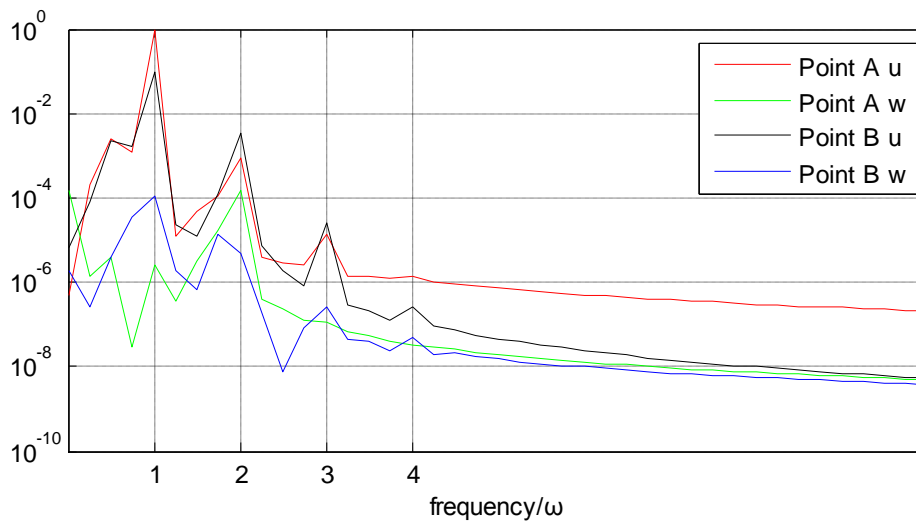


Figure 3.14. The spectra of baroclinic velocity u' and w' for Exp_Ref at point A ($x=0$ km, $z=-1000$ m) and point B ($x=60$ km, $z=-1000$ m), respectively. The baroclinic velocity is scaled by 0.025 m s $^{-1}$ and ω represents the M2 tidal frequency.

3 Tidal flow over sinusoidal topography: the harmonics, energy flux and conversion rate

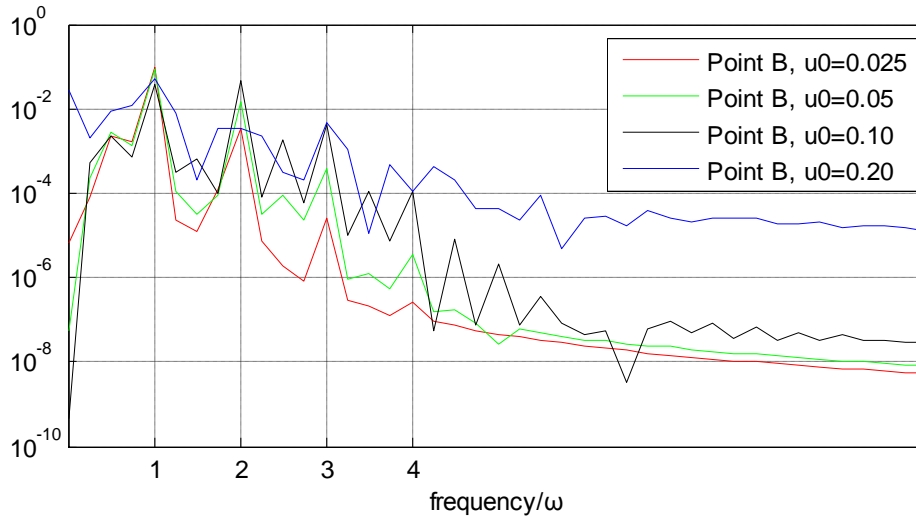


Figure 3.15. The spectra of baroclinic velocity u' for Exp_Ref, Exp_u0.05, Exp_u0.10 and Exp_u0.20 at point B ($x=60$ km, $z=-1000$ m), respectively. The baroclinic velocity is scaled by u_0 and ω represents the M2 tidal frequency.

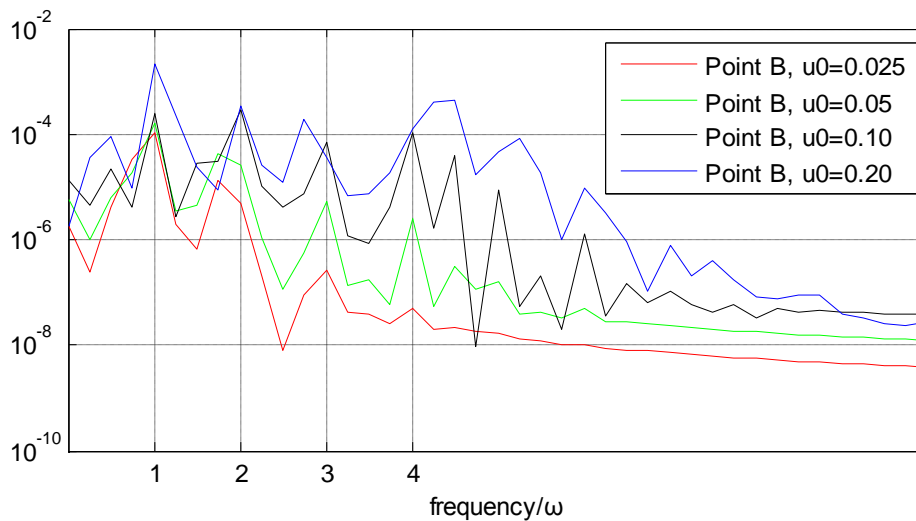


Figure 3.16. The spectra of baroclinic velocity w' for Exp_Ref, Exp_u0.05, Exp_u0.10 and Exp_u0.20 at point B ($x=60$ km, $z=-1000$ m), respectively. The baroclinic velocity is scaled by u_0 and ω represents the M2 tidal frequency.

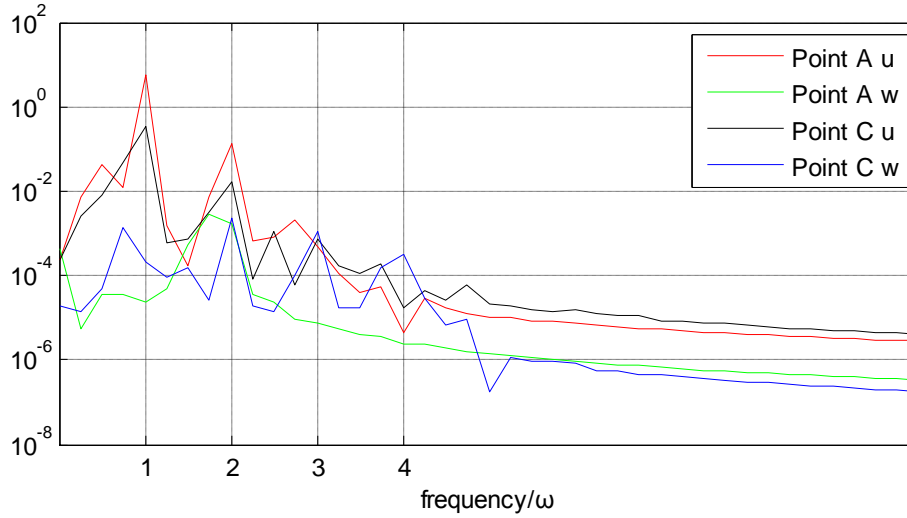


Figure 3.17. The spectra of baroclinic velocity u' and w' for Exp_3sinusoidal at point A ($x=0$ km, $z=-1000$ m) and point C ($x=100$ km, $z=-1000$ m), respectively. The baroclinic velocity is scaled by 0.025 m s $^{-1}$ and ω represents the M2 tidal frequency.

3.6 The harmonics

Numerical simulations show that nonlinear interactions between two topographically generated beams can generate internal wave beams (Lamb, 2004). Here, the horizontal baroclinic velocities calculated from Exp_Ref and Exp_3sinusoidal are chosen as samples to investigate the nonlinear interaction between different beams. Two methods are used to separate the harmonic frequencies from the fundamental frequency.

Firstly, we use the following formula to fit the baroclinic velocity,

$$u'(x, z, t) = A_1 \sin(\omega t + \theta_1) + A_2 \sin(2\omega t + \theta_2) + A_3 \sin(3\omega t + \theta_3). \quad (3.2)$$

Where u' is the baroclinic velocity, A_1 , A_2 and A_3 are the amplitudes for mode 1, 2 and 3 waves, θ_1 , θ_2 and θ_3 are the phases for mode 1, 2 and 3 waves. ω is the M2 tidal frequency. The baroclinic velocities are calculated over two tidal cycles from the seventh tidal cycle to the ninth tidal cycle. The amplitudes and phases of the internal tides for the first three modes can be obtained using the above formula. The full baroclinic velocity, velocities of mode 1 wave and mode 2 wave calculated from Exp_Ref are shown in Fig. 3.18. The maximum amplitude of mode 2 wave is smaller than one tenth of the amplitude of mode 1 wave. But for Exp_3sinusoidal (Fig. 3.19), the mode 2 wave and mode 3 wave almost have the same amplitude which is

about 1/5 of the amplitude of mode 1 wave. The amplitude of mode 2 wave calculated from Exp_Ref is smaller than one calculated from Exp_3sinusoidal. It means that more harmonics will be generated in the case with three-sinusoidal topography, because the internal tides generated by different ridges will interact with each other.

Secondly, we follow the formula described by Lamb (2004) to calculate the modes of the baroclinic velocity,

$$u_n(x, z, t) = \frac{1}{T} \int_{t_1}^{t_1+2T} u'(x, z, t) \cos(n\omega t) dt. \quad (3.3)$$

Where T means one tidal circle, t_1 is the seventh tidal cycle and $n=1, 2, 3, \dots$. The mode 1 and mode 2 waves for Exp_Ref are shown in Fig. 3.20 and the mode 1, mode 2 and mode 3 waves for Exp_3sinusoidal are shown in Fig. 3.21. The maximum amplitude of mode 2 wave is smaller than one tenth of the amplitude of mode 1 wave, as shown in Fig. 3.20. But for Exp_3sinusoidal (Fig. 3.21), the maximum amplitude of mode 2 wave is about 1/4 of the amplitude of mode 1 wave, while the maximum amplitude of mode 3 wave is about 1/8 of the amplitude of mode 1 wave. In addition, the results shown in Fig. 3.20 and Fig. 3.18 are similar, but mode 2 wave using the second method has a larger amplitude of $2 \times 10^{-3} \text{ m s}^{-1}$; the results shown in Fig. 3.21 and Fig. 3.19 are also similar, but mode 3 wave using the second method has a smaller amplitude. The results using both the methods show the mode 1 wave has the most energy for the two cases.

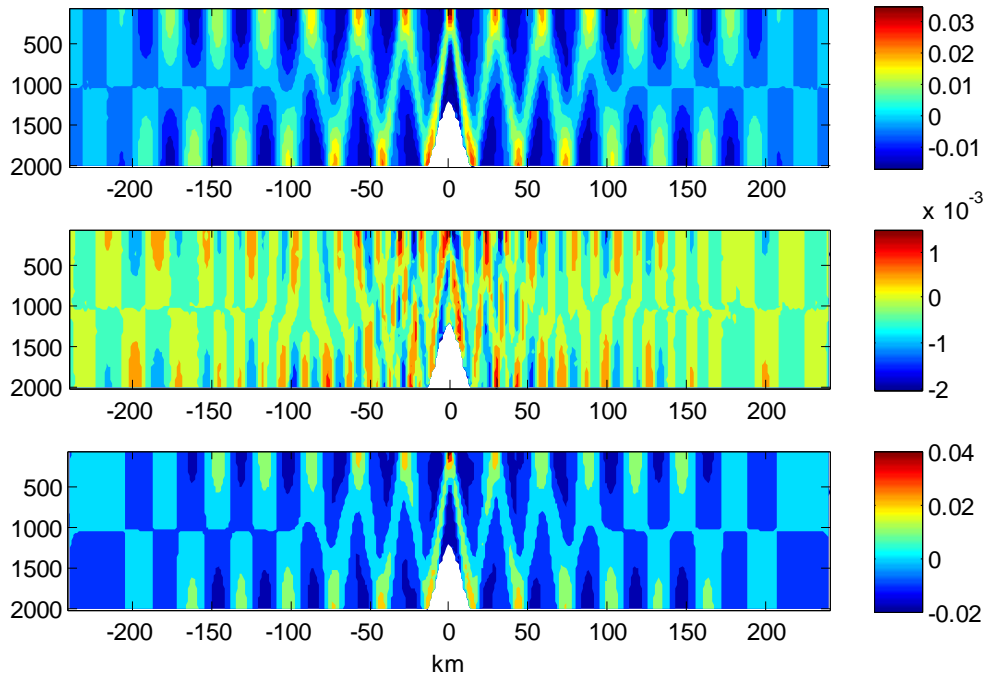


Figure 3.18. The baroclinic velocity field for Exp_Ref: (top) mode 1, (middle) mode 2, and (bottom) full baroclinic velocity obtained by the first method.

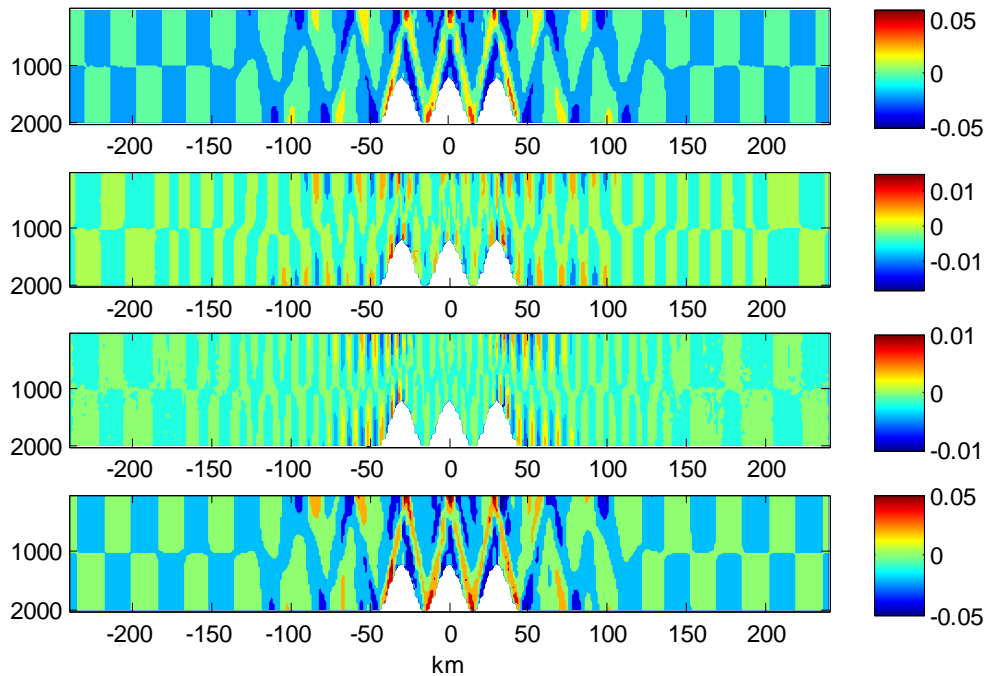


Figure 3.19. The baroclinic velocity field for Exp_3sinsoidal: (top) mode 1, (second) mode 2, (third) mode 3, and (bottom) full baroclinic velocity obtained by the first method.

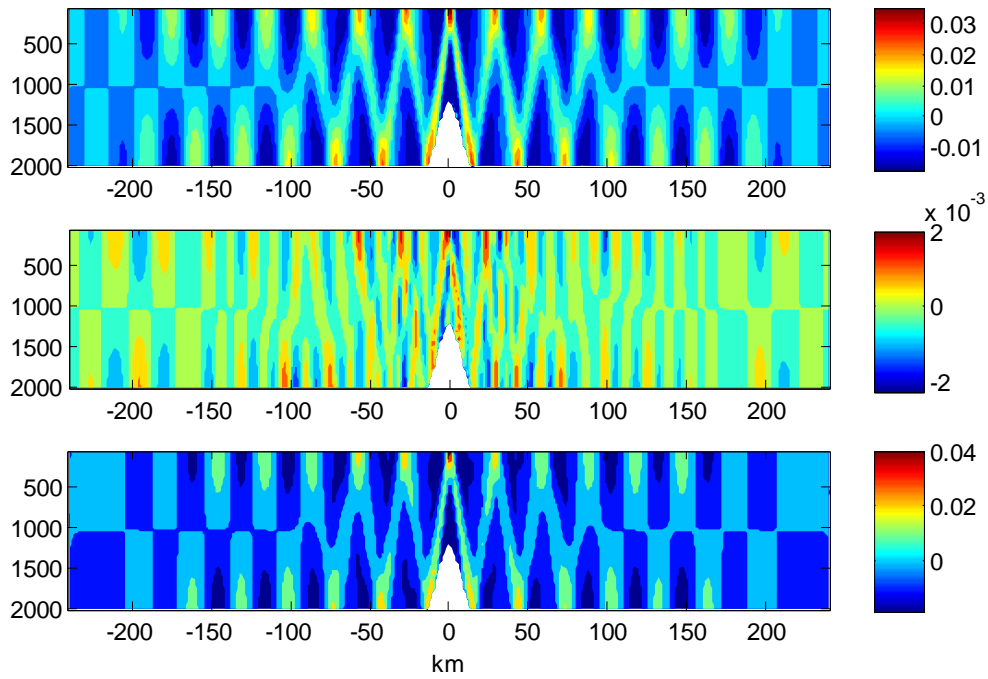


Figure 3.20. The baroclinic velocity field for Exp_Ref: (top) mode 1, (middle) mode 2, and (bottom) full baroclinic velocity obtained by the second method.

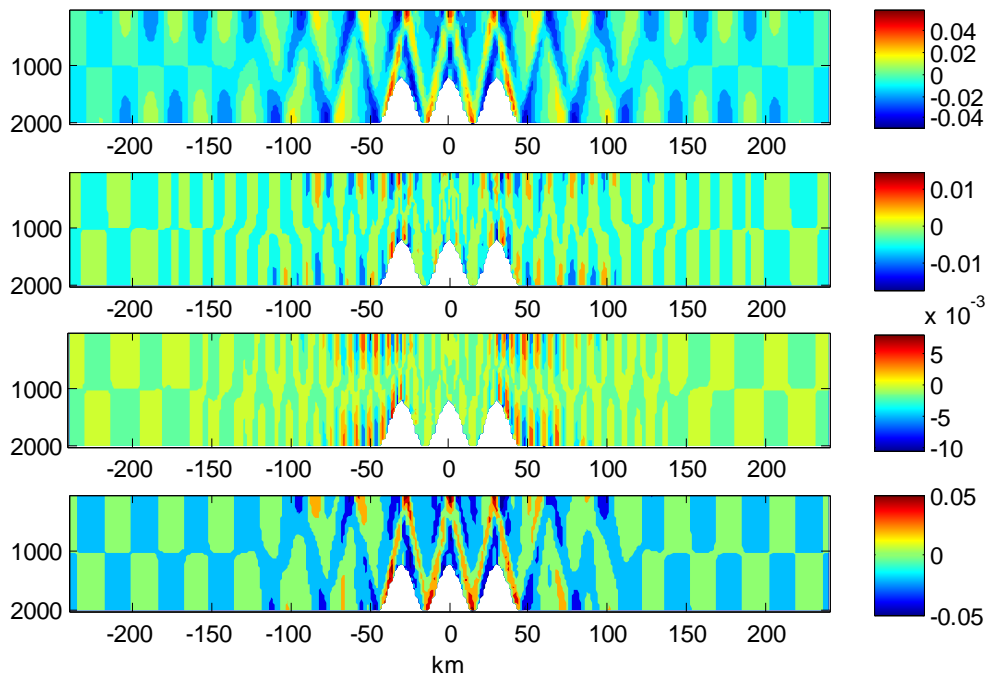


Figure 3.21. The baroclinic velocity field for Exp_3sinoidal: (top) mode 1, (second) mode 2, (third) mode 3, and (bottom) full baroclinic velocity obtained by the second method.

3.7 The energy flux and conversion rate

The conversion rate from the barotropic tide to the baroclinic tide usually is defined in two ways. When the nonlinear and dissipative terms are zero, the first method of calculating the conversion rate (this is also called the energy flux) used in Di Lorenzo et al. (2006) is

$$C1 = \frac{1}{nT} \int_t^{t+nT} \int_{-h}^{\eta} [p'(x, z, t)u'(x, z, t)|_{x=x_0} - p'(x, z, t)u'(x, z, t)|_{x=-x_0}] dz dt, \quad (3.4)$$

where t is the beginning of the seventh tidal cycle, $T=1$ tidal cycle, $n=4$, x_0 and $-x_0$ are located where the height of the ridge goes to zero. It means the energy flux radiated away from the domain. And the second method of calculating the conversion rate which means the work done to the bottom topography is

$$C2 = \int_{-L/2}^{L/2} p'(x, z = h(x), t)U(x, t) \frac{dh}{dx} dx, \quad (3.5)$$

where L is the length of the domain, h is the depth of the topography and the perturbation pressure p' contains the hydrostatic and nonhydrostatic parts, but it doesn't contain the free-surface elevation. However, Khatiwala (2003) and Legg and Huijts (2006) calculated the conversion rate containing the influence of the free-surface elevation. In their paper, the perturbation pressure is defined by

$$p'(x, z, t) = \rho_0 g(\eta - \eta_{bt}) + p(x, z, t) - p_0(z), \quad (3.6)$$

where η_{bt} is the barotropic free-surface height. Both the barotropic free-surface height and the barotropic velocity U were got from a companion barotropic model.

In this chapter, both methods using $C2$ are investigated: firstly, we use the data both from the baroclinic model and companion barotropic model following the method in Khatiwala (2003) and Legg and Huijts (2006) to calculate the conversion rate; secondly, we only use the data from the baroclinic model and ignore the surface contribution to calculate the conversion rate. For Exp_Ref, the value calculated using the data which is only obtained from the baroclinic model is a little smaller, but not differ a lot. Thus, for simplicity, all the results listed in the following are based on the data which is only got from the baroclinic model and doesn't include the data from the companion barotropic model.

The conversion rate of internal tide has been studied in theory in previous research. For a single sinusoidal topography, the conversion rate (Balmforth et al., 2002) is

3 Tidal flow over sinusoidal topography: the harmonics, energy flux and conversion rate

given by

$$C = \frac{\pi\rho_0 U_0^2 h_0^2}{8\omega_0} \sqrt{(N^2 - \omega_0^2)(\omega_0^2 - f_0^2)} \varphi(\epsilon), \quad (3.7)$$

$$\varphi(\epsilon) = 1 + \frac{\epsilon^2}{4} + \frac{11\epsilon^4}{96} + \frac{143\epsilon^6}{2304} + \frac{4513\epsilon^8}{122880} + \frac{170791\epsilon^{10}}{7372880} + O(\epsilon^{12}), \quad (3.8)$$

when $\epsilon < 1$, $\mu = \sqrt{\frac{N^2 - \omega_0^2}{\omega_0^2 - f_0^2}}$. Where $\epsilon = \frac{dh}{dx} * \mu$ and we use the maximum slope from model to replace the slope calculated by formula. Since the model has a coarse resolution, there will be error generated due to the model resolution (see Di Lorenzo et al., 2006).

The depth-integrated and time-averaged energy fluxes for all cases are calculated. All results are averaged over 4 tidal cycles from the seventh tidal cycle and scaled by $P = \frac{\pi\rho_0 U_0^2 h_0^2}{8\omega_0} \sqrt{(N^2 - \omega_0^2)(\omega_0^2 - f_0^2)}$. The energy fluxes calculated from four cases with different heights of the topography are shown in Fig. 3.22(a). The patterns of the energy fluxes for the four experiments are similar. The eastward energy flux decreases at points far away from the point at 15 km, and the westward energy flux decreases at points far away from the point at -15 km. The amplitude of the scaled energy flux are similar, indicating that the energy flux is almost proportional to the square of the height of the topography. However, when the height of the topography is larger, the scaled-result will be a little larger. The depth-integrated time-averaged scaled energy fluxes for the cases with different barotropic velocities are shown in Fig. 3.22(b). The scaled energy flux are almost the same to each other, indicating that the energy flux is proportional to the square of the amplitude of the barotropic tide. The sensitivity of the energy flux to the stratification is shown in Fig. 3.22(c). It is found that when the stratification is weak, there will be almost no energy flux generated. The scaled-energy flux is larger, when the stratification is stronger. Fig. 3.22(d) shows that the energy flux is very small, when the width of the topography is 54 km, and the scaled-energy flux will be larger when the width of the topography is smaller. Hence, the energy flux can be parameterized by $P = \frac{\pi\rho_0 U_0^2 h_0^2}{8\omega_0} \sqrt{(N^2 - \omega_0^2)(\omega_0^2 - f_0^2)} F$, where the F would be a function of the height of the topography, the width of the topography and the stratification.

The comparison of the results predicted by the linear theory (Balmforth et al., 2002) and the model results is shown in Fig. 3.23, and all the results are scaled by $P = \frac{\pi\rho_0 U_0^2 h_0^2}{8\omega_0} \sqrt{(N^2 - \omega_0^2)(\omega_0^2 - f_0^2)}$. Fig. 3.23a) shows that the scaled conversion rate

increases with the increased height of the topography. The results predicted using the linear theory agree well with the results calculated by C1, but the results calculated by C2 are much larger than the results predicted using the linear theory and the results calculated by C1 in cases in which the heights are 800 m and 1600 m. Fig. 3.23b) shows that the theoretical predictions agree well with results calculated by C1. For a subcritical topography, the conversion rate is proportional to the square of the amplitude of the barotropic tide, and the results calculated by C2 are larger than the results calculated by C1 and the results predicted using the linear theory. Fig. 3.23c) shows the conversion rate is really dependent on the stratification. The conversion rate will be larger, when the stratification is stronger. When the stratification is too weak, there will be almost no conversion rate. Fig. 3.23d) shows that the conversion rate decreases with the increased width of the topography. The linear theory is well when the width is 30 km, but the results calculated by C1 and C2 in 54 km case are different with the results predicted using the linear theory. To sum up, the theoretical predictions can agree well with the results calculated by C1 in experiments with suitable height of the topography, velocity, stratification and width of the topography.

The formula C2 which represents the force on the topography has been used in much past research. There is an obvious difference between the results calculated by C1 and C2. We suggest that the existence of the difference not only because there is the tendency part and dissipation part between the two terms in baroclinic energy equation, but also there is a limitation of the accuracy of the calculation using this formula. As shown in Fig. 3.23, if the dh/dx is large or h is very large, the difference between the results calculated by C1 and C2 will be larger. In addition, the differences between the results using the two methods from cases with the same topography and stratification as shown in Fig. 3.23 b) are similar. In Legg and Huijts (2006), the values in the cases with large h or dh/dx are almost 2 times larger than the results using the linear theory, and the linear theory is good for 'low wide' topography. The 'calculation error' may be one of the reasons for the difference. The other reasons are that the other cases in Legg and Huijts (2006) are supercritical cases and the conversion rate for supercritical cases is larger than the conversion rate for the subcritical cases. In conclusion, we suggest that the formula C2 may bring some 'calculation error' for the conversion rate in numerical simulations, or the difference between the results calculated by C1 and C2 may be a function of dh/dx or h .

3 Tidal flow over sinusoidal topography: the harmonics, energy flux and conversion rate

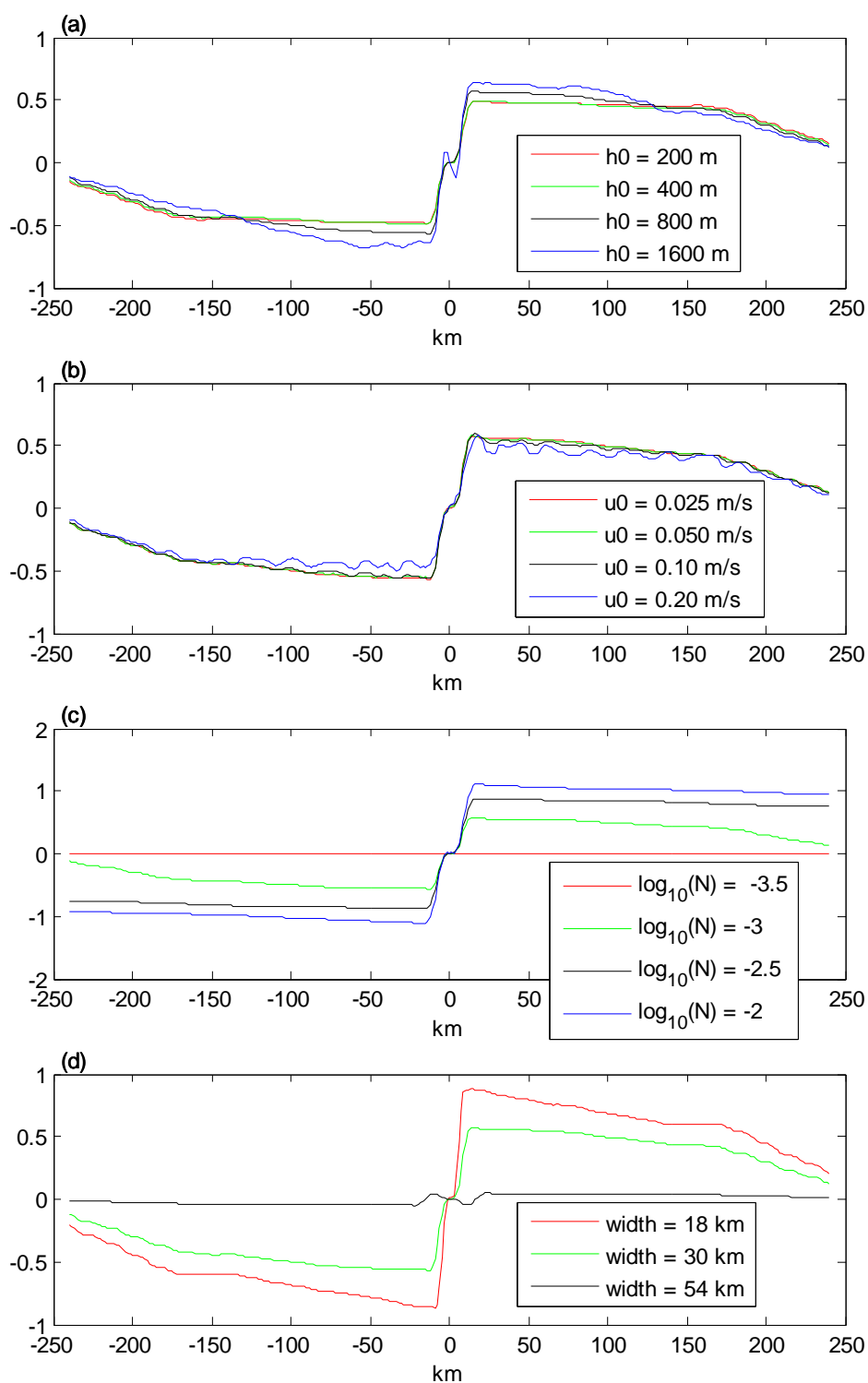


Figure 3.22. Depth-integrated and time-averaged energy flux scaled by $P = \frac{\pi \rho_0 U_0^2 h_0^2}{8 \omega_0} \sqrt{(N^2 - \omega_0^2)(\omega_0^2 - f_0^2)}$, (a) different heights of the topography, (b) different barotropic velocities, (c) different stratifications, and (d) different widths of the topography.

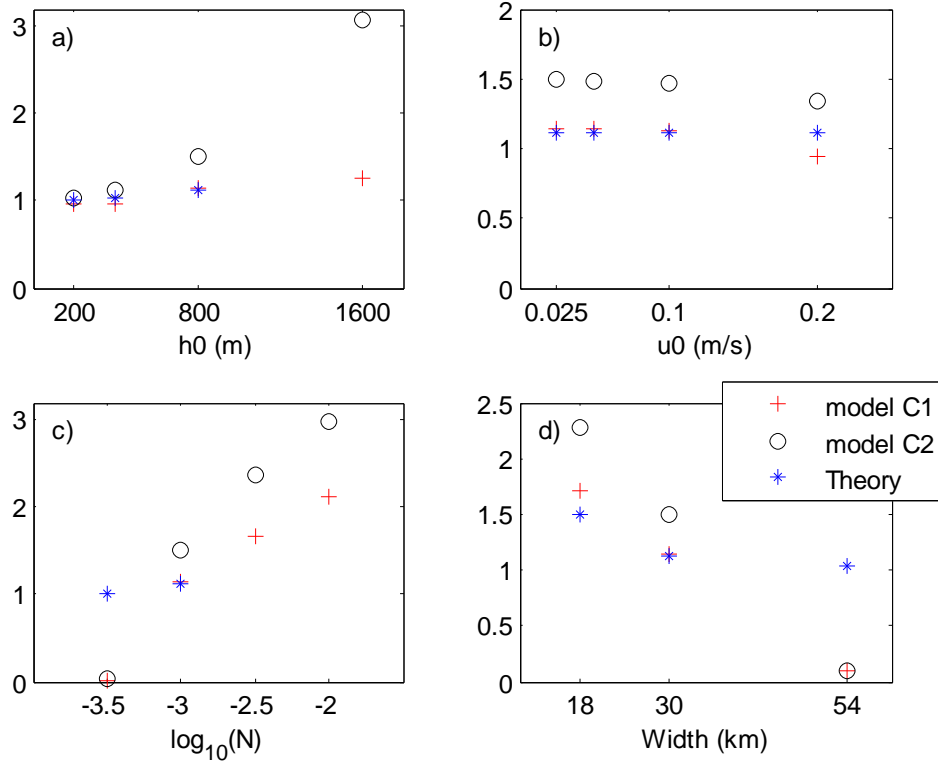


Figure 3.23. The conversion rate scaled by $P = \frac{\pi\rho_0 U_0^2 h_0^2}{8\omega_0} \sqrt{(N^2 - \omega_0^2)(\omega_0^2 - f_0^2)}$, a) different heights of the topography, b) different barotropic velocities, c) different stratifications, and d) different widths of the topography. The model C1 is calculated using the equation (3.4); the model C2 is calculated using the equation (3.5); and Theory is calculated using equations (3.7-3.8), where $\varphi(\epsilon)$ is got from the first six terms.

3.8 Discussion and conclusion

Table 3.2. The conversion rate scaled by $P = \frac{\pi\rho_0 U_0^2 h_0^2}{8\omega_0} \sqrt{(N^2 - \omega_0^2)(\omega_0^2 - f_0^2)}$.

Values/Cases	Exp_h200	Exp_h400	Exp_Ref	Exp_h1600
C1	0.96	0.97	1.14	1.27
C2	1.03	1.11	1.50	3.07
Values/Cases	Steep_h200	Steep_h400	Steep_800	Steep_h1600
C1	0.91	0.93	1.04	1.10
C2	0.98	1.07	1.38	2.74

Lamb and Kim (2012) set up experiments in which the topographies with three different shapes are used to investigate the conversion rate transferred from barotropic tide to baroclinic tide over a shelf slope. The energy flux depends on the topographic spectrum in terms of linear tide theory, thus the energy fluxes are different in experiments with different topographic shapes. In this paper, four cases with steep topography are added to compare with the results from cases with sinusoidal topography. The steep topography in the middle of the domain is represented by

$$h = (2000 - h_0) \times \left(1 - \frac{(1500n)^2}{15000^2}\right) - 2000, \quad (3.9)$$

where h (m) is the depth of the topography used in the model, h_0 is the height of the ridge and $n = (-10: 10)$. In Table 3.2, Steep_h200 means $h_0 = 200$, and so on. All configurations except the topography in the four cases with steep topography are the same with ones in Exp_Ref. We can see in Table 3.2 that the conversion rates from cases with steep topography are a little smaller than ones from cases with sinusoidal topography using the same height, thus the topographic shape is important for the accuracy of calculating the conversion rate. Though the results are a little different for different shapes, but the estimates predicted by the linear theory here are also good for the results calculated from cases with steep topographies in a certain allowable range.

The above analyses show that the factors of the height of the topography, the amplitude of the barotropic tide, the stratification and the width of the topography have an obvious influence on the baroclinic velocity. When the height of the topography increases, the generated baroclinic velocity will be larger. The pattern of baroclinic velocity fields do not change too much in experiments with different amplitudes of the barotropic tide. The stratification is really an important factor. If the stratification is too weak, there will be almost no baroclinic velocity generated. If the stratification is stronger, the baroclinic velocity will be larger. The width of topography has an influence on the pattern of baroclinic velocity field.

APE, KE, and APE plus KE are shown in this paper, and there are different patterns between in subcritical cases and in supercritical cases. Through the velocity spectra, it is found that the spectra of the horizontal velocity and of the vertical velocity are quite different. Through calculating the modes of baroclinic velocities by two methods, we find that mode 1 wave has the most energy in all experiments.

The amplitudes of mode 2 wave in Exp_3sinusoidal are larger than the results in Exp_Ref.

The depth-integrated and time-averaged energy flux is analyzed. The energy flux can be parameterized by $P = \frac{\pi\rho_0 U_0^2 h_0^2}{8\omega_0} \sqrt{(N^2 - \omega_0^2)(\omega_0^2 - f_0^2)} F$, where the F would be a function of the height of the topography, the width of the topography and the stratification. Comparing with the difference between the results calculated by C1, C2 and the results predicted by the linear theory, we can see that the values of conversion rate predicted by the theory (Balmforth et al., 2002) can compare well with the numerical values in most subcritical cases. The stratification, the height and width of the topography, the amplitude of the barotropic tide and the topographic shape are all important factors. At last, we must notice that the conversion rates calculated by C1 and C2 are much smaller than the values predicted by the linear theory, when there is very weak stratification and the width of topography is too large.

Chapter 4

4 The two-dimensional simulations of internal waves at the Luzon ridge

Abstract

The two-dimensional simulations using MITgcm are performed to study the internal waves at the Luzon ridge, where strong internal tides are generated due to tide-topography interaction and internal solitary waves are generated when the internal tides steepen by nonlinear effects, which have been observed by satellite data and studied by theories and numerical simulations. Based on the previous research, this paper focuses on the energy budget of internal waves and the influences of the height of the west ridge, the distance between the two ridges and the amplitude of the barotropic tide on the generation of internal waves. Analysis of the baroclinic energy budget of internal waves shows that the conversion rate is mainly balanced by the energy flux. The model results also show that when the height of west ridge increases, both the conversion rate and the energy flux increase; the internal waves are enhanced due to a suitable distance between the two ridges, moreover, the conversion rate and the energy flux are the largest when the distance between the two ridges is 100 km; the amplitude of the barotropic tide is one of the crucial factors to determine whether the internal solitary waves would be generated or not, furthermore, when the amplitude of the barotropic tide is larger, the speed of the internal solitary waves generated will be larger.

4.1 Introduction

The Luzon ridge, which comprises of two meridional ridges: the lower west ridge and the higher east ridge, is one of the most important generation sites for the internal tides and nonlinear waves (Niwa and Hibiya, 2004; Ramp et al., 2004; Zhao and Alford, 2006; Jan et al., 2008; Li and Farmer, 2011; Alford et al., 2015; Xu et al., 2016). When the barotropic tides flow over the ridges, the internal tides will be generated. Then, part of the internal tides will dissipate locally. Part of the internal

tides will either propagate into Pacific Ocean or into the South China Sea. Internal tides may evolve into solitary waves in the northern of South China Sea. In the ocean, the internal waves generated by barotropic tides and geostrophic flows play an important role in the turbulent mixing (Munk and Wunsch, 1998; Kunze et al., 2006; Garrett and Kunze, 2007; Nikurashin and Ferrari, 2011).

The characters of internal tides at the Luzon ridge have been studied using Both two- and three-dimensional simulations (Jan et al., 2007; Jan et al., 2012; Buijsman et al., 2012a). The energetics of M2 internal tide in the East of China Sea was studied using POM in Niwa and Hibiya (2004). The baroclinic conversion rate, the baroclinic energy flux and the baroclinic dissipation in their standard experiment at the Luzon ridge were 14.9, 9.0 and 5.9 GW, respectively. The results didn't change too much, when the horizontal resolution, vertical level number and topography averaging radius changed. The internal tide resonance was studied using MITgcm in two-dimensional and three-dimensional simulations in Buijsman et al. (2014). Their models were forced by eight barotropic tidal currents at the boundaries and the internal tides generated are then separated into the semidiurnal and diurnal parts. They found that most of resonance occurred for the first mode. The conversion rate from the M2 barotropic tide to the baroclinic tide in the Philippine Sea was studied using ROMS in Kerry et al. (2014). They showed that the mean conversion rate at the Luzon strait over 2010 was 16.21 GW. The above research showed that strong internal tides are generated at the Luzon ridge: part of the energy radiates away from the generation site and the residual energy dissipates locally. Furthermore, the internal tides which propagate westward away from their generation site may disperse into solitary waves (Buijsman et al., 2010a, b; Zhang et al., 2011).

The generation and propagation of nonlinear waves in the Northern portion of the South China Sea have been investigated in much research. Alford et al. (2010) studied the nonlinear internal waves transiting the South China Sea in detail using data from mooring during the period 26 April- 7 May 2007, and the type A and B waves were found in their research. Buijsman et al. (2010a) used ROMS to study the nonlinear internal waves in the South China Sea. In this research, the topography was represented by an ideal Gaussian ridge and it was found that the weak soliton trains were generated when the internal tides propagated and steepened by nonlinear effects. Buijsman et al. (2010b) used ROMS to study the nonlinear waves in the Luzon Strait in idealized two-dimensional simulations. The influences of the

distance between the two ridges, the Kuroshio and the height of the ridges on the generation of nonlinear waves were studied. It was found that the asymmetric modulated barotropic tide may cause asymmetric solitons on the west and east side of the two ridges. In addition, the numerical simulations of nonlinear internal waves in the South China Sea can also be found in Cai et al. (2002), Warn-Varnas et al. (2010), Zhang et al. (2011), and Wu et al. (2013).

The energy budgets of internal waves derived based on the Navier-Stokes equation have been developed recently. Cater et al. (2008) used three-dimensional Princeton Ocean Model (POM) to simulate internal tides in the region of Hawaiian Ridge. In their paper, they separated the equation into the barotropic and baroclinic parts, and their conversion rate from barotropic flow to baroclinic flow could be numerically calculated by $C = p'(-H) \cdot \bar{u} \cdot \nabla H$, where p' is the perturbation pressure, \bar{u} is the barotropic velocity and H is bottom topography. The formula has also been used in Khatiwala (2003), Legg and Huijts (2005), Zilberman et al. (2009) and Buijsman et al. (2012a). In contrast, Kelly et al. (2010) used $C = p'(-H) \cdot \bar{u} \cdot \nabla H + p'(0) \cdot \frac{\partial \eta}{\partial t}$ to define the conversion rate, where η is the surface elevation, which contains the energy conversion through the free surface. This formula has been used in Tanaka et al. (2013) and Ponte and Cornuelle (2013). Furthermore, Kang and Fringer (2012) derived the barotropic and baroclinic energy equations in a different way, and the depth-integrated conversion rate could be obtained by $\bar{C} = \overline{\rho' g W} - \overline{\frac{\partial q}{\partial z} W}$, where ρ' is the perturbation density, W is the convergence of the barotropic flow in the water column from the bottom to the depth z and q is the nonhydrostatic pressure. Based on the energy budgets derived for the models, not only the conversion rate but the other terms such as the energy flux, the dissipation and the tendency can be easily calculated.

To supplement the former research on the internal waves at the Luzon ridge, the influences of the height of the west ridge, the distance between the two ridges and the amplitude of the barotropic tide on generation of internal waves are further studied. Here, the two-dimensional numerical simulations are performed to study the characters of both the internal tides and the internal solitary waves. The topography used in the model is represented by two Gaussian ridges and the baroclinic energy equation derived by Kang and Fringer (2012) is used to understand the energy budget of internal tides. The paper is organized as follows: in section 4.2, the model

configuration is described; in section 4.3, the spectra of baroclinic velocities are presented; in section 4.4, the baroclinic energy equation is shown and the results of the energy budget are analyzed; in section 4.5, the sensitive experiments are discussed. The conclusion part is shown in section 4.6.

4.2 Model

The nonhydrostatic MITgcm (Marshall et al., 1997) which has been widely used in many past studies (Kang and Fringer, 2012; Rapaka et al., 2013; Jalali et al., 2014) is used for the two-dimensional internal wave simulations.

The Luzon Strait, which connects the western Pacific Ocean and the South China Sea, features two meridional ridges. The east ridge has been proved to be crucial for the generation of internal tides. The west ridge plays a different role: it would be another source to the generation of internal tides or it is a barrier to the internal tides generated by the east ridge (Chao et al., 2007). Here, two Gaussian ridges $h = 2600 \times e^{-\left(\frac{x}{24000}\right)^2} + 1300 \times e^{-\left(\frac{x-100000}{24000}\right)^2}$ are used to represent the topography in 20.5 °N, which means the height of the east ridge is 2600 m and the height of the west ridge is 1300 m. It simplifies the complicated topography at the Luzon ridge and the factors such as the height of the west ridge can be easily adjusted using the topography. This method of dealing with topography is similar to the methods used in Li and Farmer (2011) and Buijsamn et al. (2010b).

The horizontal size of the domain is 1200 km, which covers the longitude from 115 °E to 126.5 °E. The horizontal grid spacing is 300 m and the vertical grid spacing is 20 m. As we know, there has been some research focusing on the shoaling of the internal solitary waves on the continental shelf in the South China Sea (Duda et al., 2004; Chang et al., 2006; Lamb and Warn-Varnas, 2014; Xu et al., 2016). Here we mainly study the influences of the factors on the generation of nonlinear waves and the energy budget of the baroclinic tides, without considering the shoaling affects, thus we set the depth of the area with a uniform value of 3000 m.

In order to get a better simulation of nonlinear waves, we use the realistic horizontal stratification instead of a horizontal uniform stratification. The stratification used in these simulations is firstly calculated from the WOCE climatology in 20.5 °N from 115 °E to 126.5 °E. Then we use a linear function of temperature to fit the stratification. The topography and temperature used in the

paper are shown in Fig. 4.1. The vertical distribution of temperature from -600 km to -300 km is set to be the same to the distribution at -300 km for simplicity, and the stratification in upper 500 m on the west side of the topography is stronger than that on the east side of the topography.

The background horizontal and vertical viscosity and diffusivity are $10^{-1} \text{ m}^2 \text{ s}^{-1}$ and $10^{-5} \text{ m}^2 \text{ s}^{-1}$, respectively. The Coriolis frequency $f_0 = 5.1 \times 10^{-4}$, which represents the value in latitude 20.5°N . The Kpp scheme (Large et al., 1994) and advection temperature scheme 33 are used for all the simulations.

The barotropic tide is forced by adding a body force to momentum equations (Khatiwala, 2003). In this study, the amplitudes of M2 and K1 barotropic tides are 3.5 cm s^{-1} and 5 cm s^{-1} , respectively, which are obtained from the Ocean Topography Experiment TOPEX/Poseidon Global Inverse Solution 7.2 (TPXO7.2) (Egbert et al., 1994) at a point along 20.5°N with a depth of 3000 meters in the standard experiments. The sensitivity to the height of the west ridge, the distance between the two ridges and the amplitude of the barotropic tide is investigated in experiments. The configurations of experiments are shown in Table 4.1. Exp_1, Exp_west1, Exp_west2 and Exp_west3 are used to examine the sensitivity of the generation of internal waves to the height of the west ridge. Exp_dis1, Exp_1, Exp_dis2 and Exp_dis3 are used to examine the sensitivity to the distance between the two ridges, while Exp_u1, Exp_u2, Exp_u3, Exp_1 and Exp_u4 are used to examine the sensitivity to the amplitude of the barotropic tide. All experiments are run for 6 days.

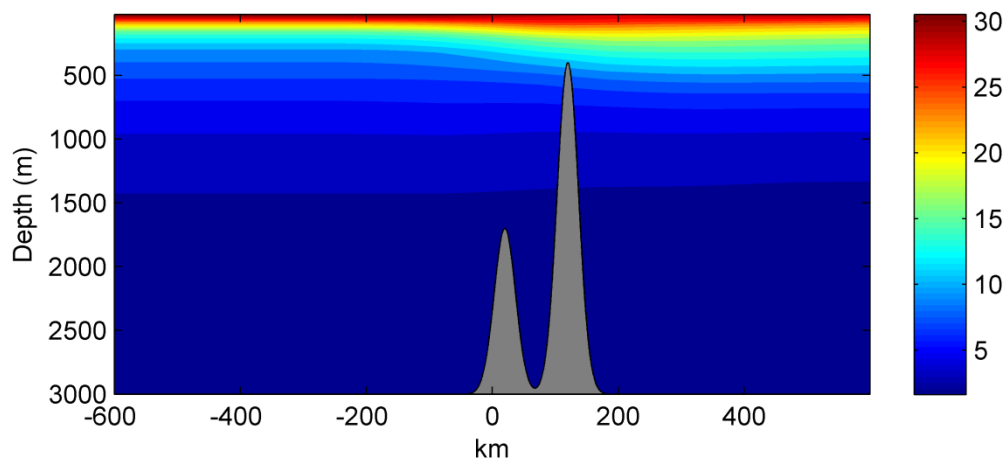


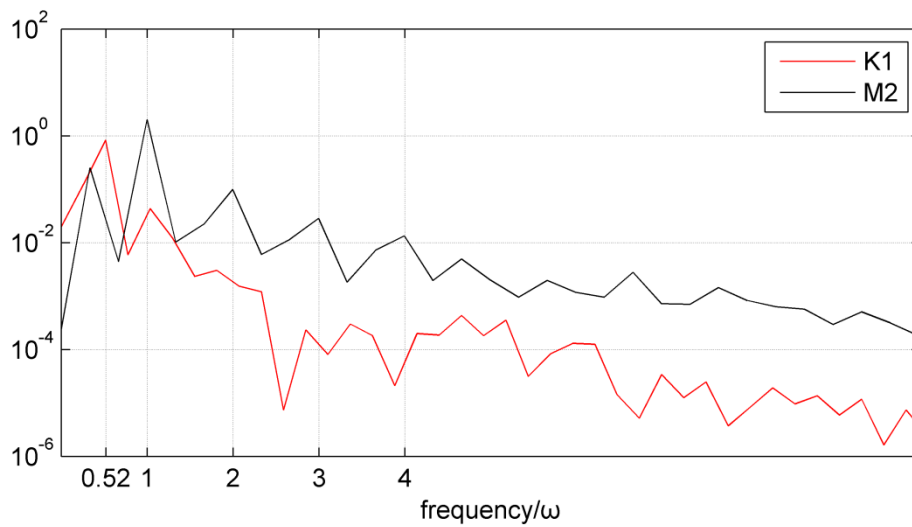
Figure 4.1. The bathymetry with two Gaussian ridges and the temperature ($^{\circ}\text{C}$) used in the model.

Table 4.1. List of Experiments in this Study: the values in all blank cells are the same to Exp_1 in the same column.

Cases	Distance (km)	West (m)	Velocity (m s ⁻¹)	Force
Exp_1	100	1300	0.035	M2
Exp_K1			0.050	K1
Exp_west1		1600		
Exp_west2		1000		
Exp_west3		700		
Exp_dis1	60			
Exp_dis2	140			
Exp_dis3	180			
Exp_u1			0.020	
Exp_u2			0.025	
Exp_u3			0.030	
Exp_u4			0.040	

4.3 The spectra

(a)



(b)

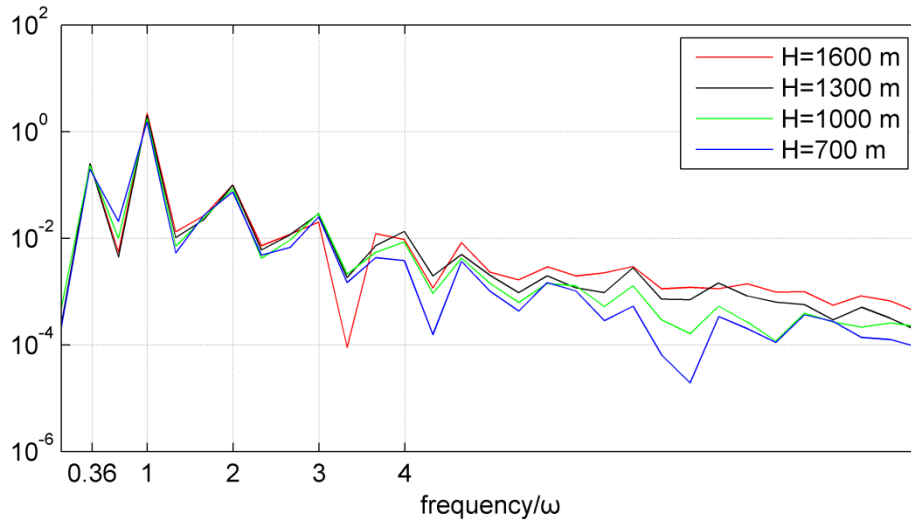


Figure 4.2. The spectra of baroclinic velocity u' for (a) Exp_K1 and Exp_1, and (b) Exp_west1, Exp_1, Exp_west2 and Exp_west3 at point $x=-120$ km, $z=-140$ m. Where H represents the height of the west ridge and ω represents the M2 tidal frequency. The baroclinic velocity is scaled by 0.035 m s^{-1} .

The spectra of baroclinic velocities are shown in Fig. 4.2. The baroclinic velocity u' is the result of the velocity u subtracting the depth-averaged velocity U . The baroclinic velocities used for the calculations are scaled by the barotropic velocity $u=0.035 \text{ m s}^{-1}$ and located at point $x=-120$ km, $z=-140$ m. Fig. 4.2(a) shows the spectra of the scaled baroclinic velocities for M2 tide and K1 tide. The spectrum for Exp_1 represented by black line is calculated using the velocities over 3 M2 tidal cycles after 3.6 M2 tidal cycles. In terms of the linear internal wave theory, we know that the baroclinic velocities generated are at the fundamental frequency and harmonic frequencies. It is shown that the spectrum has peaks at ω , f_0 , 2ω , 3ω , 4ω and the energy is mainly radiated at the fundamental frequency. In contrast, the spectrum for Exp_K1 represented by red line is calculated using the velocities over 2 K1 tidal cycles after 1.4 K1 tidal cycles. The spectrum has peaks at ω_{k1} and $2\omega_{k1}$, where ω_{k1} represents the K1 tidal frequency. In summary, the generated M2 and K1 internal tides mainly radiate energy at their fundamental frequency.

Fig. 4.2(b) shows that the spectra of the scaled baroclinic velocities for Exp_west1, Exp_1, Exp_west2 and Exp_west3. The spectra calculated from four experiments with different heights of the west ridge are quite similar: the generated internal tides radiate energy at the fundamental frequency, f_0 , and harmonic frequencies. Thus, the main structure of internal tides generated don't change too

much, when we change the height of the west ridge in experiments.

4.4 The baroclinic energy budget

4.4.1 Theory

The depth-integrated baroclinic energy equation derived by Kang and Fringer (2012), which is also used in Buijsman et al. (2012a) and Jalali et al. (2014), is used to analyze the energetics of internal tides for two-dimensional simulations. The velocity is divided into the barotropic part and the baroclinic part. The horizontal velocity $\mathbf{u}=(u, v)$, and the barotropic horizontal velocity $\mathbf{U}=(U, V)$. The baroclinic horizontal velocity $\mathbf{u}'(x, z, t) = \mathbf{u}(x, z, t) - \mathbf{U}(x, z, t)$, where $\mathbf{U} = \frac{1}{\eta+h} \int_{-h}^{\eta} \mathbf{u}(x, z, t) dz$ is the depth-averaged velocity, where h is the ocean depth and η is the ocean surface height. The vertical velocity $w = W + w'$, where the barotropic vertical velocity $W(z) = -\nabla \cdot ((h+z)\mathbf{U})$. The total density is $\rho(x, z, t) = \rho_0 + \rho_v(z) + \rho'(x, z)$, where ρ_0 is the constant reference density, ρ_v is the background density and ρ' is the perturbation density. The total pressure is given by

$$\begin{aligned} p(x, y, z, t) &= p_0 + p_v(z) + p'(x, y, z, t) + q, \\ &= \rho_0 g(\eta - z) + g \int_z^{\eta} \rho_v dz + g \int_z^{\eta} \rho' dz + q, \end{aligned}$$

where p_0 is the reference pressure, $p_v(z)$ is the background pressure, and q is the nonhydrostatic pressure. We only care about the baroclinic energy equation, and the depth-integrated baroclinic energy equation is given by

$$\frac{\partial}{\partial t} (\overline{E_k} + \overline{E_p}) + \nabla \cdot \overline{\mathbf{F}} = \overline{C} - \overline{\varepsilon} - \overline{R}, \quad (4.1)$$

where the kinetic energy $E_k = \frac{1}{2} \rho_0 (u'^2 + v'^2 + w^2)$ and the available potential energy $E_p = \frac{g^2 \rho'^2}{2 \rho_0 N^2}$. The total flux which represents the energy radiates away from a

region here $\overline{\mathbf{F}} = \overline{\mathbf{F}_e} + \overline{\mathbf{F}_a} + \overline{\mathbf{F}_d}$, where the energy flux $\overline{\mathbf{F}_e} = \overline{u'p'} + \overline{u'q}$, the advection flux $\overline{\mathbf{F}_a} = \overline{u(E_k + E_p)} + \overline{u'E_{hk}}$, the diffusion flux $\overline{\mathbf{F}_d} = -\overline{A_h \nabla E_k} - \overline{K_h \nabla E_p}$ and the cross term $E_{hk} = \rho_0 (Uu' + Vv')$. The conversion rate which represents the energy

transferred from the barotropic tide to the baroclinic tide $\overline{C} = \overline{\rho' g W} - \overline{\frac{\partial q}{\partial z} W}$ and the

nonlinear conversion rate $\overline{C_n} = \rho_0 H(\overline{U\overline{V} \cdot (u'u')} + \overline{V\overline{V} \cdot (u'v')})$. The dissipation rate $\overline{\varepsilon} = \rho_0 \overline{A_h \left(\frac{\partial \mathbf{u}'}{\partial x}\right)^2} + \rho_0 \overline{A_v \left(\frac{\partial \mathbf{u}'}{\partial z}\right)^2}$, where A_h and A_v are the horizontal and vertical eddy viscosity. The horizontal eddy viscosity A_h is constant and the vertical eddy viscosity A_v is obtained from the model output. In this paper, the residual term \overline{R} contains the diffusion flux $\overline{F_d}$, the nonlinear conversion rate $\overline{C_n}$, the dissipation of E_p , other terms and the off-line calculation error. The diffusion flux $\overline{F_d}$, the nonlinear conversion rate $\overline{C_n}$ and the dissipation of E_p are not calculated, because they are all very small compared with the other terms. The values of the residual term \overline{R} from all the experiments can be clearly seen in Table 4.2.

4.4.2 The energy budget

Table 4.2. The baroclinic energy budget calculated from numerical experiments (W m^{-1})

Cases	$\partial Pe/\partial t$	$\partial Ke/\partial t$	Conversion rate	Energy flux	Advection flux	Dissipation	Residual
1	751.7	809.5	60122.3	57218.5	-700.7	542.7	1500.6
K1	5377.2	13627.5	64364.6	49752.6	218.1	745.3	-5356.1
west1	1347.0	1175.2	65842.0	61253.9	-572.6	593.6	2044.9
west2	434.7	770.9	54846.0	52495.4	-400.1	505.4	1039.7
west3	396.2	795.2	50718.9	48737.2	-110.1	426.9	473.5
dis1	124.0	1182.6	40825.2	38626.7	66.1	339.3	486.5
dis2	680.8	1099.5	43360.2	42245.4	390.9	381.5	-1437.9
dis3	1579.3	2255.2	38546.5	33120.4	-83.8	302.8	1372.6
u1	-160.1	-717.0	19980.7	19707.8	-201.1	149.5	1201.6
u2	29.6	-335.3	30986.8	30147.5	-331.3	250.3	1226.0
u3	533.1	213.8	44710.4	42586.8	-482.8	374.6	1484.9
u4	955.0	1500.3	78217.4	74462.9	-903.7	752.6	1450.3

The internal tides are generated due to the tide-topography interaction, and we want to know the conversion rate and how much energy radiates away from the

domain. Thus, the domain-integrated, depth-integrated and time-averaged energy budget of internal tides is calculated and shown in Table 4.2. The domain of the energy budget which contains the two ridges here is from -33 to 177 km except for Exp_dis1, Exp_dis2 and Exp_dis3: the domain for Exp_dis1 is about from 7 to 177 km, the domain for Exp_dis2 is from -73 to 177 km and the domain for Exp_dis3 is from -113 to 177 km. For Exp_K1, the results are averaged over 2 K1 tidal cycles after 1.4 K1 tidal cycles. The results from other experiments are averaged over 3 M2 tidal cycles after 3.6 M2 tidal cycles.

We can see in Table 4.2 that the domain-integrated, depth-integrated and time-averaged conversion rate is about 60 KW m^{-1} in the standard experiment. In contrast, the energy flux is about 57 KW m^{-1} and similar to the result (Qian et al., 2010). The tendency terms, the advection flux, and the dissipation are all small, compared with the conversion rate and the energy flux, thus the conversion rate is mainly balanced by the energy flux. The energy budget for Exp_K1 is just a reference, for the time we choose to do the calculations is not enough for K1 tide to reach a stable status. That is, the tendency terms ($\partial Pe/\partial t + \partial Ke/\partial t$) are large in Exp_K1, because the energy budget is still developing and not fully stable. However, the conversion rate for Exp_K1 is still mainly balanced by the energy flux.

The height of the west ridge decreases from 1600 to 700 m in Exp_west1, Exp_1, Exp_west2 and Exp_west3. The conversion rate decreases about from 66 to 51 KW m^{-1} and the energy flux decreases about from 61 to 49 KW m^{-1} in the four experiments. In addition, the tendency terms, the advection flux and the dissipation also change, as the height of the west ridge changes. To sum up, it is found that both the energy flux and the conversion rate increase, when the height of the west ridge increases.

The distance between the two ridges increases from 60 to 180 km in Exp_dis1, Exp_1, Exp_dis2 and Exp_dis3. The conversion rates calculated from Exp_dis1, Exp_1, Exp_dis2 and Exp_dis3 are 41, 60, 43 and 39 KW m^{-1} , respectively. The energy fluxes calculated from Exp_dis1, Exp_1, Exp_dis2 and Exp_dis3 are 39, 57, 42 and 33 KW m^{-1} , respectively. Comparing with the results from the four experiments, we find that when the distance between the two ridges is 100 km, the conversion rate and energy flux are the largest. Thus, the internal tides enhance when the distance between the two ridges is 100 km, and the reasons are discussed in detail in 4.5.2.

The amplitude of the barotropic tidal currents increases from 0.020 to 0.040 m s⁻¹ in Exp_u1, Exp_u2, Exp_u3, Exp_1 and Exp_u4. We can see that the conversion rate increases about from 20 to 78 KW m⁻¹ and the energy flux increases about from 19.7 to 74 KW m⁻¹ in the four experiments. Thus, the energy flux and the conversion rate become larger, when the amplitude of the barotropic tide becomes larger. The differences among the conversion rates from experiments with different amplitudes of the barotropic tide are much larger than those from experiments with different heights of the west ridge. It hints that the amplitude of the barotropic tide has a much larger influence on the generation of the internal tides, compared with the height of the west ridge.

4.4.3 Evolution of the energy budget

The time evolution of domain-integrated and depth-integrated energy budget of M2 internal tide for Exp_1 is shown in Fig. 4.3. We integrate the depth-integrated energy budget from -33 to 177 km and show the evolution of the domain-integrated budget over 3 M2 tidal cycles after 3.6 M2 tidal cycles. The conversion rate, $\partial PE/\partial t$ and $\partial KE/\partial t$ have a regular cycle as same as the M2 tidal force. The energy flux is larger than 0 for all the time, which means the energy always radiates away from the domain. The dissipation and advection flux parts are very small.

Fig. 4.4 shows the time evolution of domain-integrated, depth-integrated energy budget of K1 internal tide for Exp_K1. We integrate the depth-integrated energy budget from -33 to 177 km and show the evolution of the domain-integrated budget over 2 K1 cycles after 1.4 K1 tidal cycles. The conversion rate has a larger value with a period of time from 15 to 25 hour and the peak is about at 20 hour from the beginning. In addition, the conversion rate, $\partial PE/\partial t$ and $\partial KE/\partial t$ have a regular cycle as same as the K1 tidal force; the energy flux which radiates away from the domain is between 10 and 110 KW m⁻¹; the dissipation and advection flux parts are small, compared with other terms.

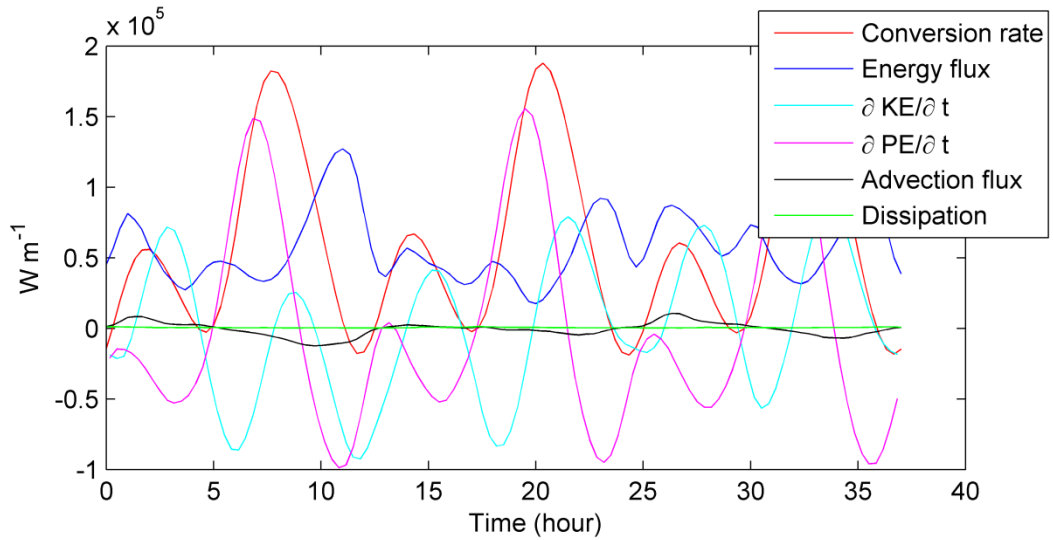


Figure 4.3. Evolution of the energy budget calculated from Exp_1.

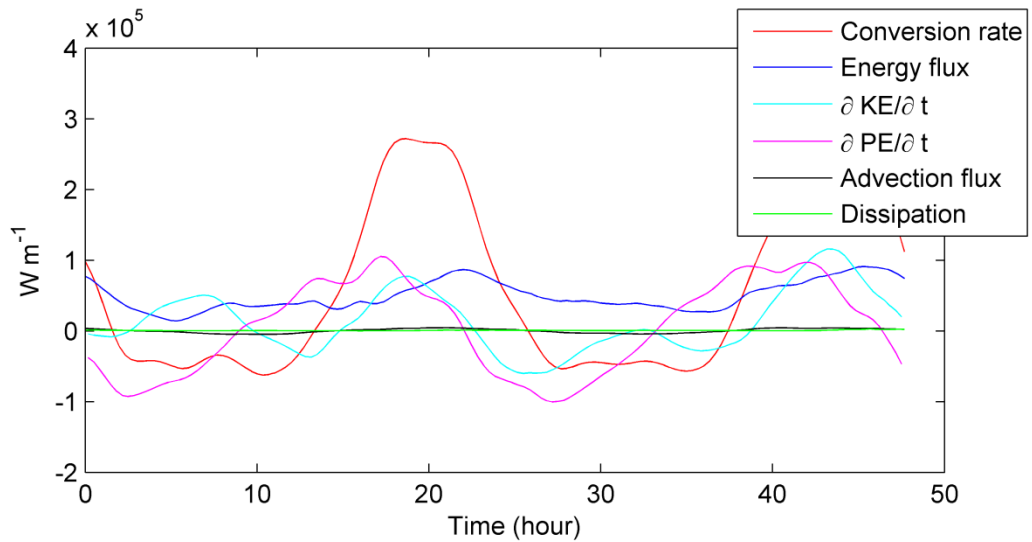


Figure 4.4. Evolution of the energy budget calculated from Exp_K1.

4.5 Sensitivity experiments

4.5.1 The height of the west ridge

Many factors have an influence on the generation of internal waves at the Luzon ridge, such as the east ridge and west ridge. Furthermore, the height of the west ridge, the shape and the width of the west ridge all have an influence on internal tides (Jan et al., 2012). As shown in Table 4.2, it is found that the energy flux and the conversion rate become larger, when the height of the west ridge increases. In this

section, the spatial distribution of the energy flux is shown and the influence of the height of the west ridge is investigated.

The depth-integrated and time-averaged energy flux is calculated, as shown in Fig. 4.5. The results are averaged over 3 M2 tidal cycles after 3.6 M2 tidal cycles. The negative energy flux means that the internal tide propagates westward and positive energy flux means that it propagates eastward. From Fig. 4.5, we can see that eastward energy fluxes at points from 177 to 600 km decrease with increasing distance from the point 177 km, and the westward energy fluxes at points from -33 to -600 km also decrease with increasing distance from the point -33 km. The internal solitary wave tails are generated at points from -270 to -580 km. The domain-integrated, depth-integrated and time-averaged energy flux can be got by subtracting the depth-integrated energy flux at -33 km from the depth-integrated energy flux at 177 km. When the height of the west ridge $H=1600$ m, the energy flux at 177 km is the largest and at the -33 km is the smallest as shown in Fig. 4.5. Thus, the domain-integrated, depth-integrated and time-averaged energy flux is largest for Exp_west1 among the four experiments. .

The solitary waves are usually generated on the west side of the two ridges from SAR (Liu et al., 2004; Zhao et al., 2004; Li et al., 2008). Fig. 4.6 shows the snapshots of baroclinic velocities after 5.9 tidal cycles calculated from the four experiments with different heights of the west ridge. The patterns of the baroclinic tides from the four experiments are quite similar. The solitary waves are generated on the west side of the topography, and there are no obvious solitary waves on the east side of the topography, which agree well with observations.

We not only show the horizontal distribution of the energy flux, but also study the vertical distribution of the energy flux. The time-averaged energy fluxes at three different points (Point A locates on the west side of the west ridge, Point B locates in the middle of the two ridges and Point C locates on the east side of the east ridge) are shown in Fig. 4.7. The results are averaged over 3 M2 tidal cycles after 3.6 M2 tidal cycles. We can see that the differences among the results calculated from the four experiments are large at Point A, but small at Point B and Point C. Thus, the increased energy flux due to the increased height of the west ridge main occurs from -1000 to -500 m at Point A.

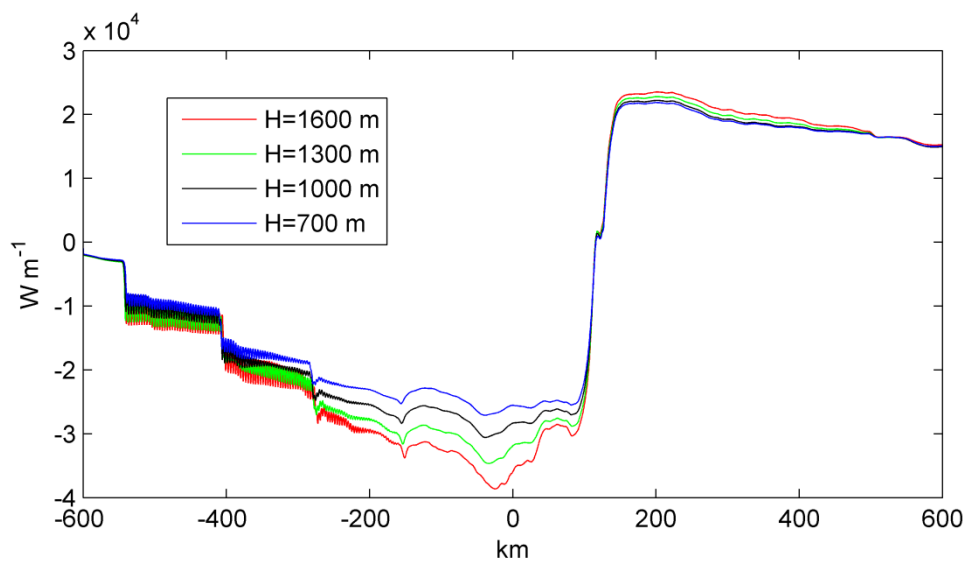


Figure 4.5. Depth-integrated and time-averaged energy fluxes for Exp_west1, Exp_1, Exp_west2 and Exp_west3. H represents the height of the west ridge.

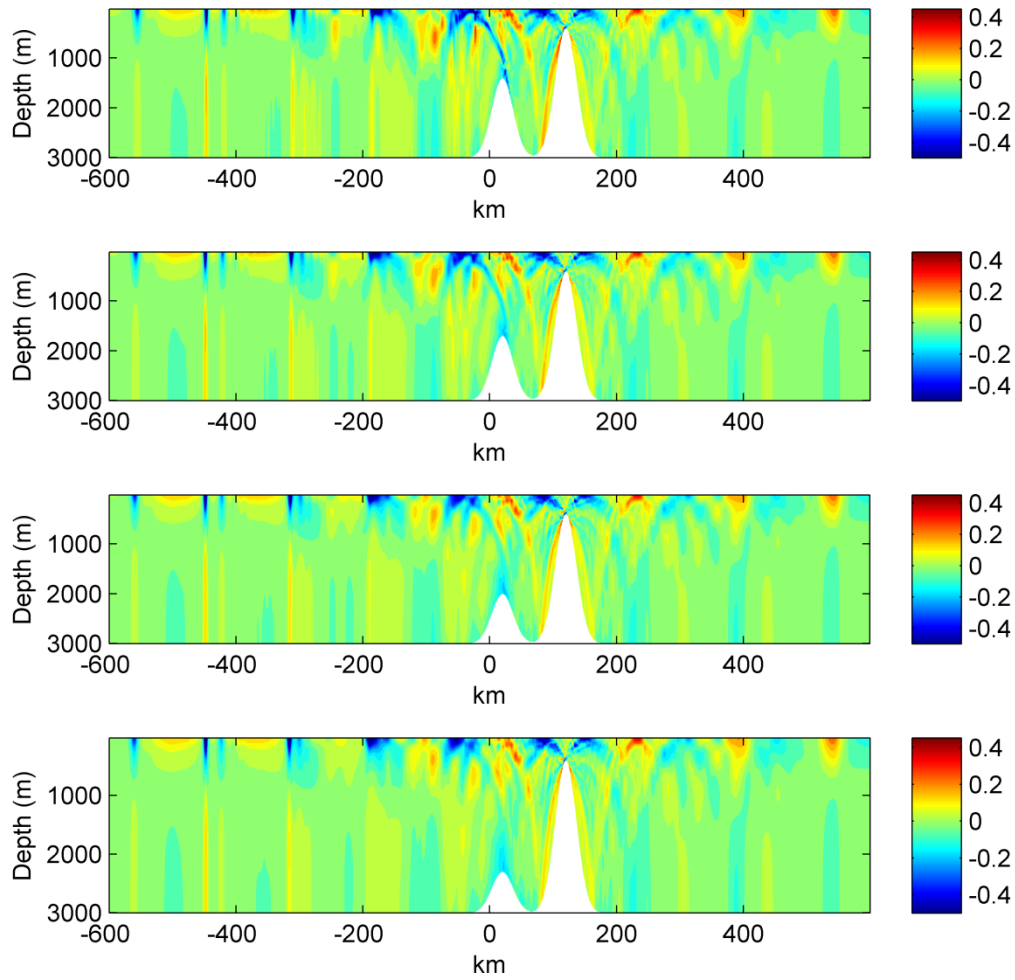


Figure 4.6. Snapshots of baroclinic velocity field (m s^{-1}) after 5.9 tidal cycles, from top to bottom, the height of the west ridge (a) $H=1600$ m, (b) $H=1300$ m, (c) $H=1000$ m, and (d) $H=700$ m.

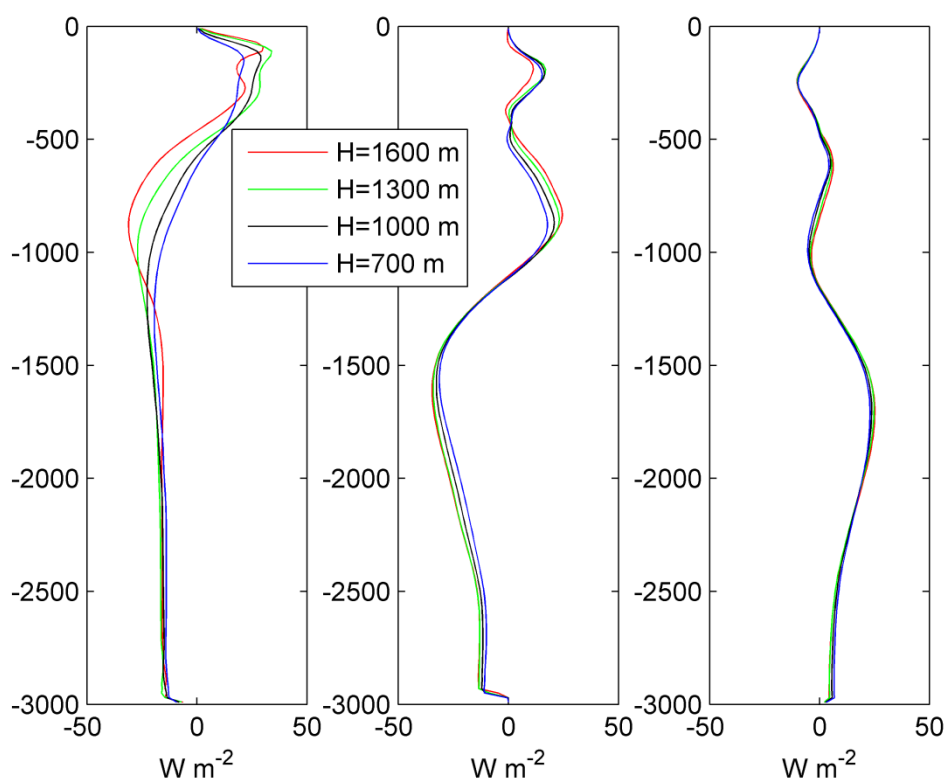


Figure 4.7. Time-averaged energy fluxes (from the left to the right) at Point A (-33 km), Point B (69 km), and Point C (177 km).

4.5.2 The distance between the two ridges

Besides the height of west ridge, the distance between the two ridges also has an influence on the generation of internal tides. Depth-integrated and time-averaged conversion rates calculated from the four experiments with different distances between the two ridges are shown in Fig. 4.8. It is found that the conversion rates are large at the two ridges. In addition, the conversion rates from the four experiments are almost the same at points from 120 to 200 km, but different at the points from -100 to 120 km due to different topographies. Furthermore, when the distance between the two ridges is 100 km (represented by green line), the domain-integrated conversion rate is larger than the conversion rates calculated from the other three experiments.

Fig. 4.9 shows depth-integrated and time-averaged energy fluxes calculated from Exp_dis1, Exp_1, Exp_dis2 and Exp_dis3. The energy fluxes at points from 177 to

600 km are almost the same. However, when the distance is 100 km, the westward fluxes at points from -33 to -600 km are the largest and the internal solitary waves are generated. In contrast, there are no obvious internal solitary waves generated in the other three experiments. Jan et al. (2012) also studied the influence of the distance on the energy flux. In their research, the energy flux decreases with the increased distance between two ridges. But in their research, the distance is 90%-110% of the distance used in the reference experiment. The reason why the results from Jan et al. (2012) and this paper are not the same is that the differences between the distances used in their paper are much smaller than the differences between the distances used in our designed experiments.

Fig. 4.10 shows the baroclinic velocities calculated from the four experiments. The length of the mode 1 internal tides is about 100 km. When the distance is 100 km, the beam radiates from the top of the east ridge to the top of the west ridge and the internal tides are enhanced, then the internal solitary waves are generated about at -290 km. In contrast, the solitary wave tails are not generated in the other three experiments. The isotherms for Exp_dis1, Exp_1 and Exp_dis2 are shown in Fig. 4.11. The red, black and blue lines represent the isotherms when dis = 60, 100 and 140 km, respectively. Through the isotherms in Fig. 4.11, we can determine that whether there are solitary waves generated or not. The internal solitary wave tails can only be seen through the black line which represents the results from Exp_1 in which the distance between the two ridges is 100 km. Furthermore, it indicates that the internal tides are enhanced, when the distance between the two ridges is 100 km, which is consistent with the conclusion from Fig. 4.10.

In summary, according to Jan et al. (2012), the internal tides generated are proved to be enhanced due to the existence of the west ridge through experiments with changing the heights of the ridge, the shapes of the ridge, the width of the ridge and the distances between the two ridge. Furthermore, here it shows that the conversion rate and energy flux are the largest, when the distance between the two ridges is 100 km.

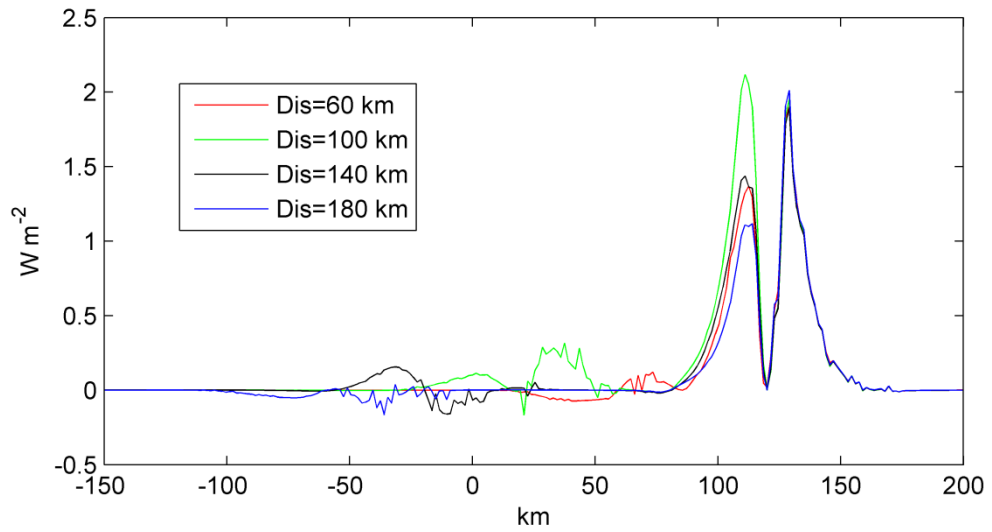


Figure 4.8. The depth-integrated and time-averaged conversion rates for Exp_dis1, Exp_1, Exp_dis2, and Exp_dis3.

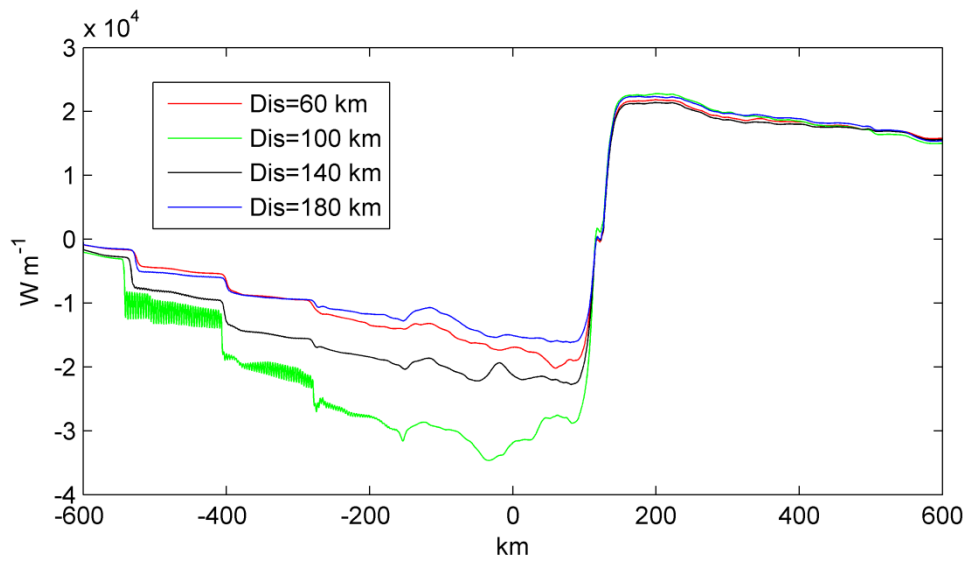


Figure 4.9. Depth-integrated and time-averaged energy fluxes for Exp_dis1, Exp_1, Exp_dis2, and Exp_dis3.

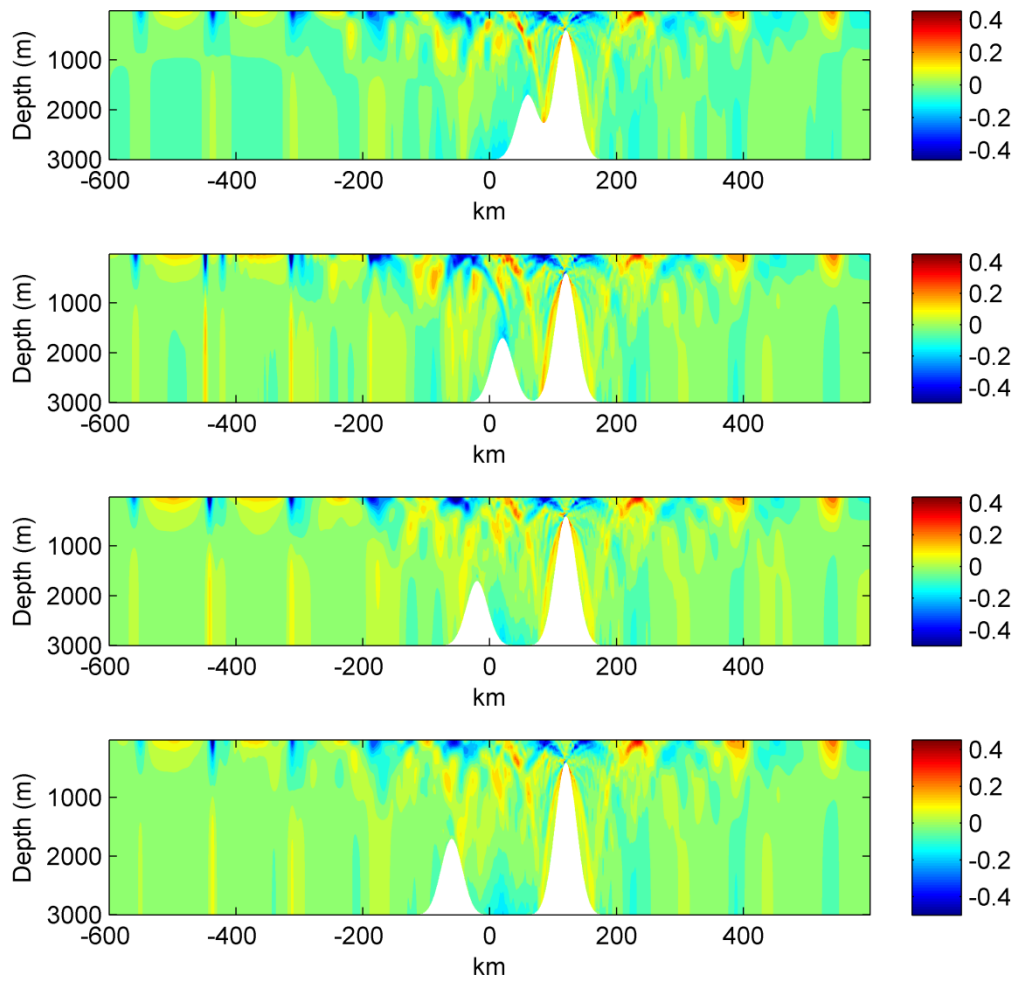


Figure 4.10. Snapshots of baroclinic velocity field (m s^{-1}) after 5.9 tidal cycles, from top to bottom, the distance between the two ridges (a) Dis=60 km, (b) Dis=100 km, (c) Dis=140 km, and (d) Dis=180 km.

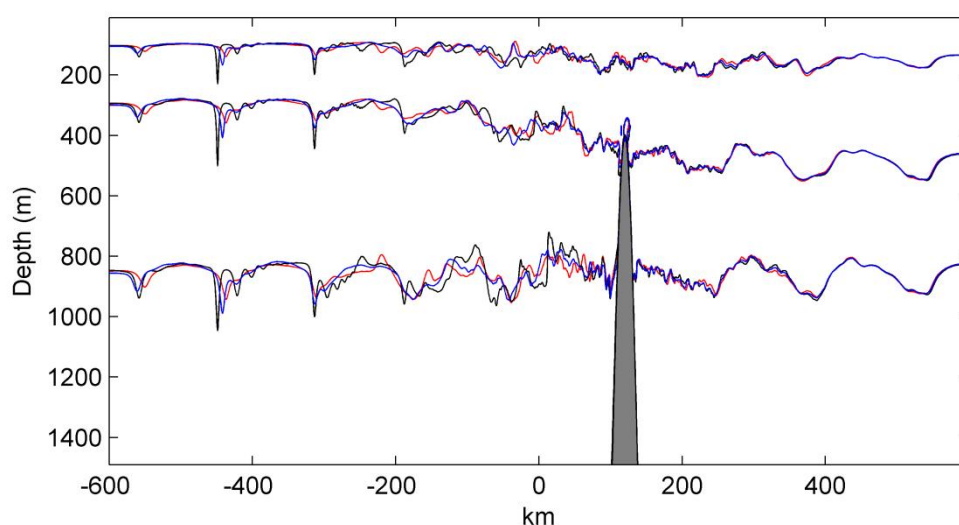


Figure 4.11. Snapshot of temperature field after 5.9 tidal cycles, and the temperatures are 5 °C (bottom line), 10 °C (middle line) and 20 °C (top line). The red, black and blue lines represent the isotherms when $dis = 60, 100$ and 140 km, respectively. The isotherm displacements are increased in magnitude by a factor of 2.

4.5.3 The amplitude of the barotropic tide

The amplitude of the barotropic tide is one of the crucial factors for the generation of internal tides. In terms of the linear theory, the energy flux is appropriate to the square of the amplitude of the barotropic tide which has been shown in Chapter 3. But the results from Chapter 3 are based on an ideal isolated topography and uniform stratification. Here, the stratification is non-uniform. Fig. 4.12 shows the depth-integrated and time-averaged energy fluxes (scaled by the square of the amplitude of the barotropic tide) calculated from the five experiments with different amplitudes of the barotropic tide. The results from the five experiments are almost the same from -50 to 400 km. This means that the energy flux is appropriate to the square of the amplitude of the barotropic tide, which is consistent with the linear theory. The scaled energy fluxes are the same in most area, but differ in small aspects. For example, the amplitudes of the tails of the energy fluxes are larger, when the amplitude of the barotropic tide is larger. It indicates that when the amplitude of the barotropic tide is larger, the amplitudes of the solitary waves generated will be larger.

Fig. 4.13 shows the snapshots of baroclinic velocities (m s^{-1}) after 5.9 tidal cycles. We can see that when $u=0.020 \text{ m s}^{-1}$ and $u=0.025 \text{ m s}^{-1}$, the generated baroclinic velocities are small and there are no internal solitary wave tails. When $u=0.030 \text{ m s}^{-1}$ and $u=0.035 \text{ m s}^{-1}$, the internal solitary wave tails are generated. When $u=0.040 \text{ m s}^{-1}$, the amplitudes of the internal solitary wave tails are the largest. Thus the amplitude of the barotropic tide is one crucial factor on the generation of internal solitary waves. At the Luzon ridge, generally the M2 barotropic tide $u=0.035 \text{ m s}^{-1}$, therefore there will be internal solitary waves generated by M2 tide. To sum up, results show that when the amplitude of barotropic tide is large enough, there will be trains of internal solitary wave generateds, which is consistent with Cai et al. (2002).

The isotherms for Exp_u1, Exp_u3 and Exp_u4 are shown in Fig. 4.14. The red, balck and blue lines represent the isotherms when $u=0.020$, 0.030 and 0.040 m s^{-1} , respectively. As suggested in Fig. 4.13, Fig. 4.14 also shows that the solitary wave tails are generated when $u= 0.030 \text{ m s}^{-1}$ and $u=0.040 \text{ m s}^{-1}$. In addition, the solitary waves in Exp_u4 have propagated further than those in Exp_u3 within the same time, indicating that the speeds of the internal solitary waves are larger in Exp_u4 than one in Exp_u3. Hence, the amplitude of the barotropic tide not only has an influence on the generation of the solitary waves but also on the speeds of the solitary waves. The speeds of the internal solitary waves will be larger, when the amplitude of the barotropic tide increases.

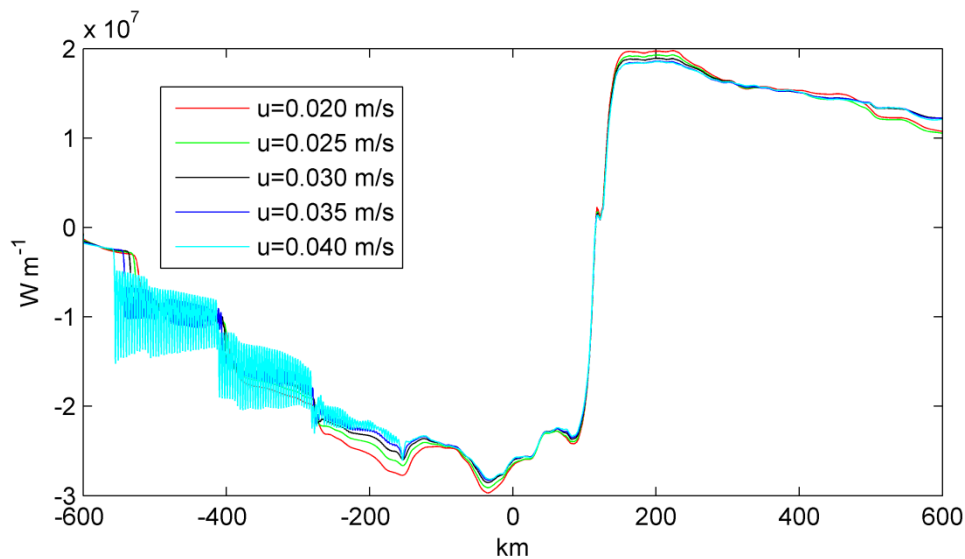


Figure 4.12. Depth-integrated and time-averaged energy fluxes for Exp_u1, Exp_u2, Exp_u3, Exp_u4.

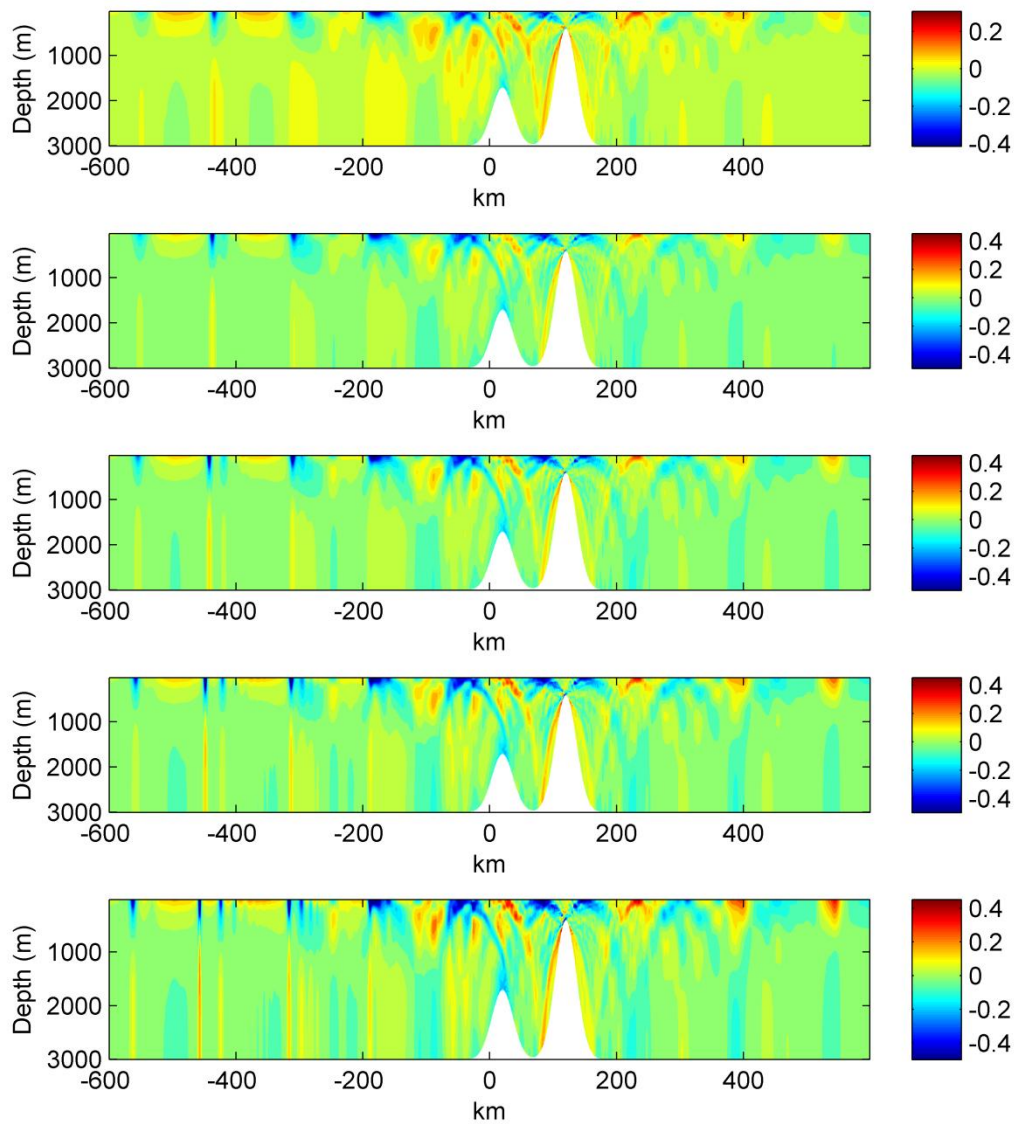


Figure 4.13. Snapshots of baroclinic velocity field (m s^{-1}) after 5.9 tidal cycles, from top to bottom, (a) $u=0.020 \text{ m s}^{-1}$, (b) $u=0.025 \text{ m s}^{-1}$, (c) $u=0.030 \text{ m s}^{-1}$, (d) $u=0.035 \text{ m s}^{-1}$, and (e) $u=0.040 \text{ m s}^{-1}$.

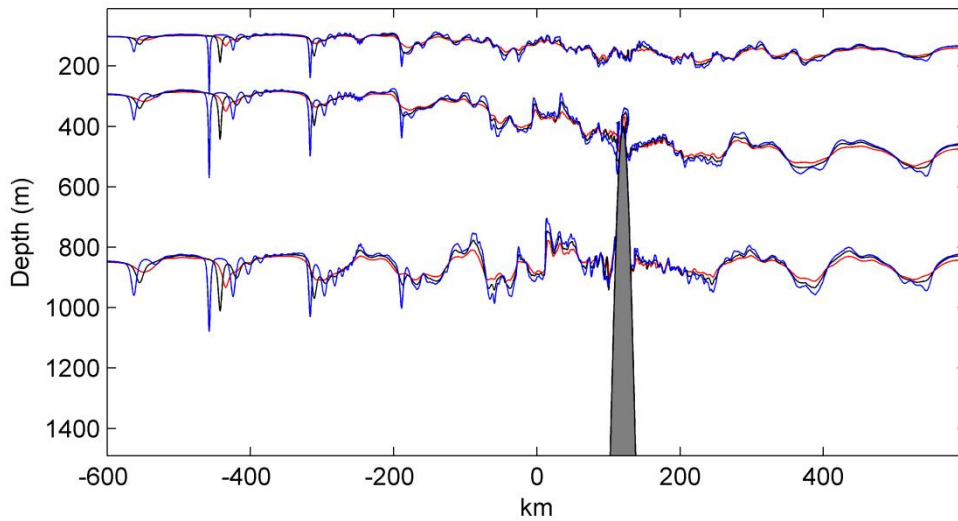


Figure 4.14. Snapshot of temperature field after 5.9 tidal cycles, and the temperatures are 5 °C (bottom line), 10 °C (middle line) and 20 °C (top line). The red, black and blue lines represent the isotherms when $u=0.020$, 0.030 and 0.040 m s^{-1} , respectively. The isotherm displacements are increased in magnitude by a factor of 2.

4.6 Conclusion

In this chapter, two-dimensional simulations of internal waves at the Luzon ridge are studied. The realistic stratification and Gaussian Ridge topography are used. The generated baroclinic velocities mainly occur at their fundamental frequency. The baroclinic energy budget shows that the domain-integrated, depth-integrated and time-averaged conversion rate is about 60 KW m^{-1} and the energy flux is about 57 KW m^{-1} in the standard experiment. The tendency terms, the advection flux, and the dissipation are all small, compared with the conversion rate and the energy flux, and the conversion rate is mainly balanced by the energy flux.

The influences of the height of the west ridge, the distance between the two ridges and the amplitude of the barotropic tide suggested in the former research (Cai et al., 2002; Buijsamn et al., 2010b; Jan et al., 2012) on the generation of internal waves are studied. Model results show that all the above factors have an obvious influence on the generation of internal waves in different aspects.

Firstly, the results show that as the height of the west ridge increases, the

conversion rate and the energy flux become larger. The increased energy flux mainly occurs from -1000 to -500 m around the west side of the west ridge. Secondly, the internal tides are enhanced due to a suitable distance between two ridges. When the distance between the two ridges is 100 km, the energy flux and the conversion rate are the largest. This is also a reason why the westward solitons are larger than eastward solutions. Thirdly, model results show that the energy flux is appropriate to the square of the amplitude of the barotropic tide. The amplitude of the barotropic tide not only has an influence on the generation of the internal solitary waves but also on the speeds of the internal solitary waves. When the amplitude of barotropic tide is larger, the speeds of the generated internal solitary waves will be larger.

Chapter 5

5 The energetics of internal tides at the Luzon ridge

Abstract

The three-dimensional simulations of the M2 and K1 internal tides using MITgcm at the Luzon ridge are presented in the paper. Not only the full barotropic and baroclinic energy budgets but also the barotropic and baroclinic kinetic energy budgets are analyzed. The results of the full energy budgets for M2 tide show that about 15.1 GW is transferred from the M2 barotropic tide to M2 baroclinic tide, which is about 88% of the barotropic input. The baroclinic energy flux is about 4.5 GW, and the total dissipation is about 11.3 GW. Additionally, it is found that the potential energy budget and nonlinear terms play a very small role in the full energy budget. The sensitivity of the results to the resolution and stratification is also investigated. When the grid spacing is coarser, the difference between the conversion rate in the baroclinic kinetic energy equation and the conversion rate in the barotropic kinetic energy equation is larger. The differences between the results from different stratifications indicate that the stratification makes a contribution to the seasonal variations of the conversion of the M2 tide. The formula (Nycander, 2005) may underestimate the conversion rate at the Luzon ridge because of using bottom stratification N_b in the calculation, compared with the model results.

5.1 Introduction

The internal tide can be generated by barotropic flow over bottom topography in stratified ocean. The energy from the barotropic tide will be either converted to the baroclinic tide or dissipated in oceanic regions. Furthermore, most of the energy will sink in marginal seas, and the rest of the energy about 1 TW estimated from TOPEX/Poseidon altimetric data is lost in the deep ocean (Egbert and Ray, 2001), which is one of the most important source to the interior mixing (Munk and Wunsch, 1998).

The dissipation of barotropic tides calculated from altimetric data (Egbert and Ray, 2001) refers to the lost energy of barotropic tides and it can't distinguish the difference between the conversion rate from barotropic tides to baroclinic tides and the dissipation of barotropic and baroclinic tides. Recently, the conversion rate of the tide has been studied in the linear theory (Balmforth et al., 2002; St. Laurent and Garrent, 2002; Llewellyn Smith and Young, 2002; Khatiwala, 2003). The conversion rates defined in the above papers refer to either the conversion rate transferred from barotropic flow to baroclinic flow or the baroclinic energy flux generated by barotropic flow over bottom topography, which are equal to each other in theory when the flow is assumed to be inviscid. Moreover, some studies have compared the results predicted by the linear theory with the model results (Di Lorenzo et al., 2006; Zaron and Egbert, 2006; Legg and Huijts, 2006).

Nycander (2005) derived a formula for the conversion rate based on the linear theory (Bell, 1975a, b; Llewellyn Smith and Young, 2002) and calculated the global conversion rate of tides using the tidal data from TPXO 6 model. The results (Nycander, 2005) showed that the global energy flux was about 1.2 TW at depths greater than 500 m, which compared well with the results calculated by Egbert and Ray (2001). However, both above calculations of global tidal dissipation are using a coarse resolution. The strong tides may occur in regions such as Luzon ridge, in which the calculations in a coarse resolution are not reliable and simulations in a higher resolution are needed.

Internal tide energy flux has been studied in numerical simulations in much research. Merrifield and Holloway (2002) used POM to simulate the M2 internal tide at the Hawaiian ridge. They showed that the radiated energy flux at these sites was 9.7 GW. Jachec et al. (2006) used SUNTANS model to simulate the internal tides in Monterey. The energy flux within the computational domain was 53 MW. The research on the energetics of internal tides using different models and focusing on different areas can also be found in the following papers. Buijsman et al. (2012b) used ROMS in the Southern California Bight. Tanaka et al. (2013) used MITgcm in the southeastern Bering Sea. Green et al. (2008) used 2-d MITgcm at the European shelf edge.

Above studies except Tanaka et al. (2013) mainly focused on the energy flux part. Moreover, several studies have derived the energy budgets from Navier-Stokes equations. The barotropic and baroclinic kinetic energy equations based on the linear

theory were studied in the Zaron and Egbert (2006). Then, Ponte and Cornuelle (2013) used MITgcm to study the kinetic energy budgets around Point Loma in San Diego, California. The full barotropic and baroclinic energy equations from POM were derived by Cater et al. (2008) and applied at the Hawaii Islands. Kang and Fringer (2012) derived barotropic and baroclinic energy equations including the potential energy parts based on Navier-Stokes equations in a different way and applied the theory in the Monterey Bay area. Through this method of derivation of the equations, one can easily distinguish the barotropic input, the conversion rate and the energy flux parts. The baroclinic energy equation (Kang and Fringer, 2012) has also been used in the research (Buijsman et al., 2012a; Jalali et al., 2014), but Buijsman et al. (2012a) calculated the conversion rate using $\bar{C} = \int p'(x, -H, t) W dx$, where p' is the perturbation pressure and W is the barotropic velocity. Furthermore, Jalali et al. (2014) added turbulent production terms to the baroclinic energy equation.

The Luzon strait connects the South China Sea to the west Pacific Ocean and features two meridional ridges. Strong diurnal and semidiurnal internal tides are generated, when the barotropic tides flow over bottom topography. Then, part of the internal tides will dissipate locally. Part of the internal tides will either propagate into Pacific Ocean or into the South China Sea. Internal tides may evolve into solitary waves in the northern of South China Sea. The conversion rate and energy flux of tides have been studied in numerical simulations and using satellite data. Niwa and Hibiya (2004) used Princeton Ocean Model in the East China Sea. Their results showed that the conversion rate of the M2 tide was 14.9 GW, the energy flux was 9.0 GW, and the dissipation was 5.9 GW in the standard experiment. Jan et al. (2008) used Princeton Ocean Model study the M2 baroclinic tide in Luzon strait. They showed that about the 18 GW barotropic tide was lost: the conversion rate was 10 GW and the barotropic tides dissipation was 8 GW. Buijsman et al. (2014) used MITgcm to simulate the internal tides at the Luzon ridge. They divided the tides into diurnal and semidiurnal parts. The internal tide resonance, conversion rate, energy flux divergence and dissipation based on the kinetic and available potential energy equation derived by Kelly et al. (2012) were studied. Zhao (2014) used the sea surface height measurements and found that the energy flux of Mode-1 M2 tide was about 2.7 GW. Kerry et al. (2014) used ROMS to study the conversion rate from barotropic tide to baroclinic tide in the Philippine Sea. At the Luzon strait, the

conversion rate was 16.02 GW. However, they haven't calculated the full energy budgets here.

In this paper, we use three-dimensional MITgcm to study the M2 and K1 internal tides and mainly focus on the energy budgets (the full barotropic and baroclinic energy budgets, and the barotropic and baroclinic kinetic energy budget). Several experiments with different stratifications and resolutions are carried out to examine the influence of the factors on the properties of the internal tides. We also want to compare our model results with the values predicted by the theory (Nycander, 2005) at the Luzon ridge, since the theory is usually used in a coarse resolution for the global calculations. The paper is organized as follows: in section 5.2, the model configuration is described; in section 5.3, the baroclinic velocity and tide ellipses are shown; in section 5.4, the results of two kinds of energy budgets (the full barotropic and baroclinic energy budgets, and the barotropic and baroclinic kinetic energy budgets) are analyzed; in section 5.5, the energy budgets of K1 internal tide are discussed; in section 5.6, the conversion rates calculated using the method of Green and Nycander (2013) are shown. The discussion and conclusion parts are shown in section 5.7 and section 5.8.

5.2 Model

The MITgcm (Marshall et al., 1997) is used for the three-dimensional internal tides simulation in this study. The nonhydrostatic simulation is used in much research on the internal waves (Kang and Fringer, 2010; Rapaka et al., 2013; Jalali et al., 2014).

Strong internal tides are generated at the Luzon ridge for its special topographic features (two north-south ridges) and its location (it connects the Pacific Sea and the Northern portion of the South China Sea). When the barotropic tides propagate from the Pacific Sea to the South China Sea, the baroclinic tides are generated here due to the tide-topography interaction. In the paper, the domain of the simulation extends over $118^{\circ}\text{E} - 124^{\circ}\text{E}$ and $17.95^{\circ}\text{N} - 23^{\circ}\text{N}$ and cover the two meridional ridges, as shown in Fig. 5.1. The horizontal resolution of the domain in standard experiments (Exp_Ref and Exp_K1) is $1/60^{\circ}$ both in the longitudinal and latitudinal directions. There are 58 vertical layers in the model: the top 400 m has a resolution of 20 m and the grid spacing increases up to 500 m at the maximum depth $z = -6400$ m. The total

calculation grid is $360 \times 304 \times 58$.

The model use realistic topography from the Smith and Sandwell v9.1 (Smith and Sandwell, 1997) with a resolution of $1/60^\circ$. The background stratification is horizontally uniform and only a linear function of temperature. The stratification is obtained as follows: firstly, we obtain the salinity and temperature averaged over the whole domain from WOCE Hydrographic Climatology (Gouretski and Koltermann, 2004); secondly, we calculate the buoyancy frequency; at last, we use a linear relation to transfer from the buoyancy frequency to the temperature field and interpolate these data onto the model points. The temperature and buoyancy frequency used in the model are shown in Fig. 5.2. The other two experiments (Exp_Summer and Exp_Winter) with stratification calculated from SODA 2.24 forced by the M2 barotropic tide are used to examine the effect of the stratification on the energy budgets. The buoyancy frequencies calculated from SODA in winter and summer are larger than the one calculated from WOCE at depth deeper than -3500m, and the stratification in winter (SODA) is weaker than the one in summer (SODA) in the upper 200 m, as shown in Fig. 5.2.

The background horizontal and vertical viscosity and diffusivity are $10^{-1} \text{ m}^2 \text{ s}^{-1}$ and $10^{-5} \text{ m}^2 \text{ s}^{-1}$, respectively. The Kpp scheme (Large et al., 1994) and advection temperature scheme 33 are used for all the simulations. The quadratic bottom drag is 0.0025, which is the same with the past research (Niwa and Hibiya, 2004; Tanaka et al., 2013; Buijsman et al., 2014).

The model is forced at the four boundaries. The amplitudes and phases of M2 and K1 barotropic tide are extracted from TPXO7.2 inverse model (Egbert et al., 1994). In order to study the influence of the resolution on the energy budgets, two other experiments (Exp_reso1 and Exp_reso2) forced by M2 barotropic tide with different resolutions are added. The horizontal resolution of Exp_reso1 is $1/30^\circ \times 1/30^\circ$ and the horizontal resolution of Exp_reso2 is $1/30^\circ \times 1/30^\circ$. A sponge layer is set at the four boundaries to minimize the reflection of energy. The sponge layer is imposed over 20 cells from the boundaries in standard experiment, and 10 cells in Exp_reso1 and Exp_reso2. A time-invariant temperature profile is set at the boundaries. The experiments are run for 20 M2 tidal cycles for M2 and 18 K1 tidal cycles for K1 from 1 July 2008.

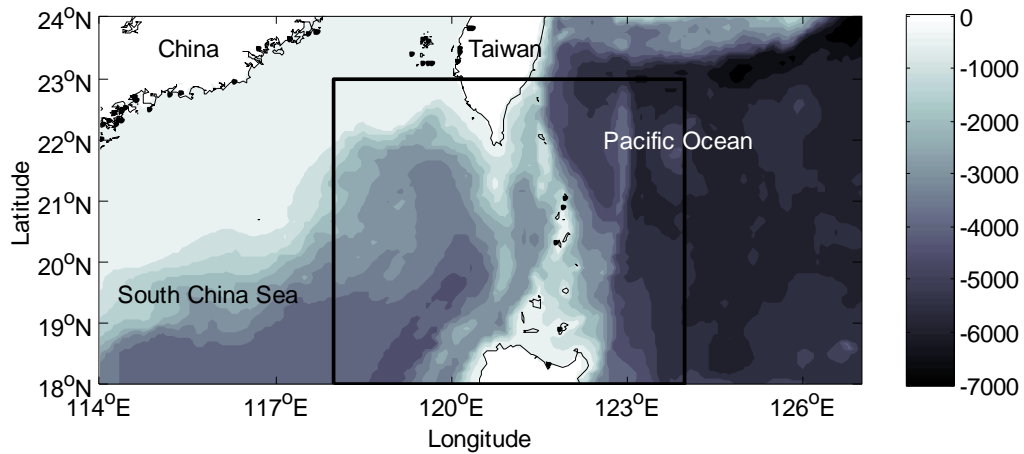


Figure 5.1. Map showing the bathymetry. The small black box shows the domain of the model.

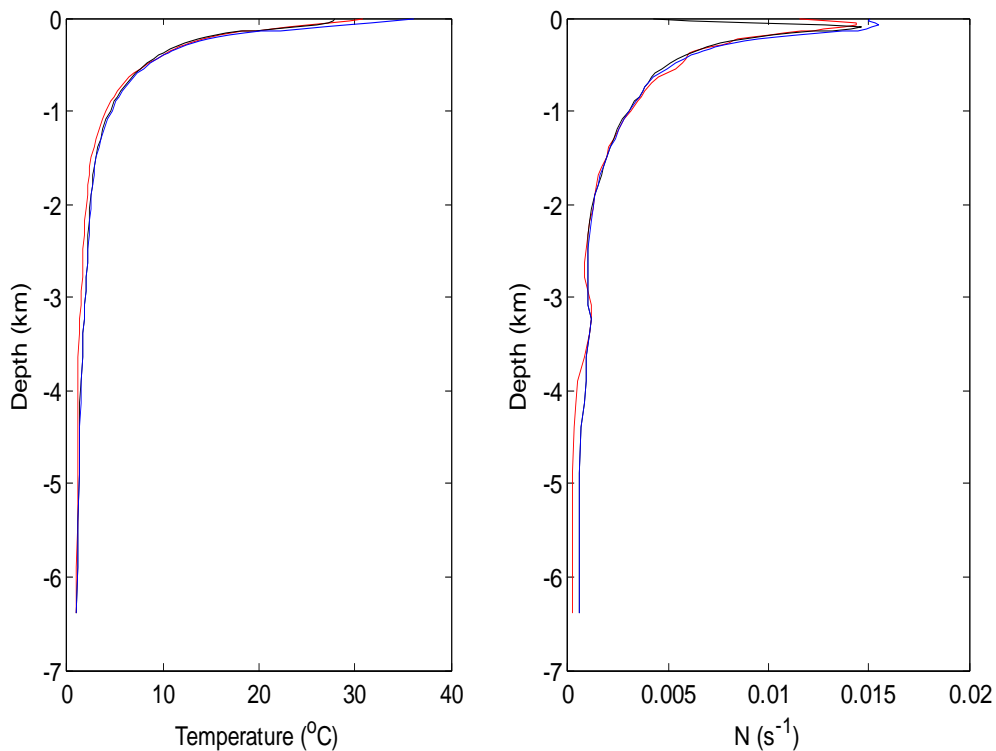


Figure 5.2. The temperature (left) and buoyancy (right) used in models: red lines represent the temperature and buoyancy calculated from WOCE Hydrographic Climatology in standard experiments; blue lines represent the temperature and buoyancy calculated from SODA v2.24 monthly data (7, 2008) used in Exp_Summer; black lines represent the temperature and buoyancy calculated from SODA v2.24 monthly data (1, 2008) in Exp_Winter.

5.3 Model validation

5.3.1 The M2 baroclinic velocity

The baroclinic velocities calculated from Exp_Ref, Exp_Summer and Exp_Winter, are shown in Fig. 5.3a), b) and c), respectively. The patterns of the baroclinic velocities calculated from experiments with different stratifications are quite similar: the internal wave beams radiate from the bottom topography and the amplitude of the baroclinic tide can reach 0.8 m s^{-1} . The internal wave beams are controlled by linear internal wave dispersion relation, and the slope of internal wave beam $s = \frac{\sqrt{\omega^2 - f^2}}{\sqrt{N^2 - \omega^2}}$, where s is the slope of internal wave beam, ω is the M2 frequency, f is the Coriolis frequency and $N(z)$ is the stratification. Thus we can see that the internal waves generated here are mainly linear.

Internal solitary waves may generate in the Northern portion of the South China Sea when strong internal tides steepen by nonlinear effects (Buijsman et al., 2010b; Zhang et al., 2011). The existence of the solitary waves has been verified basing on Satellite images (Li et al., 2008) and by observation (Duda et al., 2004; Alford et al., 2010). But here, the resolution of our model is too coarse to get the features of the internal solitary waves, for the typical wave length of the wave is about 1-2 km.

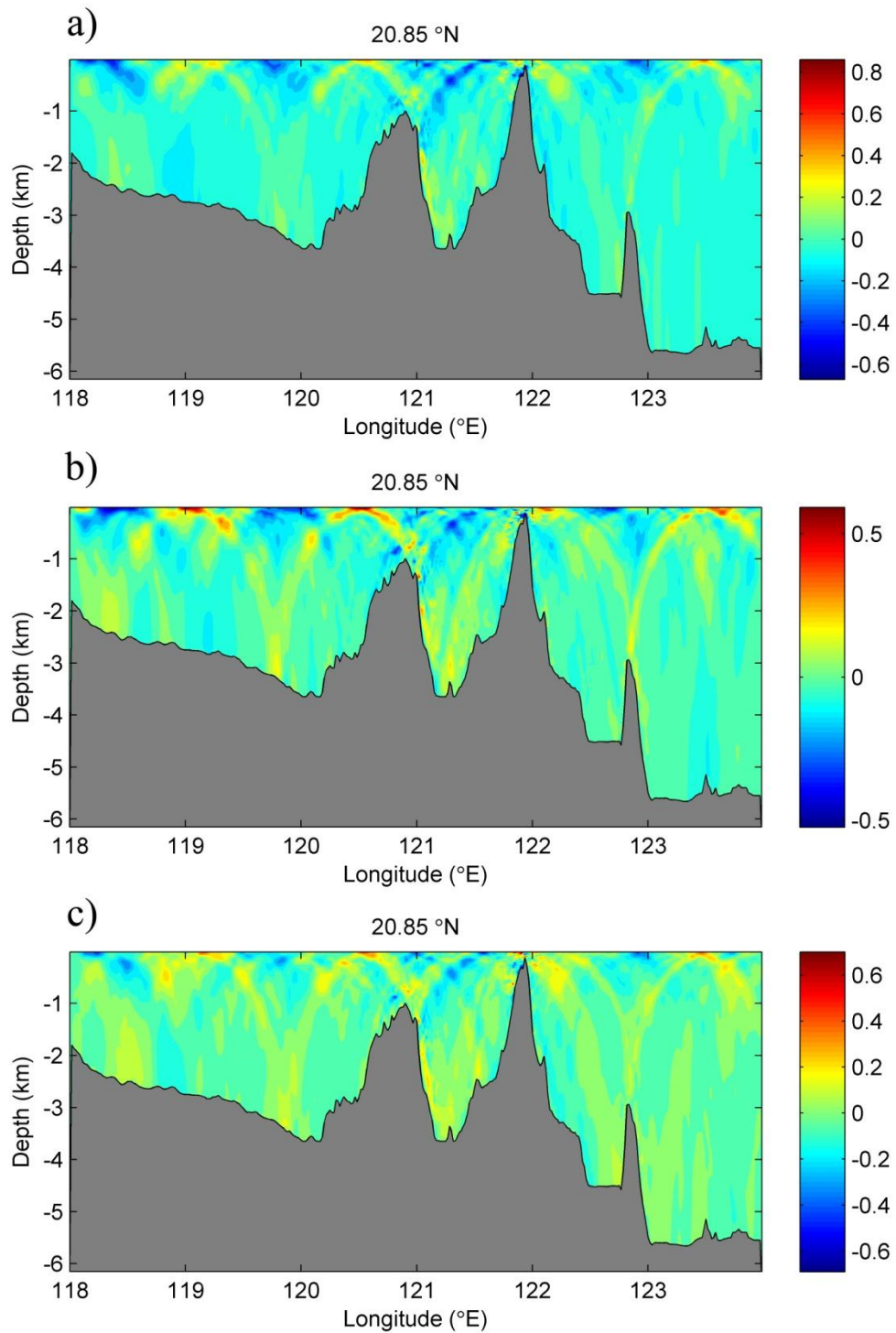


Figure 5.3. Snapshots of baroclinic velocity (m s^{-1}) along 20.85°N after 10 M2 tidal cycles: a), b) and c) represent the baroclinic velocity calculated from Exp_Ref, Exp_Summer and Exp_Winter, respectively.

5.3.2 The M2 tidal ellipses

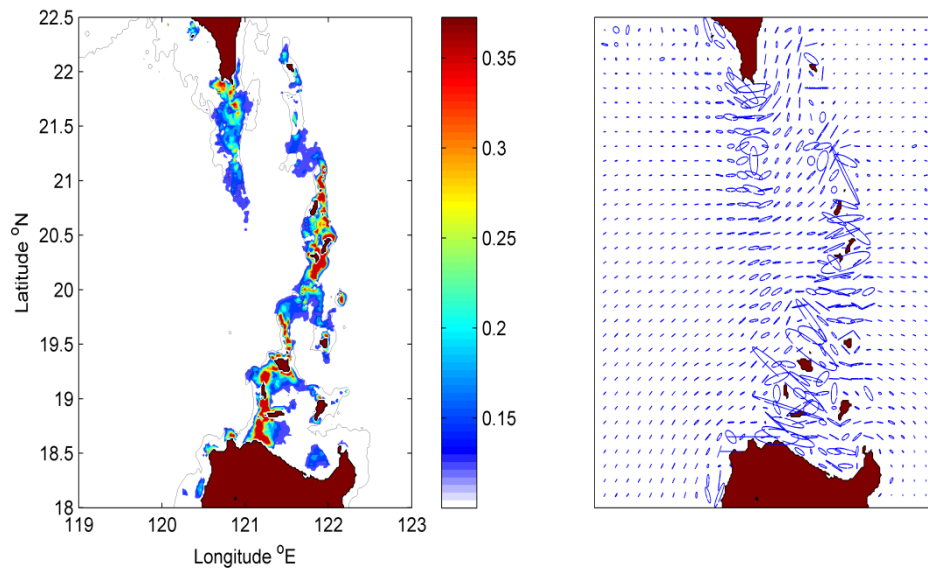


Figure 5.4. Left: the major axis amplitude of the M2 barotropic tidal ellipses. Right: the M2 barotropic tidal ellipses. Bathymetry contour is -1000 m.

Fig. 5.4 shows the major axis amplitude of the M2 barotropic tidal ellipses and the tidal ellipses. The tidal amplitudes and phases used in the tidal ellipses are calculated based on the barotropic tide currents (U , V) which are got over three tidal cycles beginning from the sixteenth M2 tidal cycle. The major axis amplitude is large along the double-ridge, especially in the northern portion of the west ridge and the middle and southern portions of the east ridge. Most of the orientations of the tidal ellipses are shown to turn towards the mouth of the Luzon Strait except the ones influenced by local topography around the two meridional ridges. The maximum velocity can reach $U_{\max} = 0.38 \text{ m s}^{-1}$. The pattern of the tidal ellipses is quite similar to the results (Buijsman et al., 2014), except that it shows relatively larger values in their paper, because the semidiurnal tidal ellipses in their paper include all semidiurnal components.

5.4 The energy budgets

5.4.1 The barotropic and baroclinic energy equations

5.4.1.1 Theory

Here we follow the energy budgets derived by Kang and Fringer (2012). In order to obtain the barotropic and baroclinic energy equations, the velocity is divided into barotropic and baroclinic parts. The full velocity $\mathbf{u}=(u, v, w)$, and the barotropic velocity $\mathbf{U}=(U, V, W)$. The baroclinic velocity is defined by

$$\mathbf{u}'(x, y, z, t) = \mathbf{u}(x, y, z, t) - \mathbf{U}(x, y, z, t), \quad (5.1)$$

where the horizontal barotropic velocities can be obtained by

$$\mathbf{U}_h = \frac{1}{\eta+h} \int_{-h}^{\eta} \mathbf{u}_h(x, y, z, t) dz, \quad (5.2)$$

where η is the free surface elevation, h is the depth of ocean, $\mathbf{u}_h=(u, v)$ and $\mathbf{U}_h=(U, V)$. The continuity equation for (U, V, W) gives

$$\frac{\partial U}{\partial x} + \frac{\partial V}{\partial y} + \frac{\partial W}{\partial z} = 0. \quad (5.3)$$

The boundary condition on the bottom is

$$-\mathbf{U}_h \cdot \nabla_H h = W, \quad \text{when } z = -d. \quad (5.4)$$

Combining (5.3) and (5.4), the vertical barotropic velocity can be obtained by

$$W(z) = -\nabla_H \cdot ((z+h)\mathbf{U}_h). \quad (5.5)$$

The total density is

$$\rho(x, y, z, t) = \rho_0 + \rho_v(z) + \rho'(x, y, z, t), \quad (5.6)$$

where ρ_0 is the constant reference density, ρ_v is the background density and ρ' is the perturbation density. The total pressure is given by

$$\begin{aligned} p(x, y, z, t) &= p_0 + p_v(z) + p'(x, y, z, t) + q, \\ &= \rho_0 g(\eta - z) + g \int_z^{\eta} \rho_v dz + g \int_z^{\eta} \rho' dz + q, \end{aligned} \quad (5.7)$$

where p_0 is the reference pressure, $p_v(z)$ is the background pressure, and q is the nonhydrostatic pressure. Decomposition goes a series of processes, and we can obtain the barotropic and baroclinic equations. The depth-integrated barotropic equation reads

$$\frac{\partial}{\partial t} (\overline{E_{kb}} + \overline{E_{pb}}) + \nabla_H \cdot \overline{\mathbf{F}_b} = -\overline{C} - \overline{\varepsilon_b} - \overline{R_{b1}}, \quad (5.8)$$

where the overbar indicates depth-integrated and the barotropic kinetic energy is

$$E_{kb} = \frac{1}{2}\rho_0(U^2 + V^2), \quad (5.9)$$

the depth-integrated potential energy due to surface elevation is

$$\overline{E_{pb}} = \frac{1}{2}\rho_0g\eta^2, \quad (5.10)$$

the depth-integrated barotropic energy flux is

$$\overline{\mathbf{F}_b} = \mathbf{U}_h\overline{E_{kb}} + \mathbf{U}_hH\rho_0g\eta + \mathbf{U}_h\overline{p'} + \mathbf{U}_h\overline{q} - \overline{A_h\nabla_H E_{kb}}, \quad (5.11)$$

where $\mathbf{U}_h\overline{E_{kb}}$ is the barotropic advection flux, $-\overline{A_h\nabla_H E_{kb}}$ is the barotropic diffusion flux, $\mathbf{U}_hH\rho_0g\eta + \mathbf{U}_h\overline{p'} + \mathbf{U}_h\overline{q}$ are barotropic pressure energy flux and A_h is the horizontal eddy viscosity, which is constant in our model. The term \mathbf{F}_b represents the barotropic input. The depth-integrated conversion rate which represents the conversion rate from the barotropic flow to the baroclinic flow is

$$\overline{C} = \overline{\rho'gW} - \overline{\frac{\partial q}{\partial z}W}, \quad (5.12)$$

and the barotropic dissipation term is

$$\overline{\varepsilon_b} = \rho_0A_h\nabla_H\mathbf{U}_h \cdot \nabla_H\mathbf{U}_h. \quad (5.13)$$

The barotropic residual term $\overline{R_{b1}}$ contains the bottom drag and nonlinear conversion rate term. The depth-integrated baroclinic equation reads

$$\frac{\partial}{\partial t}(\overline{E_k} + \overline{E_p}) + \nabla_H \cdot \overline{\mathbf{F}} = \overline{C} - \overline{\varepsilon} - \overline{R}, \quad (5.14)$$

where the baroclinic kinetic energy is

$$E_k = \frac{1}{2}\rho_0(u'^2 + v'^2 + w^2), \quad (5.15)$$

the available potential energy is

$$E_p = \frac{g^2\rho'^2}{2\rho_0N^2}, \quad (5.16)$$

the cross kinetic energy is

$$E_{hk} = \rho_0(Uu' + Vv'), \quad (5.17)$$

and the depth-integrated baroclinic energy flux is

$$\overline{\mathbf{F}} = \overline{\mathbf{u}'_hp'} + \overline{\mathbf{u}'_hq} + \overline{\mathbf{u}_h(E_k + E_p)} + \overline{\mathbf{u}'_hE_{hk}} - \overline{A_h\nabla_H E_k} - \overline{K_h\nabla_H E_p}, \quad (5.18)$$

where $\overline{\mathbf{u}'_hp'} + \overline{\mathbf{u}'_hq}$ is the baroclinic pressure energy flux, $\overline{\mathbf{u}_h(E_k + E_p)} + \overline{\mathbf{u}'_hE_{hk}}$

is the baroclinic advection flux, and $-\overline{A_h\nabla_H E_k} - \overline{K_h\nabla_H E_p}$ is the baroclinic

diffusion flux. The baroclinic dissipation term is

$$\bar{\varepsilon} = \rho_0 A_h \nabla_H \mathbf{u}'_h \cdot \nabla_H \mathbf{u}'_h + \rho_0 A_v \frac{\partial \mathbf{u}'_h}{\partial z} \cdot \frac{\partial \mathbf{u}'_h}{\partial z} + \rho_0 A_h \nabla_H W \cdot \nabla_H W + \rho_0 A_v \frac{\partial w}{\partial z} \cdot \frac{\partial w}{\partial z}. \quad (5.19)$$

where A_v are the vertical eddy viscosity which is estimated with the KPP scheme and K_h are the vertical eddy diffusivity. The baroclinic residual term \bar{R} contains the dissipation of E_p , the bottom drag term and nonlinear conversion rate term.

5.4.1.2 The results

The depth-integrated, time-averaged conversion rate, the divergence of the depth-integrated baroclinic M2 energy flux and the difference between them (the divergence of the energy flux minus the conversion rate) are shown in Fig. 5.5. The results are averaged over 3 tidal cycles from the beginning of the sixteenth M2 tidal cycle. The strong conversion rate distributes mainly along the two meridional ridges, which is similar to the past research (Niwa and Hibiya, 2004; Kerry et al., 2014; Buijsman et al., 2014). The strong baroclinic energy flux divergence has a pattern similar to the conversion rate and the strong difference can be found at locations with strong conversion rate. The conversion rate is larger than the divergence of the baroclinic energy flux in most areas. From the right figure in Fig. 5.5, we can see that the local dissipation mainly occurs at their generation sites.

The domain-integrated, the time-averaged and the depth-integrated budgets are analyzed in this section. We integrate the depth-integrated budgets over 119.5 °E - 122.5 °E and 18 °N - 22.5 °N and average them over 3 tidal cycles from the beginning of the sixteenth M2 tidal cycle. We keep the tendency terms in our paper, which is not the same with Kang and Fringer (2012), because the kinetic and potential energy is not fully stable and they may increase within the three tidal cycles. Then the barotropic energy budget reads

$$\text{BT Tendency} + \nabla \cdot \text{Flux (BT input)} = -\text{Conversion} - \text{BT Dissipation}, \quad (5.20)$$

the baroclinic energy budget reads

$$\text{BC Tendency} + \nabla \cdot \text{Flux (BC radiation)} = \text{Conversion} - \text{BC Dissipation}. \quad (5.21)$$

Here we ignore the diffusion flux in the energy flux terms (5.11 and 5.18) for it is very small (Kang and Fringer, 2012) compared with the other flux terms. We also calculate the energy flux contributions and find that the hydrostatic term is really the dominant term. The dissipation here is not calculated from the dissipation terms in the equations, but represents the remaining terms in the two equations (5.20 and 5.21)

(Niwa and Hibiya, 2004; Kang and Fringer, 2012) and may contain some errors due to offline calculations.

The results of the budgets can be found in Table 5.1 and Table 5.2. Results show that about 15.1 GW is transferred from the M2 barotropic tide to M2 baroclinic tide, which is about 88% of the barotropic input (17.1 GW). The barotropic dissipation is about 2.0 GW (about 11.4 % of the barotropic input). The net baroclinic energy flux away from Luzon ridge is about 4.5 GW (29.6% of the conversion rate and 26.1% of the barotropic tide input) and the baroclinic dissipation is about 9.4 GW. To sum up, there are 17.1 GW converted from M2 barotropic tide in our model: 4.5 GW energy radiates away from the Luzon ridge, the total dissipation is 11.3 GW and the remaining 1.3 GW is the tendency. The barotropic and baroclinic advection flux are very small in all experiments compared with other terms. The barotropic tendency is in the order of about 10^{-2} GW and the baroclinic tendency is a little larger than the barotropic tendency. The barotropic dissipation is between 0.9 and 2.0 GW, and the baroclinic dissipation is between 9.0 and 14.0 GW.

The results of the former research (Niwa and Hibiya, 2004; Jan et al., 2008; Kerry et al., 2014; Zhao, 2014) showed that the conversion rate of M2 tide calculated at the Luzon ridge was between 10 and 20 GW, and the energy flux of M2 tide was between 2 and 10 GW. We must notice that the calculation domains used by them and us are not exactly the same.

In order to know the influence of the stratification and the model grid spacing on the results of the energy budgets, several experiments introduced in section 5.2 are carried out. The results of the energy budgets in each experiment are also shown in Table 5.1 and Table 5.2. Exp_Winter and Exp_Summer are used to examine the sensitivity of energy budgets to the stratification. We can see that the barotropic input, the conversion rate and the baroclinic energy flux in Exp_Winter are the largest compared with the values in Exp_Summer and Exp_Ref; in contrast, these values from Exp_Summer are the smallest. The barotropic input and the conversion rate in Exp_Winter are about 2.0 GW larger than these in Exp_Summer and the energy flux in Exp_winter is about 0.8 GW larger than that in Exp_Summer. Thus we may infer that the stratification makes a contribution to the seasonal variations of the conversion of the M2 tide.

The conversion rate and the energy flux of tides in global ocean are sensitive to the model resolution (Niwa and Hibiya, 2011; 2014). Exp_Reso1 and Exp_Reso2 are

used to examine the sensitivity of energy budgets to the resolution. When the horizontal resolution is $1/30^0 \times 1/30^0$ (Exp_Reso1) and the horizontal resolution is $1/20^0 \times 1/20^0$ (Exp_Reso2), the barotropic input and the baroclinic energy flux in the two experiments are all a little smaller than the results in Exp_Ref. The above results in Exp_Reso2 are smaller than the results in Exp_Reso1. This is consistent with the past research that the generated internal tide energy flux will be smaller by using a coarser resolution (Niwa and Hibiya, 2004).

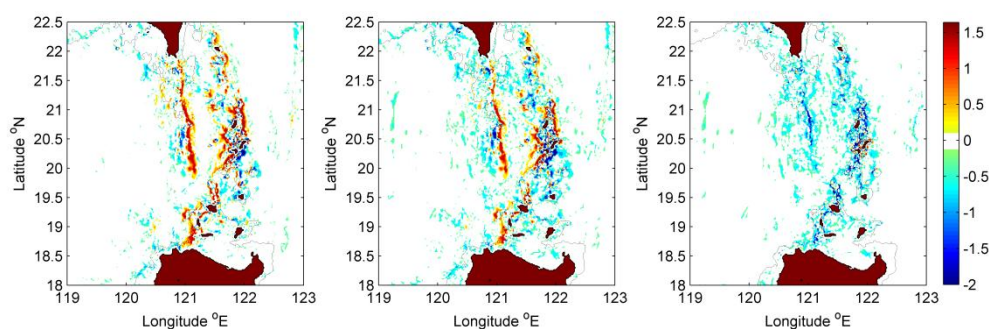


Figure 5.5. From the left to the right: the depth-integrated, time-averaged conversion rate; the divergence of the depth-integrated, time-averaged baroclinic M2 energy flux and the difference between them (the divergence of the energy flux minus the conversion rate). Bathymetry contour is -1000 m. (W m^{-2})

Table 5.1. The barotropic energy budget. (GW)

Cases	$\partial Pe/\partial t$	$\partial Ke/\partial t$	Conversion n	Energy flux	Advection n flux	Dissipation n
Ref	0.004	0.083	15.062	-17.103	0.001	1.953
Winter	0.004	0.072	15.945	-17.956	0.001	1.934
Summer	0.004	0.068	14.171	-15.991	0.001	1.747
Reso1	-0.012	-0.120	14.367	-16.259	0.004	2.020
Reso2	-0.014	-0.155	15.535	-16.275	-0.004	0.913

Table 5.2. The baroclinic energy budget. (GW)

Cases	$\partial Pe/\partial t$	$\partial Ke/\partial t$	Conversion n	Energy flux	Advection n flux	Dissipation n
Ref	0.761	0.447	15.062	4.461	0.015	9.378
Winter	0.970	0.305	15.945	4.799	-0.006	9.877

Summer	0.504	0.150	14.171	4.032	0.039	9.446
Reso1	0.688	0.427	14.367	4.148	0.015	9.089
Reso2	0.675	0.611	15.535	3.877	0.011	10.361

5.4.2 The barotropic and baroclinic kinetic energy equations

5.4.2.1 Theory

The barotropic and baroclinic kinetic energy equations derived from Euler equations are shown in this part. The following equations can be obtained by adding the nonhydrostatic pressure terms to the equations derived by the studies (Zaron and Egbert, 2006; Ponte and Cornuelle, 2013). We can also obtain the kinetic energy budgets after ignoring some nonlinear terms and potential energy terms in the equations from Kang and Fringer (2012). The depth-integrated barotropic kinetic energy equation reads

$$\frac{\partial}{\partial t}(\overline{E_{kb}}) + \nabla_{\mathbf{H}} \cdot \overline{\mathbf{F}_p} = -\overline{\mathcal{C}} - \overline{\varepsilon_b} - \overline{R_{b2}}, \quad (5.22)$$

where the barotropic kinetic energy is

$$E_{kb} = \frac{1}{2} \rho_0 (U^2 + V^2), \quad (5.23)$$

the depth-integrated barotropic energy flux is

$$\overline{\mathbf{F}_p} = \mathbf{U}_h H \rho_0 g \eta + \mathbf{U}_h \overline{p'} + \mathbf{U}_h \overline{q}, \quad (5.24)$$

the depth-integrated conversion rate is

$$\overline{\mathcal{C}} = \overline{\rho' g W} - \frac{\partial \overline{q}}{\partial z}, \quad (5.25)$$

and the barotropic dissipation term is

$$\overline{\varepsilon_b} = \rho_0 A_h \nabla_{\mathbf{H}} \mathbf{U}_h \cdot \nabla_{\mathbf{H}} \mathbf{U}_h. \quad (5.26)$$

The barotropic residual term $\overline{R_{b2}}$ contains the bottom drag. The depth-integrated baroclinic kinetic energy equation reads

$$\frac{\partial}{\partial t}(\overline{E_{k1}}) + \nabla_{\mathbf{H}} \cdot \overline{\mathbf{F}_1} = \overline{\mathcal{C}_1} - \overline{\varepsilon} - \overline{R_1}, \quad (5.27)$$

where the baroclinic kinetic energy is

$$E_{k1} = \frac{1}{2} \rho_0 (u'^2 + v'^2), \quad (5.28)$$

the depth-integrated baroclinic energy flux is

$$\overline{\mathbf{F}}_1 = \overline{\mathbf{u}'_h p'} + \overline{\mathbf{u}'_h q}, \quad (5.29)$$

the depth-integrated baroclinic conversion rate is

$$\overline{C}_1 = \overline{\rho' g w'} - \overline{\frac{\partial q}{\partial z} w'}, \quad (5.30)$$

and the baroclinic dissipation term is

$$\overline{\varepsilon} = \rho_0 A_h \nabla_H \mathbf{u}'_h \cdot \nabla_H \mathbf{u}'_h + \rho_0 A_v \frac{\partial \mathbf{u}'_h}{\partial z} \cdot \frac{\partial \mathbf{u}'_h}{\partial z}. \quad (5.31)$$

where A_h and A_v are the horizontal and vertical eddy viscosity. The baroclinic residual term \overline{R}_1 contains the bottom drag term.

5.4.2.2 The results

The barotropic and the baroclinic energy budgets are analyzed in this section. The barotropic kinetic energy budget reads

$$\text{BT Tendency} + \nabla \cdot \text{Flux (BT input)} = -\text{BT Conversion} - \text{BT Dissipation}, \quad (5.32)$$

the baroclinic kinetic energy budget reads

$$\text{BC Tendency} + \nabla \cdot \text{Flux (BC radiation)} = \text{BC Conversion} - \text{BC Dissipation}. \quad (5.33)$$

These terms (5.32 and 5.33) represent the terms in equations (5.22 and 5.27). The dissipation here is not calculated from the dissipation terms in the equations, but represents the remaining terms in the two equations (5.32 and 5.33) as done in section 5.4.1.2.

The domain-integrated, the time-averaged and the depth-integrated budgets are obtained as follows. The depth-integrated budgets are averaged over 3 tidal cycles from the beginning of the sixteenth M2 tidal cycle and integrated over 119.5 °E - 122.5 °E and 18 °N - 22.5 °N. The values of the barotropic and baroclinic kinetic energy budgets are shown in Table 5.3 and Table 5.4. The formulas for the tendency of the kinetic energy, the conversion rate and the energy flux terms in Table 5.3 and in Table 5.1 are exactly the same, so the values of these terms in the two tables are the same. The barotropic dissipations in Table 5.3 are similar to the ones in Table 5.1, moreover, the tendency of the potential energy and the barotropic advection flux are all small. To sum up, comparing the results in Table 5.3 with the results in Table 5.1, we can see that the results are quite similar and this means that the potential energy budget plays a very small role in the full barotropic energy budget.

The formulas for the tendency in the baroclinic kinetic energy equation and the tendency in the baroclinic energy equation are not the same: there is no vertical

velocity in former equation, thus the results are not the same. The results of the depth-integrated baroclinic conversion rate $\bar{C}_1 = \overline{\rho' g w'} - \overline{\frac{\partial q}{\partial z} w'}$ are shown in Table 5.4. The values of the baroclinic conversion rate from Exp_Ref, Exp_Winter and Exp_Summer are 15, 15.7 and 14.3 GW, respectively. But when the resolution of the experiments is coarser, the baroclinic conversion rate becomes smaller. In addition, comparing the results in Table 5.4 with the results in Table 5.2, we can see that the biggest difference between the kinetic energy equations and the full energy equations is the baroclinic conversion rate. This term $\bar{C}_1 = \overline{\rho' g w'} - \overline{\frac{\partial q}{\partial z} w'}$ in the baroclinic kinetic energy equation represents the conversion rate of available potential energy into baroclinic energy and $\bar{C} = \overline{\rho' g W} - \overline{\frac{\partial q}{\partial z} W}$ represents the barotropic energy kinetic energy into available potential energy. They are usually similar and numerically equal when the flow is in viscid and adiabatic (Zaron and Egbert, 2006). The values of the two terms from Exp_Ref, Exp_Winter and Exp_Summer are almost the same. But when the grid spacing is coarser, the difference becomes larger.

Table 5.3. The barotropic kinetic energy budget. (GW)

Cases	$\partial Ke/\partial t$	Conversion	Energy flux	Dissipation
Ref	0.083	15.062	-17.103	1.958
Winter	0.072	15.945	-17.956	1.939
Summer	0.068	14.171	-15.991	1.752
Reso1	-0.120	14.367	-16.259	2.012
Reso2	-0.155	15.535	-16.275	0.895

Table 5.4. The baroclinic kinetic energy budget. (GW)

Cases	$\partial Ke/\partial t$	Conversion	Energy flux	Dissipation
Ref	0.401	15.004	4.461	10.142
Winter	0.325	15.665	4.799	10.541
Summer	0.074	14.297	4.032	10.191
Reso1	0.322	12.866	4.148	8.396
Reso2	0.485	13.024	3.877	8.662

5.5 The energy budgets of K1 internal tide

The Northern portion of the South China Sea is dominated by the diurnal tides, which propagate from the Pacific Ocean to the Northern portion of the South China Sea through the Luzon strait, where the baroclinic tides are generated by the barotropic tides over bottom topography. The amplitude of K1 surface tides may reduce by the conversion energy from the barotropic tide to the baroclinic tide (Jan et al., 2007), and it would be interesting to study the energy budgets of the K1 tide.

The energetics of K1 internal tide at the Luzon ridge has been studied in Jan et al. (2007). In their research, they used the three-dimensional Princeton Ocean Model (POM) with hydrostatic approximation to simulate the K1 tide. The same formulas in Niwa and Hibiya (2004) were used to calculate the barotropic input, the conversion rate and the baroclinic energy flux. Their results showed that the barotropic energy input, the conversion rate, and the net energy flux were 34.2, 12.4 and 3.6 GW at the Luzon ridge, respectively.

Fig. 5.6 shows the depth-integrated, time-averaged conversion rate, the divergence of the depth-integrated baroclinic K1 energy flux and the difference between them (the divergence of the energy flux minus the conversion rate). The patterns are quite different from the results for M2 tide: especially, the conversion rates of K1 tide are negative over $120.8^{\circ}\text{E} - 121.2^{\circ}\text{E}$ and $19.7^{\circ}\text{N} - 20.3^{\circ}\text{N}$, but they are positive for M2 tide at the same locations. The strong conversion rate of K1 tide distributes at the two sides of the east ridge and the northern portion of the west ridge, which is consistent with the research (Jan et al., 2008). The energy flux divergence shows a pattern similar to the conversion rate and the dissipation mostly occurs in the middle and southern parts of the east ridge.

The full barotropic and baroclinic energy budgets and the barotropic and baroclinic kinetic energy budgets for K1 internal tide are also calculated and shown in Table 5.5 and Table 5.6. The area integrating, the time-averaged and the depth-integrated budgets are calculated as follows: we integrate the depth-integrated budgets over $119.5^{\circ}\text{E} - 122.5^{\circ}\text{E}$ and $18^{\circ}\text{N} - 22.5^{\circ}\text{N}$ and average those over 2 tidal cycles after 14.6 K1 tidal cycles. We can see in Table 5.5 that the barotropic input, the conversion rate and the energy flux are about 23.6, 18.8 (80% of the barotropic input) and 6.5 GW (27.5% of the barotropic input), respectively. The total dissipation of the domain is about 15.8 GW: the barotropic dissipation is 4.6 GW and the

baroclinic dissipation is 11.2 GW. The barotropic input is smaller than the results (Jan et al., 2007), but the conversion rate and the energy flux are larger than the results (Jan et al., 2007). The main reason for these is that the domains used by the two papers are not exactly the same, and the model and formula for the calculations are not same. All the barotropic input, the conversion rate and the baroclinic energy flux for K1 tide are larger than the ones for M2 tide. Table 5.6 shows the barotropic and baroclinic kinetic energy budgets. The baroclinic conversion rate is little smaller than the barotropic conversion rate.

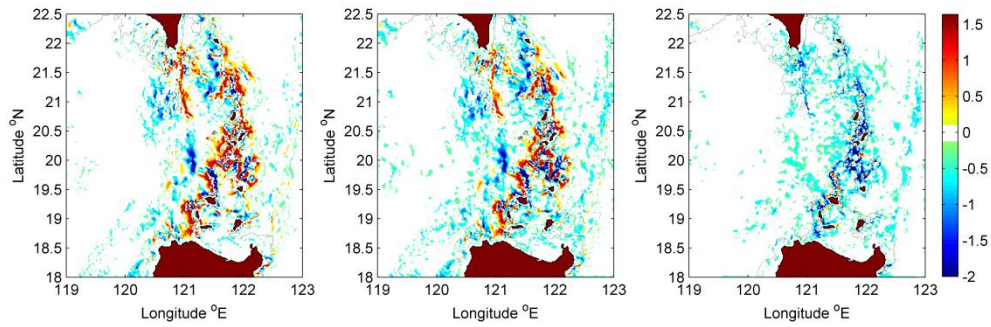


Figure 5.6. From the left to the right: the depth-integrated, time-averaged conversion rate; the divergence of the depth-integrated, time-averaged K1 baroclinic energy flux and the difference between them (the divergence of the energy flux minus the conversion rate). Bathymetry contour is -1000 m. (W m^{-2})

Table 5.5. The barotropic and baroclinic energy budgets (K1). (GW)

Cases	$\partial Pe/\partial t$	$\partial Ke/\partial t$	Conversion n	Energy flux	Advection flux	Dissipation n
Barotropic	-0.006	0.206	18.842	-23.613	0.003	4.568
Baroclinic	0.785	0.370	18.842	6.466	-0.015	11.236

Table 5.6. The barotropic and baroclinic kinetic energy budgets (K1). (GW)

Cases	$\partial Ke/\partial t$	Conversion	Energy flux	Dissipation
Barotropic	0.206	18.842	-23.613	4.565
Baroclinic	0.197	16.873	6.466	10.210

5.6 The conversion rate (Nycander, 2005)

Nycander (2005) derived a formula for the conversion rate based on the linear theory (Bell, 1975a, b; Llewellyn Smith and Young, 2002). The domain integrated conversion rate reads,

$$C = \iint C_+ dx dy + \iint C_- dx dy, \quad (5.34)$$

where

$$C_+ = -\frac{\rho_0 N_b U_+^2}{4\pi} \sqrt{1 - \frac{f^2}{\omega^2} \frac{\partial h}{\partial x}} \iint \frac{\partial g_a(|\mathbf{x}-\mathbf{x}'|)}{\partial x'} h(\mathbf{x}') dx' dy', \quad (5.35)$$

and

$$C_- = -\frac{\rho_0 N_b U_-^2}{4\pi} \sqrt{1 - \frac{f^2}{\omega^2} \frac{\partial h}{\partial y}} \iint \frac{\partial g_a(|\mathbf{x}-\mathbf{x}'|)}{\partial y'} h(\mathbf{x}') dx' dy'. \quad (5.36)$$

The formula is in the tidal-ellipse coordinate, where ρ_0 is the reference density, N_b is the bottom stratification, U_+ and U_- are the amplitudes of the semimajor and semiminor axis of the barotropic M2 tidal velocity. f is the Coriolis force, ω is the M2 tidal frequency and h is the bottom topography. Here g_a is a highpass filter,

$$g_a(r) = \frac{1}{a} G\left(\frac{r}{a}\right), \quad (5.37)$$

where G is a filtered Green function,

$$G(x) = \frac{1}{x} - \frac{\sqrt{\pi}}{2} e^{-\frac{x^2}{8}} I_0\left(\frac{x^2}{8}\right), \quad (5.38)$$

and the cutoff length a is defined by

$$a = \frac{1.455}{\pi \sqrt{\omega^2 - f^2}} \int_{-H}^0 N(z) dz, \quad (5.39)$$

where $N(z)$ is the stratification, H is the depth.

The formula has been used to calculate the global tide conversion rate in much past research (Nycander, 2005; Green and Nycander, 2013; Melet et al., 2013; Falahat et al., 2014). In addition, reformulation of Nycander (2005) can be found in Zilberman et al. (2009). The advantage of the formula (Nycander, 2005) is that the topography is in real space. However, there are some limitations for the formula: firstly, the formula is got from the linear theory and is not very suitable for the supercritical topography (Falahat et al., 2014); secondly, the results are not reliable when the depth is shallower than -500 m (Falahat et al., 2014), because of more supercritical topography caused by strong stratification and large tidal excursion parameter caused by strong tidal currents in areas of shallow water; thirdly, through the formula, one may see that the results are sensitive to the resolution, when the

topography changes rapidly in the longitudinal and latitudinal directions; at last, the conversion rate is proportional to the bottom stratification due to applying the WKB approximation in linear theory. When the bottom stratification is small and the vertical stratification varies strongly, the conversion rate becomes unreliable (Zarroug et al., 2009). We should take the whole depth structure of $N(z)$ into account.

Though the formula includes the influence of the non-uniform vertical stratification through the cutoff length a , we offer another method to take account for the influence of the non-uniform stratification. When the stratification is non-uniform, the average stratification $N_{ave} = \frac{1}{H} \int_{-H}^0 N(z) dz$ can be used to parameterize the conversion rate (Llewellyn Smith and Young, 2003). Considering the non-uniform stratification, we use both N_b and N_{ave} in the following calculations, then we can compare the results using N_b and N_{ave} with model results. We must point out that the formula using N_{ave} isn't got from a strict derivation, but the results of using N_{ave} can be seen as references to the calculations by the formula (Nycander, 2005).

The numerical scheme can be found in detail in Green and Nycander (2013). To do the calculation, firstly, we transform the formulas (5.34-5.36) from the tide-ellipse coordinate to the longitude-latitude coordinate. Secondly, we calculate the topography, stratification N_b and N_{ave} from the model. Thirdly, we calculate the amplitudes and phases of the barotropic velocities from the model results over three tidal cycles beginning from the sixteenth M2 tidal cycle and interpolate them onto the points between the topographic points as done in Falahat et al. (2014). After transforming the formulas and obtaining these data, we can get the domain integrated conversion rate using the equations (5.34-5.36).

The depth-integrated, time-averaged conversion rate (model result) and the conversion rate calculated by the formula (Nycander, 2005) using the depth-averaged stratification N_{ave} are shown in Fig. 5.7. The model result has been discussed in 5.4.1.2. The conversion rate using the formula (Nycander, 2005) has a pattern similar to the conversion rate (model result): there are strong conversion rate distributing along the two meridional ridges where the terrain slope are large. The main differences between the results are that there are less negative values using the formula and the positive values using the formula are not as large as the model results. These are remarkable because of different methods of dealing with the data.

We integrate the depth-integrated conversion rate (model results) over 119.5 °E - 122.5 °E and 18 °N - 22.5 °N and average them over 3 tidal cycles from the beginning of the sixteenth M2 tidal cycle. We only consider the conversion rate when the depth is deeper than -500 m. In order to inhibit very few unreal values using the formulas (5.35 and 5.36), we set the areas with the conversion rate larger than 4 Wm^{-2} to be 4 Wm^{-2} and with the conversion rate smaller than -4 Wm^{-2} to be -4 Wm^{-2} . Actually, if we don't do that, the results also don't change too much and do not affect the conclusions. The area integrating the time-averaged and the depth-integrated conversion rates (model results) and the conversion rates using the formula (Nycander, 2005) are shown in Table 5.7. The model results from Exp_Ref, Exp_Reso1 and Exp_Reso2 are 12.3, 12.8 and 13.4 TW, respectively, and it means that the conversion rates from the three experiments in the top 500 meters are 2.8, 1.6 and 2.1 TW, respectively. We can see in Table 5.7 that the results using N_{ave} and N_{b} from the same experiment are in the same order of magnitude. Moreover, the results with N_{ave} are larger than the ones with N_{b} . The results from Exp_Ref and Exp_Reso1 using the formula (Nycander, 2005) with the bottom stratification N_{b} are smaller than model results from the same experiment, thus the formula (Nycander, 2005) may underestimate the conversion rate at the Luzon ridge for a high resolution. The conversion rate from Exp_Reso2 is larger than the model result mainly because of the complicated topography and coarser resolution. When we replace the bottom stratification N_{b} in the formula to the depth averaged stratification N_{ave} , the result from Exp_Ref compares well with the model result and is the best result.

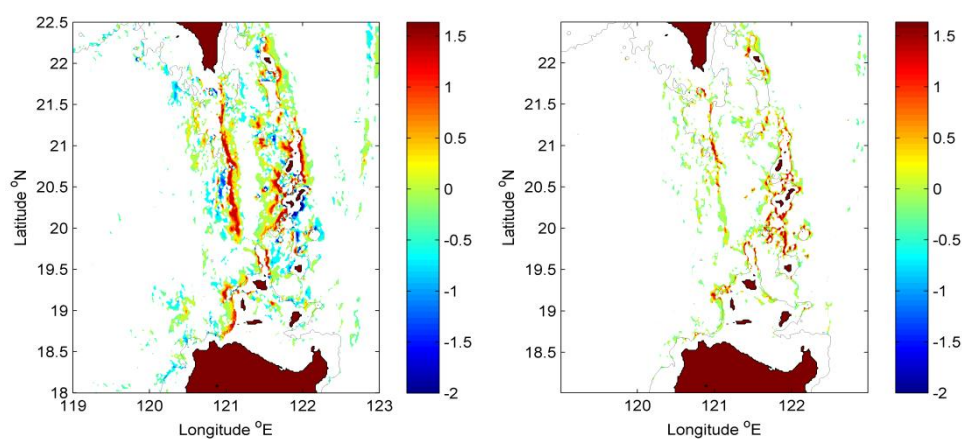


Figure 5.7. The depth-integrated, time-averaged conversion rate ($<-500 \text{ m}$, W m^{-2}), left: model result (Ref); right: using the method of Green and Nycander (2013). Bathymetry contour is -1000 m . The values in blank space are between -0.1 and 0.1

W m^{-2} .

Table 5.7. The conversion rate. (GW)

	Ref	Reso1	Reso2
model	12.3	12.8	13.4
N_b	6.4	4.1	17.1
N_{ave}	12.0	6.9	24.0

5.7 Discussion

Here, the influence of the integration time on the energy budgets is also investigated. The domain-integrated, the time-averaged and the depth-integrated budgets which are integrated over $119.5^\circ\text{E} - 122.5^\circ\text{E}$ and $18^\circ\text{N} - 22.5^\circ\text{N}$ and averaged over 3 tidal cycles from the beginning of the eighth M2 tidal cycle are shown in Table 5.8 and Table 5.9. In contrast, the energy budgets shown in Table 5.1 and Table 5.2 are averaged from the beginning of the sixteenth M2 tidal cycle. The barotropic input, the conversion rate and the barotropic dissipation shown in Table 5.8 are all a little smaller than ones shown in Table 5.1. Furthermore, we can see in Table 5.8 that the barotropic input, the conversion rate and the barotropic dissipation for Exp_Ref are 15.9, 14.1 and 1.6 GW, respectively, which are 1.2, 1.0 and 0.35 GW smaller than ones in Table 5.1.

We can see in Table 5.9 that the conversion rate, the baroclinic energy flux and the baroclinic dissipation for Exp_Ref are 14.1, 4.2 and 8.3 GW, respectively. The conversion rate, the baroclinic flux and the baroclinic dissipation for Exp_Ref, Exp_Winter, Exp_Reso1 and Exp_Reso2 in Table 5.9 are all a little smaller than ones in Table 5.2. However, the conversion rate and the baroclinic energy flux for Exp_Summer in Table 5.9 are a little larger than ones in Table 5.2. In conclusion, the energy budgets change a little with the changing of the integration time.

We have shown the influence of the resolution of the model, the stratification and the integration time on the energy budgets in the paper. As we know, the energy budgets are also influenced more or less by the domain of the model, the boundary conditions, the forcing, the schemes we use, the values of the viscosity and the diffusivity. So, we can adjust some and test more controlling parameters to get better

simulations, if we have enough observation data.

Table 5.8. The barotropic energy budget. (GW)

Cases	$\partial Pe/\partial t$	$\partial Ke/\partial t$	Conversion	Energy	Advection	Dissipation
			n	flux	n flux	n
Ref	-0.015	0.250	14.073	-15.940	0.001	1.631
Winter	-0.015	0.251	15.514	-17.374	0.001	1.623
Summer	-0.010	0.221	15.129	-17.122	0.001	1.781
Reso1	-0.016	0.284	13.562	-14.995	0.002	1.163
Reso2	-0.017	0.295	13.667	-14.650	-0.002	0.707

Table 5.9. The baroclinic energy budget. (GW)

Cases	$\partial Pe/\partial t$	$\partial Ke/\partial t$	Conversion	Energy	Advection	Dissipation
			n	flux	n flux	n
Ref	0.737	0.837	14.073	4.228	0.0001	8.271
Winter	0.522	0.835	15.514	4.814	-0.001	9.344
Summer	1.286	0.582	15.129	4.677	0.019	8.565
Reso1	0.509	0.929	13.562	3.750	0.012	8.362
Reso2	0.450	0.931	13.667	3.392	0.002	8.892

5.8 Conclusion

We use three-dimensional MITgcm to simulate the M2 internal tide and K1 internal tide at the Luzon ridge, where both diurnal and semidiurnal internal tides are generated by barotropic tides over bottom topography. Six experiments are performed to investigate the energetics of internal tides and examine the sensitivity of the results to the resolution and stratification. The experiments are forced at the four boundaries by M2 and K1 barotropic tides through the amplitudes and phases of barotropic tides extracted from TPXO7.2.

From the baroclinic velocity fields, we can see that the internal wave beams are controlled by the linear dispersion relation. The Luzon Strait is also a source of nonlinear internal waves (Ramp et al., 2004; Zhao and Alford, 2006; Li and Farmer, 2011). The strong nonlinear waves are not found in the paper mainly due to the

coarse resolution. Through calculating the tidal ellipses, we can see that the major axis amplitude is large along the double-ridge, especially in the northern portion of the west ridge and the middle and southern portions of the east ridge. The maximum velocity can reach $U_{\max} = 0.38$ m/s.

The input energy of the barotropic tide, the conversion rate and the baroclinic energy flux at the Luzon ridge based on POM has been studied in past research (Niwa and Hibiya, 2004; Jan et al., 2008). The conversion rate was also calculated based on ROMS (Kerry et al., 2014) and the energy flux was calculated using the sea surface height measurements (Zhao, 2014). Their results showed that the conversion rate of M2 tide calculated at the Luzon ridge was between 10 and 20 GW, and the energy flux of M2 tide was about between 2 and 10 GW.

Here two different energy budgets are calculated. Firstly, full energy budgets (Kang and Fringer, 2012) are shown. There are 17.1 GW energy converted from M2 barotropic tide in our model: 4.5 GW (26.1% of the barotropic tide input) energy radiates away from the Luzon ridge, the total dissipation is 11.3 GW and the remaining 1.3 GW is the tendency. The conversion rate is about 15.1 GW and the advection flux is very small. We use the stratification from SODA 2.24 to examine the sensitivity of the results to the stratification and find that the barotropic input, the conversion rate and the baroclinic energy flux in the two experiments using SODA are all similar to the results from Exp_Ref using WOCE. Comparing the results from Exp_Reso1 and Exp_Reso2 with the results from Exp_Ref, we can see that the generated internal tide energy flux will be smaller by using a coarser resolution (Niwa and Hibiya, 2004). Secondly, the kinetic energy budgets are analyzed. Comparing the results from kinetic budgets and full energy budgets, we can see the potential energy budget plays a very small role in the full barotropic energy budget. The baroclinic conversion rate and barotropic conversion rate in the kinetic energy equations are examined. They are usually similar and numerically equal when the flow is in viscous and adiabatic (Zaron and Egbert, 2006). The values of the two terms from Exp_Ref, Exp_Winter and Exp_Summer are almost the same. But when the grid spacing is coarser, the difference becomes larger.

The full barotropic and baroclinic energy budgets and the barotropic and baroclinic kinetic energy budgets for K1 tide are also calculated. There are 23.6 GW energy converted from K1 barotropic tide in our model: 6.5 GW (27.5% of the barotropic tide input) energy radiates away from the Luzon ridge, the total

dissipation is 15.8 GW and the conversion rate is about 18.8 GW (80% of the barotropic input). The baroclinic conversion rate is little smaller than the barotropic conversion rate.

The formula (Nycander, 2005) is also used to calculate the conversion rate here and it may underestimate the conversion rate because of using the bottom stratification N_b in the calculation. When we use the depth-averaged stratification N_{ave} , the result from Exp_Ref is the best result.

The energy budgets of the tides at the Luzon ridge are studied in this paper. But some details can be improved. For example, we can adjust some and test more controlling parameters that has an influence on the final results, if we have enough observation data.

Chapter 6

6 Summary and Outlook

6.1 Summary

In Chapter 2, the velocity data from SODA and ECCO2, mean flow and eddy velocity from the global eddy-permitting STORM model are used to calculate the conversion rate from geostrophic flows into internal lee waves based on linear theory. The WOCE hydrographic atlas is used to give the buoyancy frequency, while single beam sounding data is used to calculate the topographic spectrum and the topographic roughness. In addition, the roughness (Goff and Arbic, 2010) is used.

The energy transferred about 0.03-0.23 TW using single beam sounding data from geostrophic flows to internal lee waves field. The values will be between 0.03 and 0.08 TW using the roughness of Goff and Arbic (2010). The results show that there are lots of areas with zero-value for the roughness of Goff and Arbic (2010) and the roughness (Goff and Arbic, 2010) is larger than the roughness calculated from single beam sounding data in most areas. Therefore, we choose the values calculated using single beam sounding data as the last results. These values are smaller than the result of Scott et al. (2011). In addition, the conversion rates calculated using SODA and ECCO2 are smaller than the rates calculated using the mean flow and eddy velocity from the global eddy-permitting STORM model. The conversion rates are largely influenced by the velocity data and the roughness.

We differentiate between the conversion rate from the eddies and from the mean flow, and the difference between the conversion rate from eddies and mean flow is about 0.05-0.11 TW. Compared with 1 TW of power lost from barotropic tides in the deep ocean (Egbert and Ray, 2001), the energy transferred from geostrophic flows is a little smaller. The lee waves generated by geostrophic flows have a significant impact on the ocean state (Melet et al., 2014). The role of the lee waves generated by geostrophic flows should be further discussed, because the exact conversion rate of lee waves is still a wide open question, and the vertical structure and process of dissipation of lee waves are still not clear.

In Chapter 3, a series of experiments are set up to investigate the baroclinic tide

generated by the barotropic tide over sinusoidal topography. This process has been studied in linear theory; here we focus on the effects of the height of the topography, the amplitude of the barotropic tide, the stratification and the width of topography on the baroclinic tide generated and the comparison of the differences between the values predicted by linear theory and the ones calculated by two definitions of conversion rates.

The results show that when the height of the topography and the amplitude of the barotropic tide increases, the generated baroclinic velocity will be larger; the pattern of baroclinic velocity field doesn't change too much, when the amplitude of the barotropic tide changes; there will be almost no baroclinic velocity generated in experiment with too weak stratification or too wide topography; the baroclinic velocity generated will be stronger in experiments with stronger stratification.

APE, KE, and APE plus KE are shown in this paper. The patterns between in subcritical cases and in supercritical cases are quite different. Through two methods of calculating the modes of the baroclinic velocity, we find that mode 1 wave has the most energy. The amplitude of mode 2 wave from Exp_3sinusoidal is larger than that from Exp_Ref.

Comparing with the results calculated by C1 (energy flux), C2 (conversion rate) and the results predicted by linear theory, we find that the results predicted by linear theory agree well with the results calculated by C1 in most cases, and the results calculated by C2 are larger than the results calculated by C1 in most cases. In summary, the conversion rates predicted by the formula of Balmforth et al. (2002) can compare well with the results from numerical simulations.

In Chapter 4, two-dimensional simulations of internal waves at the Luzon ridge are studied. Two Gaussian ridges are used to represent the topography and realistic buoyancy frequency calculated from WOCE is used to give the stratification. It is found that the generated baroclinic velocity mainly occurs at their fundamental frequency. The domain-integrated, depth-integrated and time-averaged energy budget is calculated and the results show that the conversion rate is about 60 KW m^{-1} and the energy flux is about 57 KW m^{-1} in the standard experiment. The tendency terms, the advection flux, and the dissipation are all very small, compared with the conversion rate and the energy flux, thus the conversion rate is mainly balance by the energy flux.

The former research (Cai et al., 2002; Buijsamn et al., 2010b; Jan et al., 2012)

shows that the height of the west ridge, the distance between the two ridges and the amplitude of the barotropic tide have influences on the generation of the internal waves. Thus, a series of experiments are set up to investigate the role of the above factors. Firstly, the results show that as the height of the west ridge increases, the westward energy flux on the west side of the topography increases. The increased energy flux mainly occurs from -1000 to -500 m around the west side of the west ridge. Secondly, the internal tide enhances due to a suitable distance between two ridges. When the distance between the two ridges is 100 km, the westward energy flux and the conversion rate are the largest. This is also a reason why the westward solitons are larger than eastward solutions. Thirdly, model results show that the energy flux is appropriate to the square of amplitude of the barotropic tide. The amplitude of the barotropic tide is one of the crucial factors to determine whether the internal solitary waves would be generated or not. When the amplitude of barotropic tide is larger, the speed of the generated internal solitary waves will be larger. Thus, the above factors have obvious influences on the generation of the internal waves in different aspects.

In Chapter 5, the three-dimensional MITgcm is used to simulate the M2 internal tide and K1 internal tide at the Luzon ridge, where both diurnal and semidiurnal internal tides are generated by barotropic tides over bottom topography. The experiments are forced at the four boundaries by M2 and K1 barotropic tides through the amplitudes and phases of barotropic tides extracted from TPXO7.2. Six experiments are performed to investigate the energetics of the internal tides and examine the sensitivity of the results to the resolution and stratification.

From the baroclinic velocity fields, we find that the internal wave beams are controlled by the linear dispersion relation. The Luzon Strait is also a source of nonlinear internal waves (Ramp et al., 2004; Zhao and Alford, 2006; Li and Farmer, 2011). The strong nonlinear waves are not found here mainly due to the coarse resolution. Through calculating the tidal ellipses, we can see that the major axis amplitude is large along the double-ridge, especially in the northern portion of the west ridge and the middle and southern portions of the east ridge. The maximum velocity can reach $U_{\max} = 0.38 \text{ m s}^{-1}$.

The input energy of the barotropic tide, the conversion rate and the baroclinic energy flux based on POM has been studied in the paper (Niwa and Hibiya, 2004; Jan et al., 2008). The conversion rate was also calculated based on ROMS (Kerry et

al., 2014) and the energy flux was calculated using the sea surface height measurements (Zhao, 2014). Their results showed that the conversion rate of M2 tide calculated at the Luzon ridge was between 10 and 20 GW, and the energy flux of M2 tide was between 2 and 10 GW. But they didn't calculate the full energy budget.

Here two different energy budgets are calculated. Firstly, full energy budgets (Kang and Fringer, 2012) are shown. There are 17.1 GW energy converted from M2 barotropic tide in our model: 4.46 GW (26.1% of the barotropic tide input) energy radiates away from the Luzon ridge, the total dissipation is 11.34 GW and the remaining 1.3 GW is the tendency. The conversion rate is about 15.1 GW and the advection flux is very small. We use the stratification from SODA 2.24 to examine the sensitivity of the results to the stratification and find that the barotropic input, the conversion rate and the baroclinic energy flux in the two experiments using SODA are all similar to the results from Exp_Ref using WOCE. Comparing the results from Exp_Reso1 and Exp_Reso2 with the results from Exp_Ref, we can see that the generated internal tide energy flux will be smaller by using a coarser resolution, which is consistent with the result (Niwa and Hibiya, 2004). Secondly, the kinetic energy budgets are analyzed. Comparing the results from the kinetic budgets and the full energy budgets, we can see the potential energy budget plays a very small role in the full barotropic energy budget. The baroclinic conversion rate and barotropic conversion rate in the kinetic energy equations are examined. They are usually similar and numerically equal when the flow is in viscous and adiabatic (Zaron and Egbert, 2006). The values of the two terms from Exp_Ref, Exp_Winter and Exp_Summer are almost the same. But when the grid spacing is coarser, the difference becomes larger.

The full barotropic and baroclinic energy budgets and the barotropic and baroclinic kinetic energy budgets for K1 tide are also calculated. Model results show that there are 23.6 GW energy converted from K1 barotropic tide: 6.5 GW (27.5% of the barotropic tide input) energy radiates away from the Luzon ridge, the total dissipation is 15.8 GW and the conversion rate is about 18.8 GW (80% of the barotropic input). The baroclinic conversion rate is little smaller than the barotropic conversion rate.

The formula (Nycander, 2005) is also used to calculate the conversion rate here and it may underestimate the conversion rate because of using the bottom stratification N_b in the calculation. When the depth-averaged stratification N_{ave} is

used, the result from Exp_Ref is the best result.

The energy budgets of the tides at the Luzon ridge are studied in this paper. But some details can be improved. For example, we can adjust some and test more controlling parameters that have influences on the final results, if we have enough observation data.

6.2 Outlook

The mixing caused by internal waves plays an important role in sustaining the large scale ocean circulation. The scale of the process is too small for ocean circulation models to resolve; hence we need to parameterize it. So, it's necessary to study the generation, propagation and dissipation of internal waves in ocean. Here, we mainly focus on the lee wave generation and energetics of internal tides. There are some limitations in the thesis that can be improved and some extensions that can be studied in the future.

In Chapter 2, we calculate the conversion rate based on linear theory and use single beam sounding depth data to calculate the topographic spectrum. However, the linear theory is only accurate when the inverse Froude number is less than 1, and there are many areas with zero value for the topographic roughness because of the limitation of the topographic data. The seasonal and annual variability of the conversion rate can also be studied.

The results from Chapter 3 and Chapter 4 are got from the numerical simulations using MITgcm. Other ocean models can be used to do the same simulations. Then we can compare with the results from different models.

In Chapter 5, the three-dimensional MITgcm is used to simulate the internal tides at the Luzon ridge, and the energy budgets of the K1 and M2 internal tides are studied. But some details can be improved. For example, we can adjust some and test more controlling parameters, if we have enough observation data.

The topography is important both for internal lee wave generation and for internal tide generation. Better topographic data is needed both for internal lee wave study and for internal tide study. We will study the process and the vertical structure of the dissipation. This is important if we want to parameterize them in ocean circulation models.

Acknowledgements

First and foremost, I am sincerely grateful to my supervisor Carsten Eden for his excellent guidance and great support. I benefited a lot from his expertise, good ideas and great patience. I would not finish my PHD study without his support.

I feel so happy to work with colleagues Nils Brüggemann, Manita Chouksey, Lars Czeschel, Julia Dräger-Dietel, Alexa Griesel, Philipp Jurgenowski, Martina Nemes, Friederike Pollmann. They are all very kind and helpful. They spent lots of time asking many questions and giving valuable suggestions, especially when I had problems with my presentation. Thanks very much!

I would like to thank Felix Ament, Inga Hense, Lars Kaleschke, Thomas Pohlmann and Jin-Song von Storch for being my committee members. I have met lots of nice people in University of Hamburg. Thanks to all of you.

Many thanks go to my friends, my parents, my aunts, my grandmother and grandfather in China, who have always supported me.

Finally, my PHD study is funded by China Scholarship Council (CSC). I would like to thank CSC for providing the fund for the completion of the thesis.

Bibliography

Alford, M. H., 2001: Internal swell generation: The spatial distribution of energy flux from the wind to mixed layer near-inertial motions. *Journal of Physical Oceanography*, 31(8), 2359-2368.

Alford, M. H., 2003: Improved global maps and 54-year history of wind-work on ocean inertial motions. *Geophysical Research Letters*, 30(8).

Alford, M. H., Lien, R. C., Simmons, H., Klymak, J., Ramp, S., Yang, Y. J., ... and Chang, M. H., 2010: Speed and evolution of nonlinear internal waves transiting the South China Sea. *Journal of Physical Oceanography*, 40(6), 1338-1355.

Alford, M. H., MacKinnon, J. A., Nash, J. D., Simmons, H., Pickering, A., Klymak, J. M., ... and Lu, C. W., 2011: Energy flux and dissipation in Luzon Strait: Two tales of two ridges. *Journal of Physical Oceanography*, 41(11), 2211-2222.

Alford, M. H., Peacock, T., MacKinnon, J. A., Nash, J. D., Buijsman, M. C., Centuroni, L. R., ... and Fu, K. H., 2015: The formation and fate of internal waves in the South China Sea. *Nature*, 521(7550), 65.

Balmforth, N. J., Ierley, G. R., and Young, W. R., 2002: Tidal conversion by subcritical topography. *Journal of Physical Oceanography*, 32(10), 2900-2914.

Balmforth, N. J., and Peacock, T., 2009: Tidal conversion by supercritical topography. *Journal of Physical Oceanography*, 39(8), 1965-1974.

Bell, T. H., 1975a: Lee waves in stratified flows with simple harmonic time dependence. *Journal of Fluid Mechanics*, 67(04), 705-722.

Bell, T. H., 1975b: Topographically generated internal waves in the open ocean. *Journal of Geophysical Research*, 80(3), 320-327.

Brearley, J. A., Sheen, K. L., Naveira Garabato, A. C., Smeed, D. A., and Waterman, S., 2013: Eddy-induced modulation of turbulent dissipation over rough topography in the Southern Ocean. *Journal of Physical Oceanography*, 43(11), 2288-2308.

Buijsman, M. C., Kanarska, Y., and McWilliams, J. C., 2010a: On the generation and evolution of nonlinear internal waves in the South China Sea. *Journal of Geophysical Research: Oceans*, 115(C2).

Buijsman, M. C., Klymak, J. M., Legg, S., Alford, M. H., Farmer, D., MacKinnon, J. A., ... and Simmons, H., 2014: Three-dimensional double-ridge internal tide resonance in Luzon Strait. *Journal of Physical Oceanography*, 44(3), 850-869.

Buijsman, M. C., McWilliams, J. C., and Jackson, C. R., 2010b: East-west asymmetry in nonlinear internal waves from Luzon Strait. *Journal of Geophysical Research: Oceans*, 115(C10).

Buijsman, M. C., Legg, S., and Klymak, J., 2012a: Double-ridge internal tide interference and its effect on dissipation in Luzon Strait. *Journal of Physical Oceanography*, 42(8), 1337-1356.

Buijsman, M. C., Uchiyama, Y., McWilliams, J. C., and Hill-Lindsay, C. R., 2012b: Modeling semidiurnal internal tide variability in the Southern California Bight. *Journal of Physical Oceanography*, 42(1), 62-77.

Cai, S., Long, X., and Gan, Z., 2002: A numerical study of the generation and propagation of internal solitary waves in the Luzon Strait. *Oceanologica Acta*, 25(2), 51-60.

Carter, G. S., Merrifield, M. A., Becker, J. M., Katsumata, K., Gregg, M. C., Luther, D. S., ... and Firing, Y. L., 2008: Energetics of M2 barotropic-to-baroclinic tidal conversion at the Hawaiian Islands. *Journal of Physical Oceanography*, 38(10), 2205-2223.

Carton, J. A., Giese, B. S., and Grodsky, S. A., 2005: Sea level rise and the warming of the oceans in the Simple Ocean Data Assimilation (SODA) ocean reanalysis. *Journal of Geophysical Research: Oceans*, 110(C9).

Chang, M. H., Lien, R. C., Tang, T. Y., D'Asaro, E. A., and Yang, Y. J., 2006: Energy flux of nonlinear internal waves in northern South China Sea. *Geophysical Research Letters*, 33(3).

Chao, S. Y., Ko, D. S., Lien, R. C., and Shaw, P. T., 2007: Assessing the west ridge of Luzon Strait as an internal wave mediator. *Journal of Oceanography*, 63(6), 897-911.

Di Lorenzo, E., Young, W. R., and Smith, S. L., 2006: Numerical and analytical estimates of M₂ tidal conversion at steep oceanic ridges. *Journal of Physical Oceanography*, 36(6), 1072-1084.

Duda, T. F., Lynch, J. F., Irish, J. D., Beardsley, R. C., Ramp, S. R., Chiu, C. S., ... and Yang, Y. J., 2004: Internal tide and nonlinear internal wave behavior at the continental slope in the northern South China Sea. *Oceanic Engineering, IEEE Journal of*, 29(4), 1105-1130.

Eden, C., and Olbers, D., 2014: An energy compartment model for propagation, nonlinear interaction, and dissipation of internal gravity waves. *Journal of Physical Oceanography*, 44(8), 2093-2106.

Egbert, G. D., Bennett, A. F., and Foreman, M. G., 1994: TOPEX/POSEIDON tides estimated using a global inverse model. *Journal of Geophysical Research: Oceans*, 99(C12), 24821-24852.

Egbert, G. D., and Ray, R. D., 2001: Estimates of M₂ tidal energy dissipation from TOPEX/Poseidon altimeter data. *Journal of Geophysical Research: Oceans*, 106(C10), 22475-22502.

Falahat, S., Nycander, J., Roquet, F., and Zarroug, M., 2014: Global calculation of tidal energy conversion into vertical normal modes. *Journal of Physical Oceanography*, 44(12), 3225-3244.

Farmer, D., Li, Q., and Park, J. H., 2009: Internal wave observations in the South China Sea: The role of rotation and non - linearity. *Atmosphere-Ocean*, 47(4), 267-280.

Furuichi, N., Hibiya, T., and Niwa, Y., 2008: Model-predicted distribution of wind-induced internal wave energy in the world's oceans. *Journal of Geophysical Research: Oceans*, 113(C9).

Garabato, A. C. N., Polzin, K. L., King, B. A., Heywood, K. J., and Visbeck, M., 2004: Widespread intense turbulent mixing in the Southern Ocean. *Science*, 303(5655), 210-213.

Gerkema, T., and Zimmerman, J. T. F., 2008: An introduction to internal waves. *Lecture Notes*, Royal NIOZ, Texel.

Gill A E., 1982: *Atmosphere-ocean dynamics*[M]. Academic press.

Goff, J. A., and Arbic, B. K., 2010: Global prediction of abyssal hill roughness statistics for use in ocean models from digital maps of paleo-spreading rate, paleo-ridge orientation, and sediment thickness. *Ocean Modelling*, 32(1), 36-43.

Goff, J. A., and Jordan, T. H., 1988: Stochastic modeling of seafloor morphology: Inversion of Sea Beam data for second-order statistics. *Journal of Geophysical Research: Solid Earth (1978–2012)*, 93(B11), 13589-13608.

Gouretski, V., and Koltermann, K. P., 2004: WOCE global hydrographic climatology. *Berichte des BSH*, 35, 1-52.

Green, J. M., and Nycander, J., 2013: A comparison of tidal conversion parameterizations for tidal models. *Journal of Physical Oceanography*, 43(1), 104-119.

Green, J. M., Simpson, J. H., Legg, S., and Palmer, M. R., 2008: Internal waves, baroclinic energy fluxes and mixing at the European shelf edge. *Continental Shelf Research*, 28(7), 937-950.

Jachec, S. M., Fringer, O. B., Gerritsen, M. G., and Street, R. L., 2006: Numerical simulation of internal tides and the resulting energetics within Monterey Bay and the surrounding area. *Geophysical Research Letters*, 33(12).

Jalali, M., Rapaka, N. R., and Sarkar, S., 2014: Tidal flow over topography: effect of excursion number on wave energetics and turbulence. *Journal of Fluid Mechanics*, 750, 259-283.

Jan, S., Chern, C. S., Wang, J., and Chao, S. Y., 2007: Generation of diurnal K1 internal tide in the Luzon Strait and its influence on surface tide in the South China Sea. *Journal of Geophysical Research: Oceans*, 112(C6).

Jan, S., Chern, C. S., Wang, J., and Chiou, M. D., 2012: Generation and propagation of baroclinic tides modified by the Kuroshio in the Luzon Strait. *Journal of Geophysical Research: Oceans*, 117(C2).

Jan, S., Lien, R. C., and Ting, C. H., 2008: Numerical study of baroclinic tides in Luzon Strait. *Journal of oceanography*, 64(5), 789-802.

Jiang, J., Lu, Y., and Perrie, W., 2005: Estimating the energy flux from the wind to ocean inertial motions: The sensitivity to surface wind fields. *Geophysical research letters*, 32(15).

Kalnay, E., and Coauthors, 1996: The NCEP/NCAR 40-Year Reanalysis Project. *Bull. Amer. Meteor. Soc.*, 77, 437-471.

Kang, D., and Fringer, O., 2010: On the calculation of available potential energy in internal wave fields. *Journal of Physical Oceanography*, 40(11), 2539-2545.

Kang, D., and Fringer, O., 2012: Energetics of barotropic and baroclinic tides in the Monterey Bay area. *Journal of Physical Oceanography*, 42(2), 272-290.

Kelly, S. M., Nash, J. D., and Kunze, E., 2010: Internal-tide energy over topography. *Journal of Geophysical Research: Oceans*, 115(C6).

Kerry, C. G., Powell, B. S., and Carter, G. S., 2014: The impact of subtidal circulation on internal tide generation and propagation in the Philippine Sea. *Journal of Physical Oceanography*, 44(5), 1386-1405.

Khatiwala, S., 2003: Generation of internal tides in an ocean of finite depth: analytical and numerical calculations. *Deep Sea Research Part I: Oceanographic Research Papers*, 50(1), 3-21.

Kuhlbrodt, T., Griesel, A., Montoya, M., Levermann, A., Hofmann, M. and Rahmstorf, S., 2007: On the driving processes of the Atlantic meridional overturning circulation. *Reviews of Geophysics*, 45(2).

Kunze, E., Firing, E., Hummon, J. M., Chereskin, T. K., and Thurnherr, A. M., 2006: Global abyssal mixing inferred from lowered ADCP shear and CTD strain profiles. *Journal of Physical Oceanography*, 36(8), 1553-1576.

Lamb, K. G., 2004: Nonlinear interaction among internal wave beams generated by tidal flow over supercritical topography. *Geophysical Research Letters*, 31(9).

Lamb, K. G., and Kim, J., 2012: Conversion of barotropic tidal energy to internal wave energy over a shelf slope for a linear stratification. *Continental Shelf Research*, 33, 69-88.

Lamb, K. G., and Warn-Varnas, A., 2014: Shoaling of internal solitary waves at the ASIAEX site in the South China Sea. *Nonlinear Processes in Geophysics Discussions*, 1, 1163-1222.

Large, W. G., McWilliams, J. C., and Doney, S. C., 1994: Oceanic vertical mixing: A review and a model with a nonlocal boundary layer parameterization. *Reviews of Geophysics*, 32(4), 363-404.

Legg, S., and Huijts, K.M.H., 2006: Preliminary simulations of internal waves and mixing generated by finite amplitude tidal flow over isolated topography. *Deep Sea Research Part II: Topical Studies in Oceanography*, 53 (1-2). pp. 140-156. ISSN 0967-0645.

Lien, R. C., Tang, T. Y., Chang, M. H., and d'Asaro, E. A., 2005: Energy of nonlinear internal waves in the South China Sea. *Geophysical Research Letters*, 32(5).

Li, Q., and Farmer, D. M., 2011: The generation and evolution of nonlinear internal waves in the deep basin of the South China Sea. *Journal of Physical Oceanography*, 41(7), 1345-1363.

Liu, A. K., Ramp, S. R., Zhao, Y., and Tang, T. Y., 2004: A case study of internal solitary wave propagation during ASIAEX 2001. *Oceanic Engineering, IEEE Journal of*, 29(4), 1144-1156.

Li, X., Zhao, Z., and Pichel, W. G., 2008: Internal solitary waves in the northwestern South China Sea inferred from satellite images. *Geophysical Research Letters*, 35(13).

Llewellyn Smith, S. G., and Young, W. R., 2002: Conversion of the barotropic tide. *Journal of Physical Oceanography*, 32(5), 1554-1566.

Llewellyn Smith, S. G., and Young, W. R., 2003: Tidal conversion at a very steep ridge. *Journal of Fluid Mechanics*, 495, 175-191.

Marshall, J., Adcroft, A., Hill, C., Perelman, L., and Heisey, C., 1997: A finite-volume, incompressible Navier Stokes model for studies of the ocean on parallel computers. *Journal of Geophysical Research: Oceans*, 102(C3), 5753-5766.

Melet, A., Hallberg, R., Legg, S., and Nikurashin, M., 2014: Sensitivity of the ocean state to lee wave-driven mixing. *Journal of Physical Oceanography*, 44(3), 900-921.

Melet, A., Nikurashin, M., Muller, C., Falahat, S., Nycander, J., Timko, P. G., ... and Goff, J. A., 2013: Internal tide generation by abyssal hills using analytical theory. *Journal of Geophysical Research: Oceans*, 118(11), 6303-6318.

Menemenlis, D., Campin, J. M., Heimbach, P., Hill, C., Lee, T., Nguyen, A., ... and Zhang, H., 2008: ECCO2: High resolution global ocean and sea ice data synthesis. *Mercator Ocean Quarterly Newsletter*, 31, 13-21.

Merrifield, M. A., and Holloway, P. E., 2002: Model estimates of M2 internal tide energetics at the Hawaiian Ridge. *Journal of Geophysical Research: Oceans*, 107(C8), 5-1.

Munk, W., and Wunsch, C., 1998: Abyssal recipes II: energetics of tidal and wind mixing. *Deep Sea Research Part I: Oceanographic Research Papers*, 45(12), 1977-2010.

Nikurashin, M., and Ferrari, R., 2010a: Radiation and dissipation of internal waves generated by geostrophic flows impinging on small-scale topography: Theory. *Journal of Physical Oceanography*, 40, 1055-1074.

Nikurashin, M., and Ferrari, R., 2010b: Radiation and dissipation of internal waves generated by geostrophic motions impinging on small-scale topography: Application to the Southern Ocean. *Journal of Physical Oceanography*, 40(9), 2025-2042.

Nikurashin, M., and Ferrari, R., 2011: Global energy conversion rate from geostrophic flows into internal lee waves in the deep ocean. *Geophysical Research Letters*, 38(8).

Nikurashin, M., Ferrari, R., Grisouard, N., and Polzin, K., 2014: The impact of finite-amplitude bottom topography on internal wave generation in the Southern Ocean. *Journal of Physical Oceanography*, 44(11), 2938-2950.

Niwa, Y., and Hibiya, T., 2004: Three-dimensional numerical simulation of M2 internal tides in the East China Sea. *Journal of Geophysical Research: Oceans*, 109(C4).

Niwa, Y., and Hibiya, T., 2011: Estimation of baroclinic tide energy available for deep ocean mixing based on three-dimensional global numerical simulations. *Journal of oceanography*, 67(4), 493-502.

Niwa, Y., and Hibiya, T., 2014: Generation of baroclinic tide energy in a global three-dimensional numerical model with different spatial grid resolutions. *Ocean Modelling*, 80, 59-73.

Nycander, J., 2005: Generation of internal waves in the deep ocean by tides. *Journal of Geophysical Research: Oceans*, 110(C10).

Paoletti, M. S., Drake, M., and Swinney, H. L., 2014: Internal tide generation in nonuniformly stratified deep oceans. *Journal of Geophysical Research: Oceans*, 119(3), 1943-1956.

Párfis, F., Smith, S. L., and Young, W. R., 2006: Tidal conversion at a submarine ridge. *Journal of Physical Oceanography*, 36(6), 1053-1071.

Ponte, A. L., and Cornuelle, B. D., 2013: Coastal numerical modelling of tides: Sensitivity to domain size and remotely generated internal tide. *Ocean Modelling*, 62, 17-26.

Qian, H., Shaw, P. T., and Ko, D. S., 2010: Generation of internal waves by barotropic tidal flow over a steep ridge. *Deep Sea Research Part I: Oceanographic Research Papers*, 57(12), 1521-1531.

Rapaka, N. R., Gayen, B., and Sarkar, S., 2013: Tidal conversion and turbulence at a model ridge: direct and large eddy simulations. *Journal of Fluid Mechanics*, 715, 181-209.

Ramp, S. R., Tang, T. Y., Duda, T. F., Lynch, J. F., Liu, A. K., Chiu, C. S., ... and Yang, Y. J., 2004: Internal solitons in the northeastern South China Sea. Part I: Sources and deep water propagation. *Oceanic Engineering, IEEE Journal of*, 29(4), 1157-1181.

Rimac, A., Storch, J. S., Eden, C., and Haak, H., 2013: The influence of high-resolution wind stress field on the power input to near-inertial motions in the ocean. *Geophysical Research Letters*, 40(18), 4882-4886.

Scott, R. B., Goff, J. A., Naveira Garabato, A. C., and Nurser, A. J. G., 2011: Global rate and spectral characteristics of internal gravity wave generation by geostrophic flow over topography. *Journal of Geophysical Research: Oceans*, 116(C9).

Sen, A., Scott, R.B. and Arbic, B.K., 2008: Global energy dissipation rate of deep-ocean low-frequency flows by quadratic bottom boundary layer drag: Computations from current-meter data. *Geophysical Research Letters*, 35(9).

Shaw, P. T., Ko, D. S., and Chao, S. Y., 2009: Internal solitary waves induced by flow over a ridge: With applications to the northern South China Sea. *Journal of Geophysical Research: Oceans*, 114(C2).

Smith, W. H., and Sandwell, D. T., 1997: Global sea floor topography from satellite altimetry and ship depth soundings. *Science*, 277(5334), 1956-1962.

St. Laurent, L., and Garrett, C., 2002: The role of internal tides in mixing the deep ocean. *Journal of Physical Oceanography*, 32(10), 2882-2899.

Storch, J. S. V., Eden, C., Fast, I., Haak, H., Hernández-Deckers, D., Maier-Reimer, E., ... and Stammer, D., 2012: An estimate of the Lorenz energy cycle for the world ocean based on the STORM/NCEP simulation. *Journal of Physical Oceanography*, 42(12), 2185-2205.

Tanaka, T., Yasuda, I., Tanaka, Y., and Carter, G. S., 2013: Numerical study on tidal mixing along the shelf break in the Green Belt in the southeastern Bering Sea. *Journal of Geophysical Research: Oceans*, 118(12), 6525-6542.

Vallis, G. K., 2016: Geophysical fluid dynamics: whence, whither and why?. In *Proc. R. Soc. A* (Vol. 472, No. 2192, p. 20160140). The Royal Society.

Warn-Varnas, A., Hawkins, J., Lamb, K. G., Piacsek, S., Chin-Bing, S., King, D., and Burgos, G., 2010: Solitary wave generation dynamics at Luzon Strait. *Ocean Modelling*, 31(1), 9-27.

Watanabe, M., and Hibiya, T., 2002: Global estimates of the wind-induced energy flux to inertial motions in the surface mixed layer. *Geophysical research letters*, 29(8).

Waterman, S., Naveira Garabato, A. C., and Polzin, K. L., 2013: Internal waves and turbulence in the Antarctic Circumpolar Current. *Journal of Physical Oceanography*, 43(2), 259-282.

Wright, C. J., Scott, R. B., Ailliot, P., and Furnival, D., 2014: Lee wave generation rates in the deep ocean. *Geophysical Research Letters*, 41(7), 2434-2440.

Wu, L., Miao, C., and Zhao, W., 2013: Patterns of K1 and M2 internal tides and their seasonal variations in the northern South China Sea. *Journal of oceanography*, 69(4), 481-494.

Wunsch, C., 1998: The work done by the wind on the oceanic general circulation. *Journal of Physical Oceanography*, 28(11), 2332-2340.

Xu, J., Chen, Z., Xie, J., and Cai, S., 2016: On generation and evolution of seaward propagating internal solitary waves in the northwestern South China Sea. *Communications in Nonlinear Science and Numerical Simulation*, 32, 122-136.

Xu, Z., Liu, K., Yin, B., Zhao, Z., Wang, Y., and Li, Q., 2016: Long-range propagation and associated variability of internal tides in the South China Sea. *Journal of Geophysical Research: Oceans*, 121, 8268-8286.

Zaron, E. D., and Egbert, G. D., 2006: Verification studies for a z-coordinate primitive-equation model: Tidal conversion at a mid-ocean ridge. *Ocean Modelling*, 14(3), 257-278.

Zarroug, M., Nycander, J., and Döös, K., 2010: Energetics of tidally generated internal waves for nonuniform stratification. *Tellus A*, 62(1), 71-79.

Zhai, X., Greatbatch, R. J., Eden, C., and Hibiya, T., 2009: On the loss of wind-induced near-inertial energy to turbulent mixing in the upper ocean. *Journal of Physical Oceanography*, 39(11), 3040-3045.

Zhang, Z., Fringer, O. B., and Ramp, S. R., 2011: Three-dimensional, nonhydrostatic numerical simulation of nonlinear internal wave generation and propagation in the South China Sea. *Journal of Geophysical Research: Oceans*, 116(C5).

Zhao, Z., 2014: Internal tide radiation from the Luzon Strait. *Journal of Geophysical Research: Oceans*, 119(8), 5434-5448.

Zhao, Z., and Alford, M. H., 2006: Source and propagation of internal solitary waves in the northeastern South China Sea. *Journal of Geophysical Research: Oceans*, 111(C11).

Bibliography

Zhao, Z., Klemas, V., Zheng, Q., and Yan, X. H., 2004: Remote sensing evidence for baroclinic tide origin of internal solitary waves in the northeastern South China Sea. *Geophysical Research Letters*, 31(6).

Zilberman, N. V., Becker, J. M., Merrifield, M. A., and Carter, G. S., 2009: Model estimates of M2 internal tide generation over Mid-Atlantic Ridge topography. *Journal of Physical Oceanography*, 39(10), 2635-2651.